Modeling a geologically complex karst aquifer system, Hochifen-Gottesacker, Alps

Zur Erlangung des akademischen Grades eines

Doktors der Naturwissenschaften

von der Fakultät für

Bauingenieur, Geo- und Umweltwissenschaften

des Karlsruher Instituts für Technologie (KIT)

genehmigte

DISSERTATION

von

Dipl.-Geol. Zhao CHEN

aus Xinjiang, VR China

Tag der mündlichen Prüfung:

30.05.2017

Referent: Prof. Dr. Nico Goldscheider

Korreferent: Prof. Dr. Erwin Zehe

Karlsruhe (2017)

Abstract

About one quarter of the global population is completely or partially dependent on drinking water from karst aquifers. They are vulnerable to contamination and difficult to manage due to their unique hydrogeological characteristics. Many regional important karst systems are hydraulically connected over wide areas and require transboundary exploration, protection and management. Furthermore, future climate projections suggest a strong change in temperature and precipitation regimes in many karst regions of the world over the next decades and may also have a lasting negative impact on local karst water resources in terms of both quantity and quality. To better understand dominate hydrological processes at local karst systems, quantify their dynamics and predict aquifer discharge behaviors under potential future climate conditions, hydrological models tailored to karst catchments are needed.

In order to obtain a better global overview of karst aquifers and to create a basis for sustainable international water resources management, the first part of this study dealt with the mapping of karst aquifers at over-regional scale and presents the basic concepts and the detailed mapping procedure, using France as an example to illustrate the step-by-step workflow, which includes generalization, differentiation of continuous and discontinuous carbonate and evaporite rock areas, and the identification of non-exposed karst aquifers. The map also shows selected caves and karst springs, which are collected in an associated global database. The draft karst aquifer map of Europe shows that 21.6 % of the European land surface is characterized by the presence of (continuous or discontinuous) carbonate rocks; about 13.8 % of the land surface is carbonate rock outcrop.

Subsequently, this study moved from global to local working scale and focused on an Alpine karst system (Hochifen-Gottesacker), which is characterized by complex hydrogeology and can be especially vulnerable under changing hydro-meteorological conditions. A numerical model was developed step-by-step to simulate the surface and subsurface heterogeneous hydrological processes within the studied karst catchment. The model contains a hybrid-structure (combining lumped and distributed model) and incorporates the investigated karst aquifer and its adjacent non-karst area. Additionally, spatially-distributed meteorological variables and their driven snow accumulation/melting dynamic are considered in the simulated catchment. The simulation results demonstrate that the model is able to simulate simultaneously the transient and highly variable discharge behavior of four spatially-distributed model outlets at an hourly time step, which represent a permanent spring, an overflow spring, an estavelle and the surface runoff generated from the non-karst area. Furthermore, the dual flow regime and transient hydrodynamic behavior of phreatic and epiphreatic conduits in the karst aquifer are demonstrated in the simulation.

To better understand model complexity and uncertainty, a novel multi-step sensitivity analysis approach was developed and applied to evaluate the model part representing the karst area for model outlets using a multi-objective and time-varying approach. The information about parameter sensitivity derived and combined from these two work stages made it possible to identify the spatiotemporal dynamics of controlling parameters. The results demonstrate that a limited number of spatially-distributed parameters control the varying flow pattern, which is caused mainly by dynamics of high permeability flow in individual karst sub-catchments and flooding mechanisms in major karst drainage conduits. Additionally, the interactions between parameters were quantified. The results demonstrate that the model is nonlinear and the influential parameters are highly correlated in the model space and time domain. The complete sensitivity analysis was performed for prior and posterior parameter ranges. The difference between them was used to assess the influence of parameter constraints on the results of sensitivity analyses. The results show that the spatial patterns of identified parameter sensitivity and interactions are strongly influenced by given parameter bounds.

The last part of this study presents an investigation of present and future water fluxes and storages within the studied karst catchment using the previous developed numerical model. A delta approach combined with random sampling technique was used to assess the potential impacts of climate changes. The model simulation under current condition demonstrates that a large portion of precipitation infiltrates into the karst aquifer as autogenic recharge and contributes to surface runoff in the adjacent non-karst area, which can partly infiltrate into the karst aquifer as allogenic point recharge. Moreover, the result shows that surface snow storage is dominant from November to April, while subsurface water storage in the karst aquifer dominates from May to October. The climate scenario runs demonstrate that the varied climate conditions affect the spatiotemporal distribution of water fluxes and storages significantly: (1) the total catchment discharge decreases under all evaluated future climate conditions. (2) The spatiotemporal discharge pattern is strongly controlled by temperature variations, which can shift the seasonal snowmelt pattern. The snow storage in the cold season (December to April) decreases significantly under all change scenarios. (3) Increased karst aquifer recharge in winter and spring, and decreased recharge in summer and autumn, partly compensate each other. (4) The impacts on the subsurface flow dynamics are regulated by the karst aquifer due to its characteristic dual flow systems and spatially heterogeneous distributed drainage structure.

Kurzfassung

Etwa ein Viertel der Weltbevölkerung ist ganz oder teilweise abhängig von Trinkwasser aus Karstgrundwasserleitern. Aufgrund ihrer einzigartigen hydrogeologischen Eigenschaften sind Karstaquifere besonders verletzbar gegenüber Schadstoffeinträgen und besonders schwierig zu bewirtschaften. Viele regional wichtige Karstsysteme sind über weite Gebiete hydraulisch miteinander verbunden und erfordern grenzüberschreitende Ansätze zur Erkundung, zum Schutz und zur Bewirtschaftung. Zusätzlich deuten künftige Klimavorhersagen auf eine starke Veränderung der Temperatur- und Niederschlagsregime in vielen Karstregionen der Welt in den nächsten Jahrzehnten hin, und können sich negativ auf lokale Karstwasserressourcen auswirken, sowohl in Bezug auf ihre Quantität als auch hinsichtlich ihrer Qualität. Um die dominanten hydrologischen Prozesse lokaler Karstsysteme besser zu verstehen, ihre Dynamik zu quantifizieren und das Schüttungsverhalten der Karstgrundwasserleiter unter künftigen Klimabedingungen vorhersagen zu können, sind hydrologische Modelle, die auf Karsteinzugsgebiete zugeschnitten sind, erforderlich.

Um einen besseren globalen Überblick über Karstgrundwasserleiter zu erhalten und eine Grundlage für ein nachhaltiges und internationales Wasserressourcenmanagement zu etablieren, beschäftigte sich der erste Teil dieser Arbeit mit der Kartierung von Karstgrundwasserleitern auf überregionalem Maßstab, und präsentiert die grundlegenden Konzepte und die detaillierte Vorgehensweise bei der Kartierung. Am Beispiel von Frankreich wird der Arbeitsablauf Schritt für Schritt dargestellt, von der Generalisierung über die Differenzierung von Gebieten mit kontinuierlichen und diskontinuierlichen Karbonatgesteinen bzw. Evaporiten, bis hin zur Identifizierung von tiefen und bedeckten Karstgrundwasserleitern. Die Karte zeigt auch ausgewählte Höhlen und Karstquellen, welche in einer assoziierten globalen Datenbank gesammelt werden. Die Karstgrundwasserleiterkarte von Europa zeigt, dass 21.6 % der Landfläche durch (kontinuierliche oder diskontinuierliche) Karbonatgesteinen charakterisiert ist; wobei anstehende Karbonatgesteine auf etwa 13.8 % der Fläche anzutreffen sind.

Anschließend wechselt die vorliegende Arbeit vom globalen zum lokalen Arbeitsmaßstab und fokussiert sich auf ein alpines Karstsystem (Hochifen-Gottesacker), welches durch eine komplexe Hydrogeologie charakterisiert und unter verändernden hydrometeorologischen Bedingungen besonders verletzbar ist. Ein numerisches Modell wurde Schritt für Schritt entwickelt, um die oberflächennahen und unterirdischen hydrologischen Prozesse innerhalb des untersuchten Einzugsgebiets zu simulieren. Das Modell enthält eine Hybrid-Struktur (kombiniert flächen-konzentriertes und -differenziertes Modell) und beinhaltet den Karstgrundwasserleiter und das angrenzende Nicht-Karstgebiet. Zudem sind räumlich verteilte meteorologische Variablen und deren steuernde Schneedynamik im simulierten Einzugsgebiet berücksichtigt. Die

Simulationsergebnisse zeigen, dass das Modell gleichzeitig die hoch dynamische Schüttungsverhalten von vier räumlich verteilten Modellaustritten mit stündlichen Zeitschritten simulieren kann, welche eine permanente Quelle, eine Überlaufquelle, eine Estavelle und den Oberflächenabfluss aus dem Nicht-Karstgebiet darstellen. Zudem werden das duale Fließsystem und das hydrodynamische Verhalten von phreatischen und epiphreatischen Karströhren in der Simulation demonstriert.

Um die Komplexität und Unsicherheit des aufgebauten Modells besser zu verstehen, wurde ein neuartiger mehrstufiger Ansatz für eine Sensitivitätsanalyse entwickelt. Dieser Ansatz wurde für den Modellteil angewendet, welcher das Karstgebiet repräsentiert. Die dabei gewonnenen Informationen über die Parametersensitivität ermöglichten die Identifizierung der räumlichen und zeitlichen Dynamik der Schlüsselparameter. Die Ergebnisse zeigen, dass eine begrenzte Anzahl von räumlich verteilten Parametern das variierende Strömungsschema im Modelbereich kontrolliert. Die Änderung des Strömungsschemas ist vor allem gesteuert durch die Strömungsdynamik in den durchlässigen Zonen des Karstgebiets und den Rückstaumechanismus im Karströhrennetzwerk. Zusätzlich wurden die Wechselwirkungen zwischen den Parametern quantifiziert. Die Ergebnisse zeigen, dass das Modell nichtlinear ist und die einflussreichen Parameter im Modelbereich stark miteinander korrelieren. Die vollständige Sensitivitätsanalyse wurde für den initialen und eingeschränkten Parameterbereich durchgeführt. Der Unterschied zwischen ihnen wurde genutzt, um den Einfluss von Parametereinschränkung auf die Ergebnisse der Sensitivitätsanalyse zu beurteilen. Die Ergebnisse zeigen, dass das räumliche Schema der identifizierten Parametersensitivität und -interaktion stark vom gegebenen Parameterbereich beeinflusst werden.

Der letzte Teil dieser Arbeit beschäftigt sich mit der Untersuchung der Dynamik des Wasserflusses und -speicherung innerhalb des studierten Einzugsgebiets unter historischen und potentiellen, künftigen Klimabedingungen mit Hilfe des bereits entwickelten numerischen Modells. Der weit verbreitete Delta-Ansatz wurde genutzt, um die möglichen Auswirkungen der Klimaveränderungen zu beurteilen. Die Modellsimulation unter dem gegenwärtigen Zustand zeigt, dass ein großer Teil des Niederschlags in den Karstgrundwasserleiter versickert und zum Oberflächenabfluss im benachbarten Nicht-Karstgebiet beiträgt. Der Oberflächenabfluss kann wiederum teilweise in den Karstgrundwasserleiter punktuell infiltrieren. Zudem zeigt das Ergebnis, dass die Oberflächenschneespeicherung von November bis April dominiert, während die unterirdische Wasserspeicherung im Karstgrundwasserleiter von Mai bis Oktober dominiert. Das Klimaszenario zeigt, dass die variierten klimatischen Bedingungen die räumliche und zeitliche Verteilung der Wasserflüsse und -speicherungen deutlich beeinflussen: (1) die gesamte Schüttung des Einzugsgebiets sinkt unter allen evaluierten zukünftigen Klimabedingungen. (2) Das räumliche und zeitliche Schüttungsschema des Einzugsgebiets wird stark durch Temperaturschwankungen gesteuert, welche die saisonale Schneeschmelze zeitlich verlagern können. Die Schneespeicherung in der kalten

Jahreszeit (Dezember bis April) nimmt bei allen Szenarien deutlich ab. (3) Erhöhte Grundwasserneubildung für den Karstgrundwasserleiter im Winter und Frühling und verringerte Grundwasserneubildung im Sommer und Herbst, kompensieren sich teilweise. (4) Die Auswirkungen auf die unterirdische Strömungsdynamik werden durch die dualen Fließwege und die räumlich heterogen verteilte Drainagestruktur im Karst-grundwasserleiter selbst geregelt.

Contents

Contents

Chapter 1

Introduction

1.1. Global distribution of karst aquifers and future water resources availability in karst regions

Karst aquifers form in soluble rocks by flowing groundwater and are characterized by solutionally enlarged fractures, bedding planes and conduits, which form a hydraulically-connected drainage network (Goldscheider and Drew, 2007). Carbonate sedimentary formations including more than 75 % of carbonate minerals, such as limestone and dolomite, are the most important karstifiable rocks (Ford and Williams, 2007). Karst also occurs in other rock types with predominantly carbonatic composition, including carbonatic conglomerates (Göppert et al., 2011) and carbonatic metamorphic rocks (marble, calcite schist) (Skoglund and Lauritzen, 2011). Evaporitic formations, such as gypsum and anhydrite, are also highly karstifiable (Waele et al., 2017). Under exceptional hydro-climatic conditions, karst phenomena can also form in other rock types, such as quartz sandstone or quartzite (Piccini and Mecchia, 2009).

Ford and Williams (2007) estimated that approximately 20 to 25 % of the global population depends largely or entirely on groundwater obtained from karst aquifers. Many karst aquifers are connected over large areas and often form transboundary aquifer systems. A prominent example is the Dinaric Karst System, which is shared between Northeast Italy, Slovenia, Croatia, Serbia, Bosnia and Herzegovina, Montenegro, Macedonia and Albania (Bonacci, 1987). The Mt. Hermon karst aquifer system, which is situated in the border region between Syria, Lebanon and Israel feeds the springs of the Jordan River (Rimmer and Salingar, 2006). One of the world's largest karst regions in Southwest China, covering about 540,000 km², is shared between seven Chinese provinces and extends across the border to Vietnam (Guo et al., 2013). In some countries and regions, such as Austria, the Dinaric region and Southwest China, karst water contributes 50 % or more to regional freshwater supplies (Hartmann et al., 2014; Lu, 2006).

Climate change projections derived from global circulation models (GCMs) suggest significant change to precipitation and temperature regimes in many karst regions (Figure 1.1). The changing climate conditions in the future may have considerable influence on karst water resources, in terms of both quantity and quality (Hartmann et al., 2014). A recent study of Hartmann et al (2015) indicates a significant impact of potential climate change on recharge processes in European karst regions. Alpine karst systems can be especially vulnerable under changing hydro-meteorological conditions since snowmelt in

mountainous environments – itself highly sensitive to varying climatic conditions – is an important controlling process for aquifer recharge. (Finger et al., 2013; Gremaud et al., 2009; Gremaud and Goldscheider, 2010). The changing mountainous precipitation and temperature are likely to substantially affect discharge regime of karst systems and future water availability in their foreland (Finger et al., 2013; Gremaud and Goldscheider, 2010).
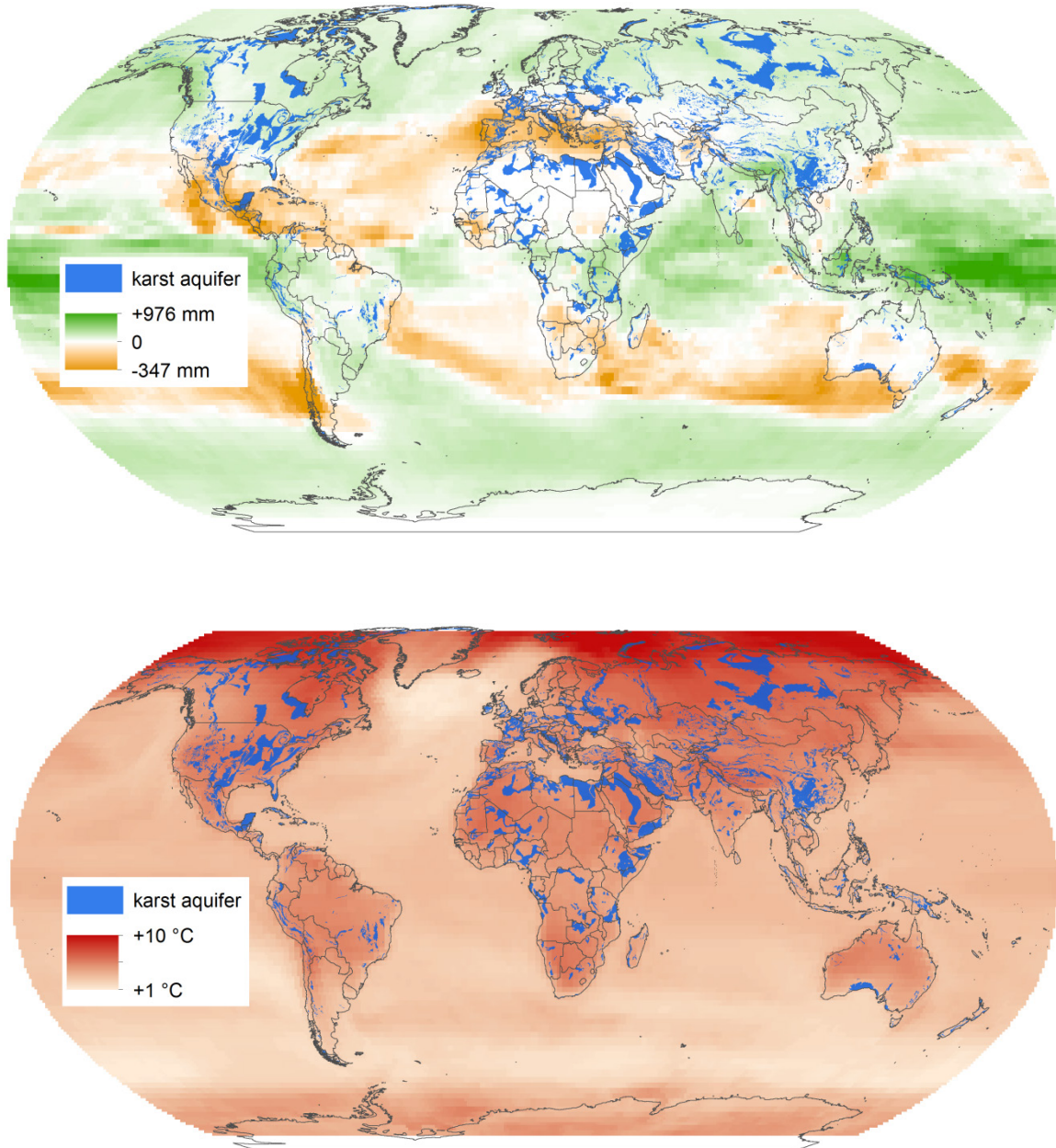
Figure 1.1: Global distribution of karst aquifers (Chen, Goldscheider and WOKAM-Team, work in progress) compared to expected median change of precipitation and temperature by the end of year 2100, scenario A2 from GCMs.

1.2. Conceptual model of karst system and modeling approaches

Karst aquifers are characterized by strong heterogeneity of water flow and storage. In general, karst aquifers can be described as a network of conduits embedded in a matrix of less karstified rock (Goldscheider and Drew, 2007). Flow in conduits is rapid and often turbulent, while flow velocities in the matrix are much lower (Kiraly, 2002). However, water storage in the conduits is often limited, while significant storage may occur in the matrix, and in other parts of the karst system (Ford and Williams, 2007). Recharge into karst aquifers may either originate from the karst area itself (autogenic) or from adjacent non-karst areas (allogenic) (Bakalowicz, 2005). The water may either infiltrate concentrated or diffusely in the epikarst, which is the upper weathered layer of the vadose zone in karst aquifers (Williams, 2008). Within the vadose zone, water is transmitted vertically from the epikarst to the phreatic zone either concentrated and rapidly via vertical shafts, or diffuse and slowly through the fissured matrix. Groundwater flow in the phreatic zone is concentrated in highly conductive conduits. Depending on the distribution of the hydraulic heads, the conduits exchange water with the surrounding matrix.

Previously, various different analytical and numerical approaches have been used to model underground flows through karst aquifers across the world. In principle, the applied models can be distinguished by their description of spatial heterogeneities into lumped parameter models and distributed parameter models. Lumped parameter models are often used to simulate the global hydraulic, physical and/or chemical response of a karst spring to recharge events in the spring catchment (e.g. Butscher and Huggenberger, 2008; Fleury et al., 2007; Hartmann et al., 2012; Jukić and Denić-Jukić, 2009; Scanlon et al., 2003). Such models help to understand the overall water balance and hydrologic dynamics of the karst system including the variability of water quality (Ghasemizadeh et al., 2012). However, spatial variations of flow patterns in the aquifer cannot be considered in this approach. In contrast, distributed parameter models discretize the model domain into a grid of homogeneous sub-units, for which groundwater flow can be described by flow equations derived from basic physical laws. In earlier literatures (Ghasemizadeh et al., 2012; Hartmann et al., 2014; Sauter et al., 2006; Teutsch and Sauter, 1991), the distributed models for karst aquifers are usually classified according to their investigation effort, practical applicability and capability to represent heterogeneities into four different types: 1) Single Continuum Porous Equivalent Model (e.g. Ghasemizadeh et al., 2015; Scanlon et al., 2003; Xanke et al., 2016), 2) Double Continuum Porous Equivalent Model (Kordilla et al., 2012; Lang, 1995; Sauter, 1992; Teutsch, 1988), 3) Hybrid Model (e.g. Kiraly, 1998; Liedl et al., 2003; Reimann, 2009) and 4) Discrete Fracture Set Model (e.g. Dershowitz et al., 2004; Long et al., 1982). Due to the lack of spatially-distributed information on the hydraulic parameter field in karst systems, particularly concerning the location and geometry of the active conduit network, the application of distributed models is often limited to simplified case studies or parameter

studies (e.g. Birk et al., 2005; Liedl et al., 2003; Reimann et al., 2011; Rooij et al., 2013). Moreover, most distributed models focus on the simulation of flow in saturated zone, while recharge and infiltration flow in unsaturated zone are calculated separately. Jeannin (2001) applied a discrete conduit network model to simulate the hydraulics of a variably saturated large cave system in Switzerland. By combining discrete conduit network and infiltration model, Gill et al. (2013) and McCormack et al. (2014) simulated the highly variable hydraulic and hydrologic behavior of a large lowland karst system in Ireland. To assess the complex, spatially heterogeneous hydrological process in a well-studied karst catchment in Germany, Doummar et al. (2012) presented an approach using an integrated catchment model (Mike She). Kraller et al. (2012) used a fully-distributed hydrological model (WaSiM-ETH) to assess the discharge regime of a large Alpine karst catchment. However, in both Mike She and WaSiM models, Darcy's law is applied to simulate groundwater flow in saturated zone, whereas turbulent conduit flow cannot be taken into account. A pragmatic approach presented by Benischke et al. (2010) is to simulate the highly variable discharge behavior of a complex Alpine karst system by combining Mike She and lumped parameter model, whereas the Mike She model simulated recharge and infiltration flow in unsaturated zone and the lumped parameter model described dual flow system in saturated zone.

1.3. Evaluation and identification of distributed karst flow models

Highly parameterized distributed karst flow models can be used to obtain a more comprehensive understanding of spatially heterogeneous karst flow processes (Doummar et al., 2012; Kordilla et al., 2012; Liedl et al., 2003; Oehlmann et al., 2013; Xanke et al., 2016). Because of limited field observations, approximations in the conceptual models, unavoidable errors in measurement data and upscaling effects by using parameters determined at local scale, the estimation of "realistic" parameters throughout the model domain is always associated with uncertainty. To better understand the model parameter uncertainty, we can use sensitivity analysis to evaluate the impact of individual parameters on the model response (Uusitalo et al., 2015). Generally, the sensitivity analysis approaches can be categorized into local and global methods. The local methods aim to assess the impact of change in the parameter values within the local region of indifference on the model output. However, the local nature of these methods inherently limits its ability to identify all potentially relevant features of the response surface (Saltelli, 2004). Alternatively, global methods vary all model parameters in predefined regions to quantify their importance and possible interactions between the individual parameters. The advancement of above mentioned classic sensitivity analysis approaches is to evaluate the dynamic of parameter sensitivity in space and time across the model domain (Wagener et al., 2009a). Often, some of the model parameters will represent processes that only matter in specific locations and during specific time periods (Reusser and Zehe, 2011; van Werkhoven et al., 2008). Such parameters are only likely to be identifiable if these locations and periods can be isolated. Numerous studies based on

different distributed environmental models demonstrated that the obtained information content could be effectively used to identify functioning model parameters and model behavior controlling processes (Herman et al., 2013; Reusser and Zehe, 2011; Tang et al., 2007a; van Werkhoven et al., 2008; Wagener et al., 2009b).

1.4. Objectives

This study aims to give an insight into the complex field of investigation on karst aquifers at global and local scale. The first part of this study is conducted to obtain a better global overview of karst aquifers by creating a world map and database of karst aquifers. Further parts of this study are focused on an Alpine karst system (Hochifen-Gottesacker) which is characterized by complex geology and underground conduit drainage network (Figure 1.2). This includes the development of a distributed numerical model to simulate spatially-distributed surface and subsurface hydrological processes within the investigated karst system. Furthermore, it aims to develop a holistic sensitivity analysis approach suitable for the investigated distributed karst catchment model to comprehensively evaluate and identify the spatiotemporal dynamics of model controls. The last part of this study aims to assess the water fluxes and storages within the studied karst catchment under current and potential future climate conditions by using the proposed numerical modeling approach.
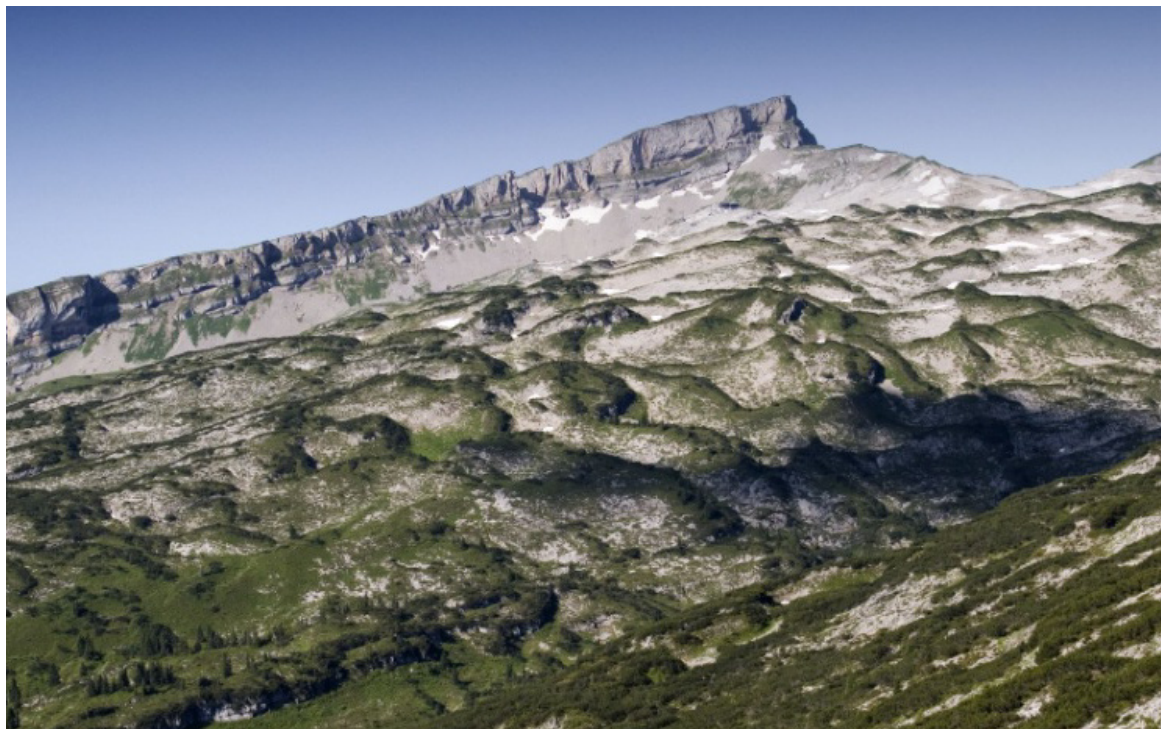
Figure 1.2: View on the summit "Hochifen" and karstic limestone plateau "Gottesacker" in the study region (Photo: Zhao Chen).

1.5. Thesis structure

The presented work is a cumulative dissertation and consists of four individual studies (chapter 2, 3, 4 and 5) and a section with summarized conclusions and outlook (chapter 6). The studies in the chapters 2, 3, and 4 are published in ISI-listed journals and the manuscript in chapter 5 has been recently submitted.

Chapter 2 documents the basic concepts and the detailed mapping procedure, using France as an example to illustrate the step-by-step workflow, which includes generalization, differentiation of continuous and discontinuous carbonate and evaporite rock areas, and the identification of non-exposed karst aquifers. Furthermore it shows selected caves and karst springs, which are collected in an associated global database.

Chapter 3 presents the modeling approach by using a discrete conduit network model to simulate highly variable flow in the studied Alpine karst aquifer system, where the underground drainage pattern is comparatively well known from previous tracer studies. The conduit model was coupled with a reservoir model representing recharge, storage and transfer of water in the epikarst and unsaturated zone. In this study, the global optimization approach was applied to achieve an efficient model calibration.

Chapter 4 introduces a novel multi-step approach based on Sobol's method to evaluate parameter sensitivity as well as interactions with respect to different model outlet points, using different objective functions to assess different hydrodynamic conditions; all varying through time. This complete sensitivity analysis was performed for prior and posterior parameter ranges. The difference between them was used to assess the influence of parameter constraints on the results of sensitivity analyses. This holistic approach was applied to the distributed karst catchment model described in Chapter 3 to evaluate and identify spatiotemporal dynamics of the model controls.

Chapter 5 presents a further development of the existing karst catchment model described in Chapter 3; in particular, linking distributed and timely high resolute snow accumulation/melting routine and extending the model domain to the adjacent non-karst area. Furthermore, a novel calibration strategy by referencing the previous sensitivity analysis study described in Chapter 4 was developed to calibrate the proposed karst catchment model reasonably and effectively. Finally, the water fluxes and storages within the studied karst system and impacts of potential climate change were assessed by using the delta approach combined with random sampling.

Chapter 2

The World Karst Aquifer Mapping Project – Concept, Mapping Procedure and Map of Europe

Abstract

Karst aquifers contribute substantially to freshwater supplies in many regions of the world, but are vulnerable to contamination and difficult to manage because of their unique hydrogeological characteristics. Many karst systems are hydraulically connected over wide areas and require transboundary exploration, protection and management. In order to obtain a better global overview of karst aquifers, to create a basis for sustainable international water resources management, and to increase the awareness in the public and among decision makers, the World Karst Aquifer Mapping (WOKAM) project was established. The goal is to create a world map and database of karst aquifers, as a further development of earlier maps. This report presents the basic concepts and the detailed mapping procedure, using France as an example to illustrate the step-by-step workflow, which includes generalization, differentiation of continuous and discontinuous carbonate and evaporite rock areas, and the identification of non-exposed karst aquifers. The map also shows selected caves and karst springs, which are collected in an associated global database. The draft karst aquifer map of Europe shows that 21.6 % of the European land surface is characterized by the presence of (continuous or discontinuous) carbonate rocks; about 13.8 % of the land surface is carbonate rock outcrop.

2.1. Introduction

According to an often-cited estimation by Ford and Williams (2007), approximately 20 to 25 % of the global population depends largely or entirely on groundwater obtained from karst aquifers. In some countries and regions, such as Austria, the Dinaric region and Southwest China, karst water contributes 50 % or more to regional freshwater supplies (Hartmann et al. 2014, Wu et al. 2009). Several large cities rely entirely or predominantly on karst aquifers, such as San Antonio (1.4 million inhabitants), Vienna (1.8 million), Rome (2.9 million) or Damascus (6 − 7 million) (Al-Charideh 2012, Kresic and Stevanovic, 2010).

Karst aquifers form in soluble rocks by flowing groundwater and are characterized by solutionally enlarged fractures, bedding planes and conduits, which form a hydraulically-connected drainage network (Goldscheider and Drew 2007). Carbonate sedimentary formations including more than 75 % of carbonate minerals, such as limestone and dolomite, are the most important karstifiable rocks (Ford and Williams 2007). Karst also occurs in other rock types with predominantly carbonatic composition, including carbonatic conglomerates (Goeppert et al. 2011) and carbonatic metamorphic rocks (marble, calcite schist) (Skoglund and Lauritzen 2011). Evaporitic formations, such as gypsum and anhydrite, are also highly karstifiable. Under exceptional hydro-climatic conditions, karst phenomena can also form in other rock types, such as quartz sandstone or quartzite (Piccini and Mecchia 2009).

Because of their unique hydrogeological characteristics, karst aquifers are particularly vulnerable to human impacts (Drew and Hötzl 1999) and are difficult to manage (Stevanovic 2015). In exposed karst systems, contaminants can easily enter the subsurface, often via thin soils and open fractures, and rapidly spread in the conduit network. Non-exposed karst aquifers (i.e. concealed, confined or artesian aquifers) are better protected against direct contamination from the land surface. However, contaminant releases from deeper sources can also result in widespread contamination of these valuable freshwater or thermal-mineral water resources (Goldscheider et al. 2010). Because of their hydrogeologic heterogeneity, karst aquifers are difficult to exploit by means of drilling wells, which are often unproductive if they do not succeed in encountering water-bearing fractures, bedding planes or conduits. Historically, karst springs have been more favorable for freshwater abstraction, but they show high fluctuations of both discharge and water quality (Bakalowicz 2005, Kresic and Stevanovic 2010).

Many karst aquifers are connected over large areas and often constitute transboundary aquifer systems. The Dinaric Karst System is shared between northeast Italy, Slovenia, Croatia, Serbia, Bosnia and Herzegovina, Montenegro, Macedonia and Albania (Bonacci 1987, UNESCO-IHP 2013). The Mt. Hermon karst aquifer system, which is situated in the border region between Syria, Lebanon and Israel, feeds the springs of the Jordan

River (Rimmer and Salingar 2006). One of the world's largest karst regions in southwest China, covering about 540,000 km², is shared between seven Chinese provinces and extends across the border to Vietnam (Guo et al. 2013). These examples highlight the need for fully integrating water resources maps.

In the context of international water management under the conditions of climate change and population growth, the need of water resources maps at the global scale becomes even more evident. For example, some previously published maps focus on precipitation and the atmospheric water cycle (Kubota et al. 2007), river networks (Yamazaki et al. 2009), dams and reservoirs (Lehner et al. 2011) or other relevant aspects. A map of "Groundwater Resources of the World" (Richts et al. 2011, WHYMAP 2008) has been prepared within the framework of the World-wide Hydrogeological Mapping and Assessment Programme (WHYMAP) coordinated by UNESCO-IHP (www-1). This map differentiates major groundwater basins, areas with local and shallow aquifers, and areas with complex hydrogeological structure, but does not include explicit information on karst aquifers.

The first relevant world map of carbonate rocks was published by Ford and Williams (1989). A revised version was prepared by Williams and Ford (2006) and used in Ford and Williams (2007). Version 3.0 of this map was elaborated by Paul Williams and Yin Ting Fong and is available online (www-2). This map differentiates between continuous and discontinuous carbonate rock areas. The total global distribution of evaporite rocks, most of which are confined by overlying sedimentary formations, was mapped by Kozary et al. (1968). Hollingsworth (2009) prepared a comprehensive map and database on Karst Regions of the World (KROW) that includes different types of karst (carbonate karst, evaporite karst and pseudokarst), along with other relevant information.

In summary, the existing global groundwater resources map does not display karst aquifers, whereas existing karst maps do not present detailed information on aquifers and groundwater resources, and are also not sufficiently detailed to be presented at the scale of WHYMAP products. Therefore, the World Karst Aquifer Mapping (WOKAM) project was established in 2012 and the map will be printed in 2017. The goal of this project is to prepare a world map of karst aquifers that helps to address global water resources management and to increase the awareness of these valuable but vulnerable freshwater supplies. The World Karst Aquifer Map (the acronym WOKAM is used both for the project and the map) shall be compatible and complementary to other maps of the WHYMAP series, in particular the Groundwater Resources of the World map (Richts et al. 2011). As with other WHYMAP products, the final map shall be printed at two different scales, 1:25 million and 1:40 million, but will also be available in digital form for further usage, such as hydrological modelling attempts at a global scale. As in other WHYMAP products, WOKAM uses the Sphere Robinson projection, which was also used for all maps in this manuscript. The digital Global Lithological Map (GLiM) by

Hartmann and Moosdorf (2012) served as an important basis for WOKAM. GLiM is also available as a printed map (Moosdorf and Hartmann 2015).

WOKAM is a project of the International Association of Hydrogeologists' (IAH) Karst Commission and is financially supported by IAH and UNESCO, in the framework of the WHYMAP programme, with special cooperation of the WHYMAP team at the German Federal Institute for Geosciences and Natural Resources (BGR). The project is coordinated and processed at the Karlsruhe Institute of Technology (KIT). An international Scientific Advisory Board (SAB), composed of the co-authors of this paper, met three times to define the mapping procedure and evaluate the progress of the project. The SAB also contributed to the global collection of data on springs and caves, with the support of numerous colleagues in many different countries (see acknowledgements). The project was implemented using a geographical information system (GIS), but also required many manual work steps.

2.2. Basic mapping approach and legend

The World Karst Aquifer Map is intended to focus on groundwater resources in karst aquifers, which develop primarily in carbonate rocks. Evaporites also constitute important karst systems in some regions, although high sulfate concentrations often hamper their direct utilization as drinking water sources. Based on hydrogeologic observations internationally and a broad supporting literature, rocks that contain at least 75 % of carbonate minerals are typically karstifiable (Ford and Williams 2007). In this paper, the term "carbonate rocks" is exclusively used for such "pure" carbonate rocks. GLiM and other globally available data sources do not provide explicit information on the percentage of carbonate minerals. However, lithological terms, such as limestone, dolomite or chalk, usually indicate "pure" carbonate rocks. Although the actual degree of karstification can vary greatly as a function of different geological and climatological factors (Goldscheider and Drew 2007), it is safe to assume that exposed carbonate rocks are karstified at least to some degree, unless proven otherwise. The following four principal mapping units were defined (Figure 2.1):

- Carbonate rocks (sedimentary or metamorphic)

- Evaporites

- Other sedimentary formations

- Other metamorphic rocks and igneous rocks

Carbonate and evaporite rocks are further subdivided into continuous and discontinuous; the underlying rationale and details of this subdivision are described below. Areas formed by mixed carbonate and evaporite rocks (more than 15 % of each rock type) are also displayed on the map.

**Carbonate rocks
(sedimentary or metamorphic)**
continuous / discontinuous

Evaporites
continuous / discontinuous

**Mixed carbonate
and evaporite rocks**

**Other sedimentary
formations**

**Other metamorphic rocks
and igneous rocks**

**Non-exposed /
exposed karst aquifer**
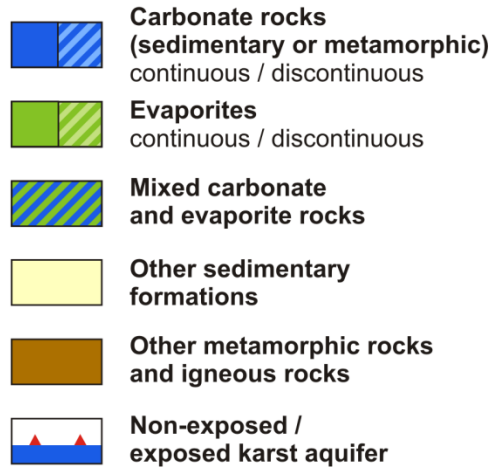
Figure 2.1: Draft legend of the World Karst Aquifer Map, displaying signatures for lithological units. The definition and representation of exposed and non-exposed karst aquifers is illustrated in Figure 2.2.

The mapping units "carbonate rocks" and "evaporites" represent potential karst aquifers. Their actual degree of karstification and hydraulic properties cannot be determined consistently at a global scale. However, it is a defensible approach to assume that most exposed carbonate and evaporitic rocks represent karst aquifers. Biochemical sedimentary formations, such as limestone and dolomite, are the most widespread carbonate rocks. Chalk is a pure but fine-grained biogenic carbonate rock and often not considered to be karstifiable. However, many chalk aquifers are actually karstified, although karst features are less prominent than in classical limestone karst. In many regions, chalk aquifers contribute substantially to freshwater supplies (Maurice et al., 2006). Metamorphic carbonate rocks, such as marble and calcite schist, also constitute important karst aquifers in some regions of the world. There is a smooth transition between diagenesis and metamorphosis and thus between sedimentary and metamorphic rocks. Therefore, this mapping unit includes the whole range of carbonate rocks, as defined above (i.e. more than 75 % carbonate minerals).

The mapping unit "other sedimentary formations" includes both consolidated and unconsolidated rocks, mostly non-carbonate siliciclastic formations, such as alluvial sediments and sandstone, but also mixed rock types (typically with less than 75 % carbonate minerals), such as marl. This generalization was done to keep the map simple and to overcome inconsistencies at national borders on the GLiM map. Areas where other sedimentary formations outcrop at the land surface may include karst aquifers at greater depth. Zones where exposed carbonate rocks plunge under adjacent other sedimentary formations are highlighted by a line of red triangles pointing to the direction of non-exposed carbonate rocks (Figure 2.2). No attempt is made to characterize those areas, beyond identifying their presence, which may include deep or artesian karst aquifers with fresh or thermal-mineral water. Exposed carbonate rocks usually form karst landscapes

with more or less developed karst landforms, such as dolines, and intense surface-groundwater interaction. This is usually not the case for non-exposed carbonate rocks, unless the overlying formations are very thin.
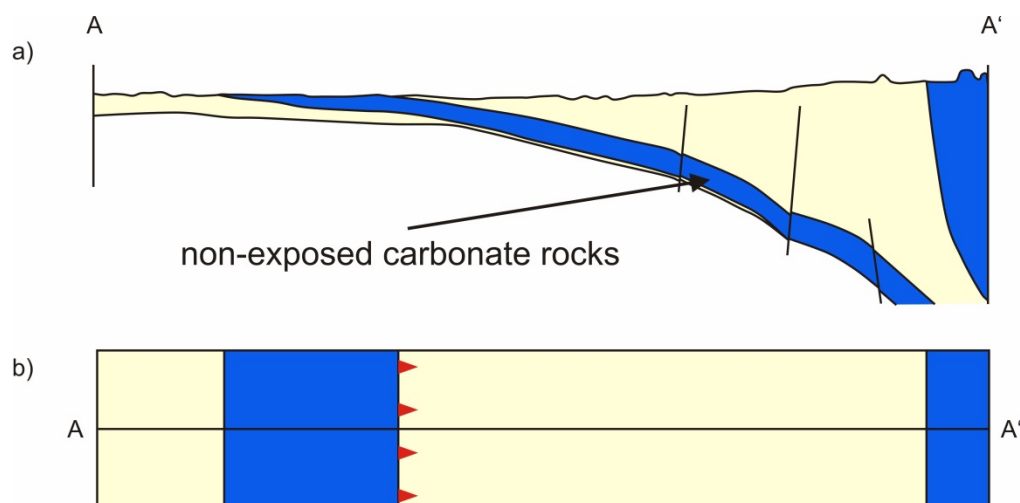
Figure 2.2: Illustration of non-exposed karst aquifers: a) Cross-section; b) Plan view; The line of red triangles points to the direction of non-exposed carbonate rocks, but the plan view map does not provide detailed information concerning the areal extent or depth of these deep aquifers; legend see Figure 2.1.

Crystalline rocks comprise igneous rocks and metamorphic rocks, which can be subdivided into metasediments and meta-igneous rocks. Metasediments include karstifiable metamorphic carbonate rocks, which belong to the mapping unit "carbonate rocks," as described above. Therefore, the last mapping unit includes "other metamorphic rocks", such as gneiss, amphibolite and different types of schist, and igneous rocks, which encompass plutonic rocks, such as granite and diorite, and volcanic rocks, such as basalt, andesite and rhyolite. Some volcanic rocks, particularly basaltic lava flows with cooling fractures and lava tubes, show similar hydraulic properties to carbonate rocks (Kauahikaua et al., 1998), but they are usually not classified as karst aquifers and not delineated on WOKAM. The detailed work-steps from GLiM to WOKAM are described further in the following.

As the World Karst Aquifer Map is intended to provide relevant information for water resources management, selected important karst springs, wells and other water abstraction structures are also presented on the map. The presence of such springs and other karst water sources is also clear evidence for the existence of high-yielding karst aquifers. Therefore, the presentation of springs on the map is also an indirect way of indicating the hydraulic properties of the karst aquifers. Additionally, the map displays selected caves, because caves are characteristic of karst and generally represent the degree of karstification, which cannot be mapped otherwise at a global scale. The selection criteria for caves considers their hydrological importance, i.e. caves related to relevant water resources are preferentially presented on the map. The detailed selection criteria and the structure of the spring and cave database are described further in the following.

2.3. Detailed mapping procedure

2.3.1. Database and workflow

The major challenge in preparing the World Karst Aquifer Map is the extremely heterogeneous cartographic databases. The Global Lithological Map (GLiM) by Hartmann and Moosdorf (2012) was assembled from 92 regional geological maps (typically national maps) with different scales and mapping units, which were merged in a geographical information system (GIS). GLiM achieved a consistent legend by regrouping and reclassifying the numerous mapping units of the regional maps, while keeping much of the more detailed basic information in the associated database, which includes three levels of information. However, as GLiM was initially not intended to be published as a printed map, it does not have a defined and consistent scale, and the map was not generalized. Furthermore, the authors of GLiM did not attempt to correct the available maps, which also means that there are some inconsistencies at state borders in terms of spatial delineation of polygons and their geologic attribution. In order to achieve a globally consistent World Karst Aquifer Map suitable for printing at defined scales (1:25 million and 1:40 million), a well-defined work flow at a consistent working scale of 1:10 million was established and implemented (Figure 2.3).
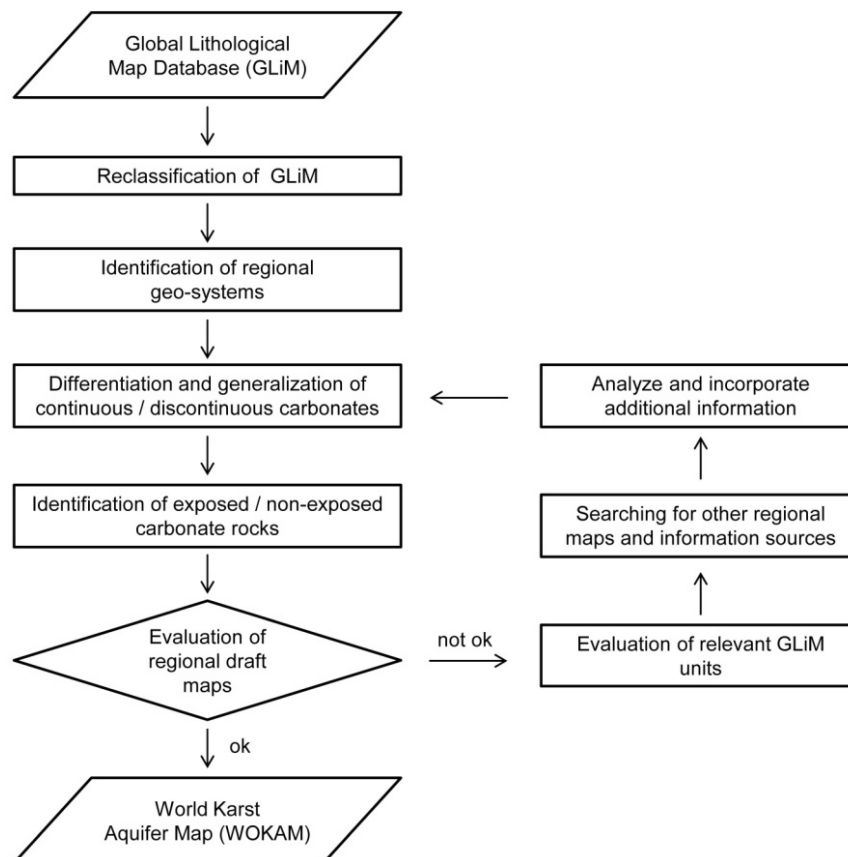
Figure 2.3: Work flow of the mapping procedure from the Global Lithological Map (GLiM) to the World Karst Aquifer Map (WOKAM).

2.3.2. Reclassification of mapping units

Figure 2.4 displays the Global Lithological Maps with its 13 lithological first-order mapping units and a detail of the map that is used as an example area to illustrate the detailed work steps from GLiM to WOKAM. The first step (illustrated in Figure 2.4c) is the reclassification of the 13 GLiM units into the four principal WOKAM mapping units, as follows (the symbols are explained in the caption of Figure 2.4):

- SC into "carbonate rocks"

- EV into "evaporites"

- SU, SS, SM and PY into "other sedimentary formations"

- MT, PA, PI, PB, VA, VI and VB into "other metamorphic rocks and igneous rocks"

As a first approximation, the resulting map nicely displayed the distribution of carbonate rocks (Figure 2.4c) but still included several problems: 1) Some important carbonate rock and karst areas were not displayed, as they were hidden in the GLiM mapping unit "mixed sedimentary rocks" (SM); 2) Some regionally important metamorphic carbonate rocks were entirely missing; 3) There was no uniform scale and no consistent generalization. Therefore, additional work steps were required.

2.3.3. Differentiation and generalization of continuous and discontinuous carbonates

The evaluation of available GIS options revealed that a hydrogeologically meaningful generalization could not be done in an automatized way, but required hydrogeological expertise and manual processing. In order to achieve a spatial framework for generalization, the map was divided into regional geo-systems based on the US Geological Survey (USGS) map of Geologic Provinces of the World (www-3) (Figure 2.5). A geo-system is defined as a spatial entity with common geologic and geomorphologic attributes.
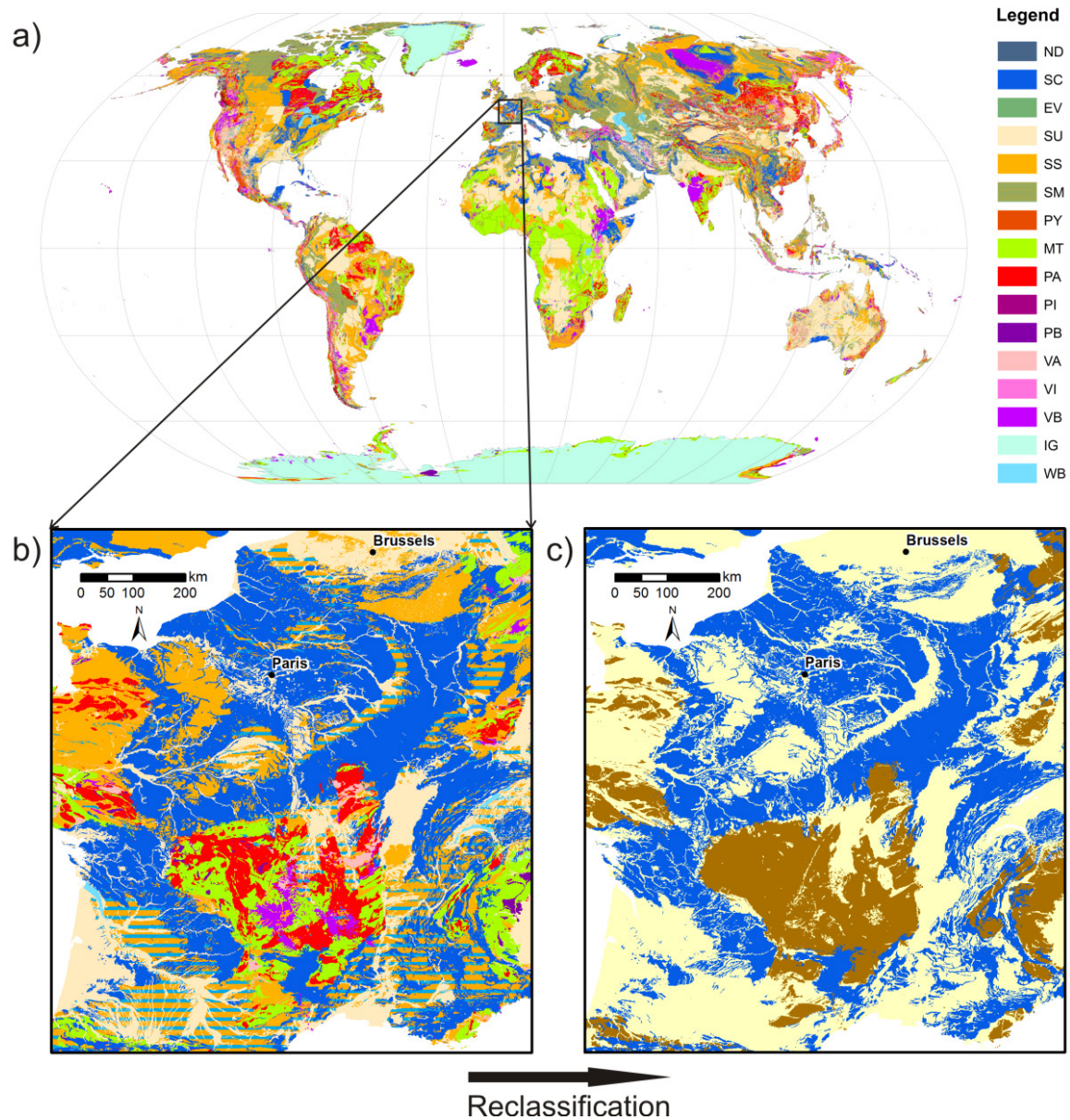
Figure 2.4: a) Original GLiM map and mapping units (ND: No data, SC: Carbonate sedimentary rocks, EV: Evaporites, SU: Unconsolidated sediments, SS: Siliciclastic sedimentary rocks, SM: Mixed sedimentary rocks, PY: Pyroclastic rocks, MT: Metamorphic rocks, PA: Acid plutonic rocks, PI: Intermediate plutonic rocks, PB: Basic plutonic rocks, VA: Acid volcanic rocks, VI: Intermediate volcanic rocks, VB: Basic volcanic rocks, IG: Ice and glaciers and WB: Water bodies); b) Detail of GLiM for the example area; c) Reclassification into WOKAM mapping units; legend see Figure 2.1.
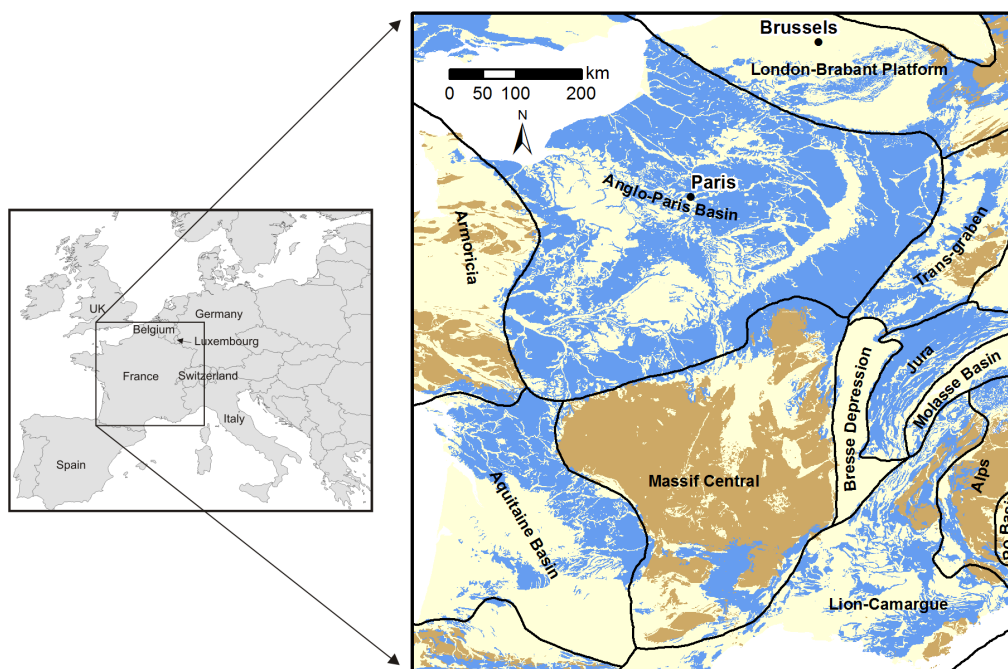
Figure 2.5: Identification of regional geo-systems based on USGS (www-3), which are used as a basis for hydrogeologically meaningful generalization; for legend see Figure 2.1.

Integrative generalization of the map was done manually, at a consistent working scale of 1:10 million. An inherent problem in generalization is the existence of outcrops that are too small to be displayed individually, but too important to be ignored. To overcome this problem, carbonate (and evaporite) areas were subdivided into continuous and discontinuous, based on an area's share of the respective rock type. Wherever possible, the mapping unit "continuous" was applied, even for small polygons, because this is straightforward and readily understood. Polygons classified as "continuous" often include small patches or thin strips of non-karst surfaces that are too small to be displayed on the generalized map. By comparing the original, non-generalized polygons with the generalized ones, it turned out that the share of carbonate rocks was generally larger than 65 %, so this threshold was taken as lower limit for "continuous" carbonate rocks. Some areas contain many tiny, scattered or ramified carbonate rock polygons that cannot be displayed individually on the generalized map. Therefore, the mapping unit "discontinuous" was introduced. By testing this approach in several regions, it turned out that the limits of 15 % and 65 % result in a meaningful generalization, both scientifically and in terms of graphical presentation. Therefore, areas with more than 65 % of carbonate (or evaporite) rock were mapped as "continuous," whereas areas between 15 and 65 % were mapped as "discontinuous." However, because of the heterogeneity of the underlying database, and due to the diversity and complexity of different geological provinces, this general rule had to be adapted individually during the process of manual generalization, while consulting available geological and hydrogeological literature for the respective regions. Figure 2.6 illustrates the differentiation of areas of "continuous" and "discontinuous" carbonate rock during generalization; some of the hydrogeologically

important but geologically complex and spatially compartmentalized karst systems in southern France are mapped as a region of discontinuous karst.
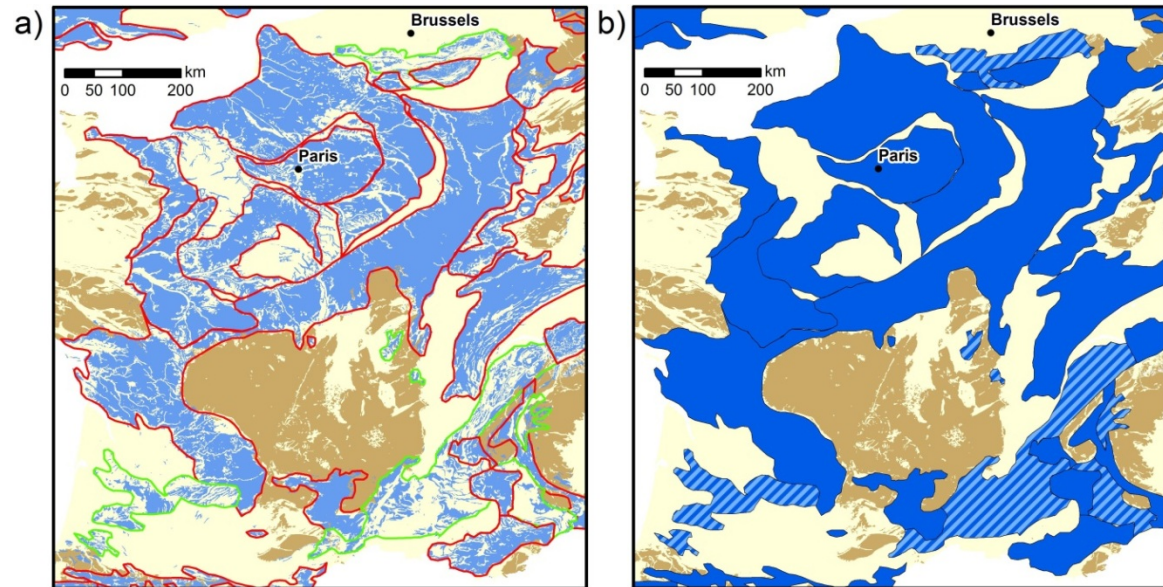
Figure 2.6: Differentiation of continuous and discontinuous carbonate rocks during the process of manual generalization at a working scale of 1:10 million: a) Original polygons with red and green lines that were used to delineate areas of continuous and discontinuous carbonate rocks; b) Generalized polygons; legend see Figure 2.1.
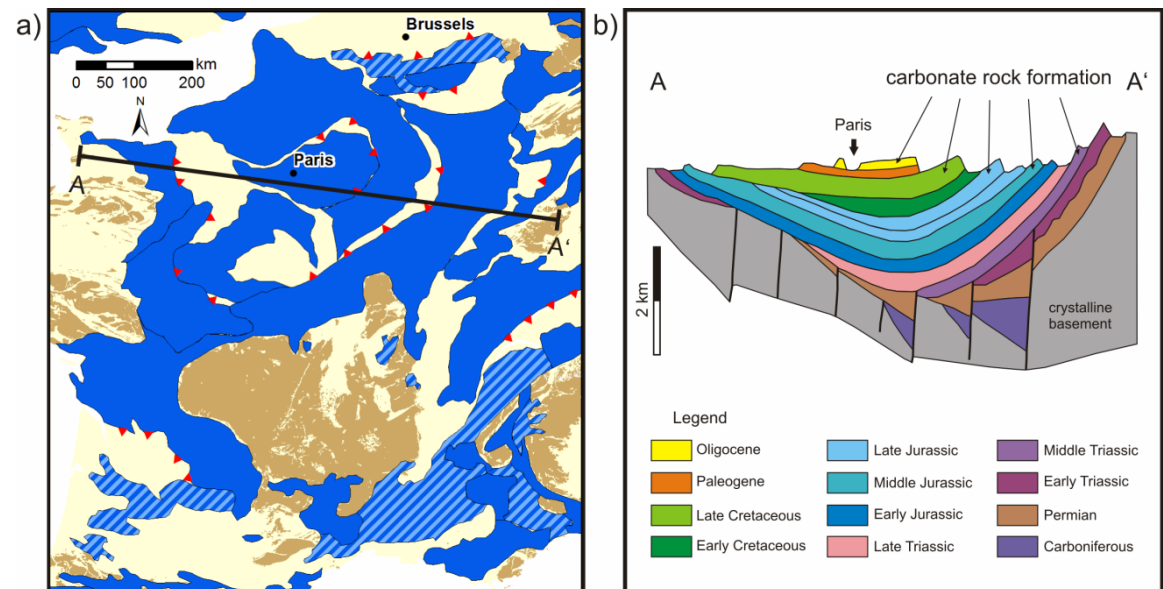
Figure 2.7: Identification and presentation of non-exposed karst aquifers on the map, exemplified by the Paris Basin: a) Karst aquifer map of France, where the red triangles point toward non-exposed carbonate rocks, illustrating the basin structure in this regionally important multi-karst-aquifer system; b) Geologic profile across the Paris Basin (after Beccaletto et al., 2011) that was used to identify non-exposed karst aquifers in this geo-province.

2.3.4. Identification of non-exposed carbonate rocks

The next step was the identification and presentation of non-exposed carbonate rocks, which constitute potential deep and confined aquifers, as illustrated in Figure 2.2. As this work step requires three-dimensional geological analysis, it could not be implemented automatically on the basis of two-dimensional information available in the GLiM database. Therefore, the geological setting of all relevant karst areas was assessed manually on the basis of the geo-system approach illustrated in Figure 2.5. Regional geological maps, profiles and literature were consulted for all geo-systems in order to identify regionally important non-exposed karst systems, such as the Paris Basin highlighted in Figure 2.7.

2.3.5. Evaluation and iterative improvement of the map

At different stages of the mapping procedure, the intermediate results were discussed by the SAB and sent to regional experts for evaluation and correction. In the case of negative evaluations, the map was further improved by searching and consulting additional and more accurate maps and information sources for the respective region until a satisfactory result was achieved (Figure 2.3). It turned out that many polygons needed to be reclassified and rearranged. In particular, the initial delineation of carbonate rock areas was often insufficient, because many important karst areas were hidden under "mixed sedimentary rocks" (SM), and some areas consisting of "metamorphic rocks" (MT) also include large areas of carbonatic meta-sediments. For most countries and regions, it was possible to make these corrections based on GLiM. For other countries, GLiM was largely replaced by information obtained from regional or national maps. This was the case for Bulgaria (Beron et al. 2006), Hungary (www-4), Italy (Sivelli and De Waele 2013), Moldova (Duscher et al. 2015), Portugal (Almeida et al. 1995), Romania (Orăşeanu and Iurkiewicz 2010), Serbia (Stevanovic and Jemcov 1996), Slovenia (Ravbar & Šebela 2015), Spain (Ayala-Carcedo 1986), Switzerland (Jeannin 2016), and Ukraine (Alexander Klimchouk, personal communication, 2016).

2.4. Karst water sources and cave database

2.4.1. Karst water sources database

Several textbooks include tables or other information on major karst springs in the world (e.g. Ford and Williams 2007; Kresic and Stevanovic 2010) or in specific regions or countries. However, for the preparation of a world karst aquifer map, the available information was insufficient. Therefore, a systematic global database on springs and other karst water sources was established in the framework of the WOKAM project. The major inherent challenges in creating this database were:

1. The amount and quality of available data and information for different countries is extremely variable (e.g. excellent data for Switzerland, almost no data for Africa);

2. The frequency and size-range of springs is also extremely unevenly distributed (e.g. many large springs in the Dinaric Karst, very few large springs in South America and Africa).

Only a limited amount of information can be displayed on a global map, whereas it is possible and useful to establish a detailed global database of karst water sources. Therefore, we followed a pragmatic approach: 1. Detailed data collection for the database (in progress); 2. Generalized presentation of selected karst water sources on the map. A template for data collection was designed and sent to SAB members and regional experts. The template allows inclusion of the following information: name and type of object (e.g. normal karst spring, thermal spring, submarine spring, water well), country and region, coordinates and altitude, relevant discharge data, information on water chemistry and temperature, information on aquifer geology, regional significance, comments, references.

Many karst springs are characterized by high variations in discharge; some springs run dry during droughts but have extremely high maximum discharges (often > 100 m³/s) following periods of high precipitation. However, in terms of water resources, the permanent (i.e. minimum) spring discharge is the most relevant quantity. In some remote and humid karst regions, many large karst springs are often not used (and sometimes not even known), whereas a relatively small karst spring in an arid region might be extremely important and well known (e.g. the springs of the Jordan River).

Based on these considerations, two main criteria were applied for inclusion of a particular karst water source on the map: the low-flow discharge of the spring (or pumping rate of the well), and its regional significance. The low-flow discharge is ideally calculated as the average annual minimum discharge, based on long-term data series. However, in most cases, such time series are not available. For many springs (e.g. in China and South America), only a single value is available, often measured during the dry season. In these cases, the dry season discharge is taken as low-flow discharge. The regional significance was determined by means of expert judgement, taking into account a combination of objective and subjective criteria. This prioritization by regional experts helped to decide whether or not a particular spring would be included in the final map.

The final map will include the following types of springs: selected karst springs with low-flow discharge ≥ 2 m³/s, selected springs with low-flow discharge < 2 m³/s, selected water wells and other abstraction structures, selected submarine springs, selected thermal and mineral springs.

Depending on the printing scale, the final selection of springs and wells will be adapted. For special maps that might be published later (e.g. karst map of a particular continent,

country or region; thematic special maps), the existing detailed database can be used and complemented, and the criteria for inclusion on the map can be adapted accordingly. For example, based on the WOKAM spring database, Stevanovic et al. (2016) have published regional karst water sources maps for South East Europe, Near and Middle East and Eastern Africa.

2.4.2. Cave database

Several books (e.g. Palmer and Palmer 2009, Courbon 1989, Laumanns 2002) and internet resources (www-5) present useful information on the longest and deepest caves in the world or in particular regions or countries. Although the focus of WOKAM is not on caves but on water resources, caves will also be displayed on the final map, insofar as caves deliver information on the degree of karstification, although there is no simple and straightforward relation between cave development and karst aquifer properties (Palmer, 1991). The global distribution of caves is even more heterogeneous than the distribution of springs, because the regional frequency, length and depth of caves also reflect the degree of exploration, which varies hugely between countries. In some small European countries, such as Switzerland or Slovenia, there are thousands of mapped caves, including large ones, whereas large carbonate rock areas in some remote regions of our planet have almost no known caves. This uneven spatial distribution and degree of information makes it very difficult to define strictly objective and applicable criteria for the selection of caves for the world karst aquifer map; therefore, a pragmatic weighting and rating approach was established, taking into account the dimensions of the cave (mapped length and depth), and its hydrological significance, role for human use and ecosystems, and regional significance (Table 2.1).

Table 2.1: Rating system for cave data evaluation: 5 out of 10 points are related to the dimensions of a cave, which always reflects the degree of exploration; the remaining 5 points are assigned for different aspects describing the significance of the cave and its associated water resources. Touristic or archeological values are not considered.

Rating section	Rating pts	Rating criterion
Length	0	< 10 km
	1	10-50 km
	2	50-100 km
	3	> 100 km
Depth	0	< 500 m
	1	500-1000 m
	2	> 1000 m
Hydrological significance	0	No particular hydrological relevance (mostly dry cave)
	1	Associated with relevant springs, swallow holes or cave streams
	2	Associated with major spring, sinking stream or underground river
Significance for human use and ecosystems	0	No particular importance
	1	Cave water (spring / stream) has major importance for human use and/or ecosystems
Regional significance	0	Low to moderate regional significance
	1	High (e.g. deepest cave in the Alps)
	2	Very high (e.g. longest cave in Africa, deepest cave in the world, only available water resource in a large region)

Depending on the scale of the final map, different thresholds can be defined for including caves from the database, e.g. six points could be the minimum value for inclusion on the 1:25 million map. Table 2.2 illustrates this point-count system by means of five examples. Some caves (e.g. Siebenhengste-Hohgant System in Switzerland) are primarily included on the map because of their dimensions (> 100 km long and > 1000 m deep); other caves (e.g. Sof Omar Cave in Ethiopia) are included because of their regional significance (longest cave in Africa), hydrological significance (a river flows through this cave) and its importance for human use and ecosystems (Asrat 2015).

Table 2.2: Application of the rating system in Table 2.1, exemplified by five important caves in Europe, the USA and Africa.

Name	Country	Length [km]	Depth [m]	Weighted rating system for evaluation					
				Length	Depth	Hydrological significance	Human use & ecosystems	Regional siginificance	SUM
				0 - 3 pts	0 - 2 pts	0 - 2 pts	0 - 1 pts	0 - 2 pts	0 - 10 pts
Blauhöhle	Germany	10.5	130	1	0	2	0	1	4
Riesending	Germany	19.2	1148	1	2	1	0	1	5
Mammoth Cave	USA	643.7	124	3	0	2	1	2	8
Siebenhengste-Hohgant Cave System	Switzerland	157.0	1340	3	2	1	0	1	7
Sof Omar Cave	Ethiopia	15.1	15	1	0	2	1	2	6

2.4.3. Karst aquifer map of France with springs and caves

The selection and cartographic presentation of significant springs and caves is illustrated for the example region (France) in Figure 2.8; Table 2.3 presents a summary of these selected objects. Springs are characterized by their low-flow and high-flow discharge (m³/s); for caves, the surveyed lengths (km) and depths (m) are indicated.
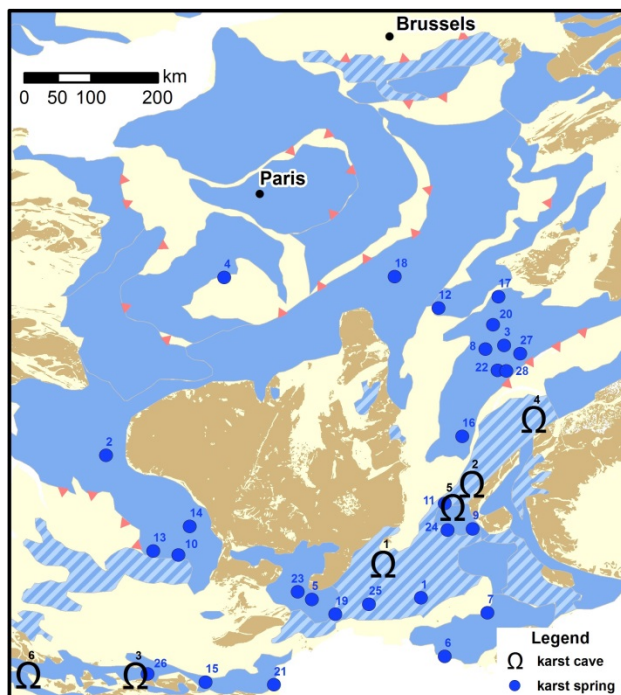
Figure 2.8: Draft karst map of the example area (France) with presentation of selected springs and caves, which are summarized in Table 2.3.

Table 2.3: Summary of selected springs and caves in France, shown on the map in Figure 2.8. Quantitative estimations for low-flow and high-flow discharge (m³/s) are indicated for springs; caves are characterized by length (km) and depth (m).

ID	Name of spring	low [m³/s]	high [m³/s]
1	Vaucluse spring	4.0	150
2	Touvre spring	6.0	40
3	Loue spring	0.9	75
4	Bouillon spring	2.5	20
5	Foux de la Vis spring	1.2	245
6	Port-Miou submarine spring	3.0	50
7	L'Evêque spring	2.3	19
8	Lison spring	0.4	91
9	Gillardes spring	3.0	60
10	Chartreux spring	1.0	50
11	Arbois spring	1.7	40
12	Bèze spring	0.9	25
13	Source Bleue and related springs	2.0	5
14	Ouysse spring	0.6	200
15	Fontestorbes spring	0.6	15
16	Groin spring	0.0	104
17	Font de Champdamoy spring	0.2	18
18	Douix spring	0.6	3

ID	Name of spring	low [m³/s]	high [m³/s]
19	Lez spring	0.1	16
20	Arcier spring	0.2	10
21	Font Estramar spring	0.8	25
22	Doubs spring	0.2	19
23	Durzon spring	1.0	20
24	Archiane spring	0.1	21
25	Fontaine de Nîmes spring	0.0	18
26	Aliou spring	0.0	32
27	Areuse spring	0.7	39
28	Orbe spring	2.0	80

ID	Name of cave	length [km]	depth [m]
1	Saint-Marcel d'Ardéche cave	51.2	233
2	Dent de Crolles cave system	50.1	673
3	Coume Ouarnède cave system	105.8	975
4	Jean Bernard cave system	20.5	1602
5	Clot d'Aspres cave system	40.0	1066
6	Pierre Saint-Martin cave system	80.2	1408

2.5. Draft Karst Aquifer Map of Europe

Figure 2.9 presents The draft karst aquifer map of Europe in the preliminary design of WOKAM at a scale of 1:25 million, using the Sphere Robinson projection. The map is presented without springs and caves, as the database has not yet been completed for all European countries. Based on the statistical evaluation of this map, it is possible to determine the areas of carbonate rocks. For this analysis, the map projection was changed to Eckert IV (equal area). Table 2.4 presents the absolute surfaces (in 1000 km²) and the percentage of carbonate rock areas in all European countries and in Europe as a whole. The table differentiates between "continuous" and "discontinuous" carbonate rock areas, as defined in WOKAM, and also presents the sum of both, i.e. the total area characterized by the presence of (continuous or discontinuous) carbonate rocks. The surface of actual carbonate outcrops is also presented and was obtained from the non-generalized polygons.

According to this analysis, 15.2 % of the land surface consists of "continuous carbonate rocks" and 6.4 % consists of "discontinuous carbonate rocks." Accordingly, 21.6 % of the European land surface is characterized by the presence of carbonate rock, most of which is karstified and forms karst aquifers. The total area share of actual carbonate rock outcrops (generally derived from the non-generalized polygons) is about 13.8 %. The areas of non-exposed karst aquifers cannot be delineated precisely, but the map allows identification of their locations. These numbers include all uncertainties involved in the entire process of generating the map—from the initial mapping in the field to the final classification and generalization in WOKAM.

In 1995, the European Cooperation in Science and Technology (COST) Action 65 prepared a draft map of carbonate rock outcrops in Europe and estimated that 35 % of the European land surface consist of carbonate rocks (COST Action 65, 1995). The main reason for the discrepancy is that WOKAM is based on a much better cartographic database and differentiates between areas of discontinuous and continuous carbonate rocks, taking into account the actual surface areas of carbonate rocks.
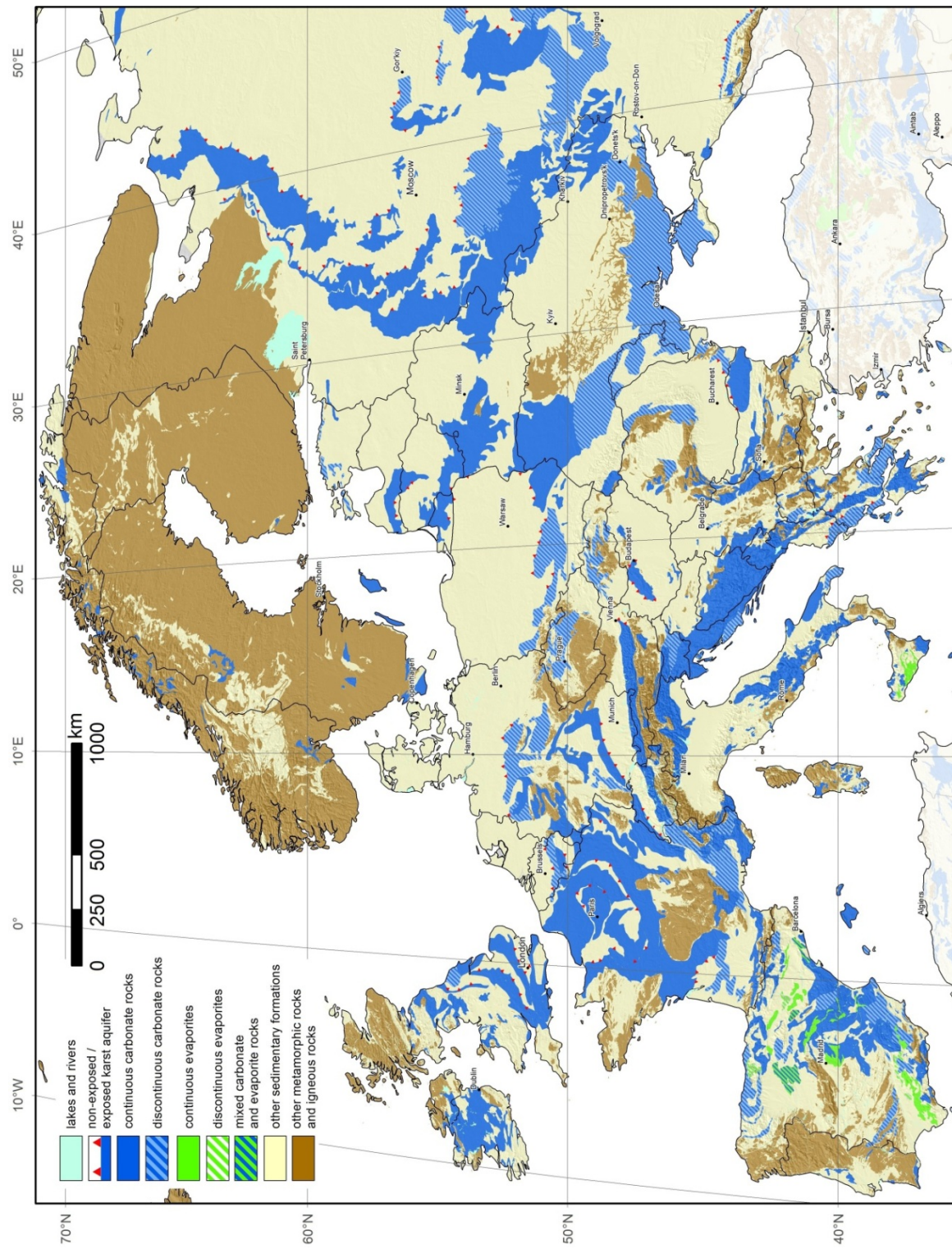
Figure 2.9: Draft Karst Aquifer Map of Europe, as an example of the World Karst Aquifer Map.

Table 2.4: Estimated distribution of carbonate rocks in all European countries, differentiated in continuous (> 65%) and discontinuous (15 – 65%) carbonate rock, as presented on the map in Figure 2.9. The area of actual carbonate outcrops (derived from the non-generalized polygons) is also presented. Uncertain data are shaded and marked in italics.

Country		Carbonate rock areas							
Name	1000 km²	continuous		discontinuous		sum (CC + DC)		outcrops	
		1000 km²	%	1000 km²	%	1000 km²	%	1000 km²	%
Albania	28,7	9,9	34,6	4,1	14,4	14,1	49,0	9,8	34,3
Andorra	0,5	0,0	0,0	0,0	0,0	0,0	0,0	0,0	0,0
Austria	83,9	23,7	28,2	0,0	0,0	23,7	28,2	20,9	25,0
Belarus	*207,3*	*66,1*	*31,9*	*0,0*	*0,0*	*66,1*	*31,9*	*52,1*	*25,1*
Belgium	30,6	3,6	11,8	5,9	19,4	9,5	31,1	3,8	12,5
Bosnia & Herzegovina	51,5	39,9	77,5	0,0	0,0	39,9	77,5	31,2	60,5
Bulgaria	111,1	30,2	27,2	0,2	0,2	30,4	27,4	30,1	27,1
Croatia	55,9	23,5	42,0	4,7	8,5	28,2	50,5	22,8	40,9
Czech Republic	78,7	0,0	0,0	15,0	19,0	15,0	19,0	7,2	9,2
Denmark	42,6	0,0	0,0	0,0	0,0	0,0	0,0	0,0	0,1
Estonia	*45,8*	*0,5*	*1,2*	*4,3*	*9,4*	*4,9*	*10,6*	*1,1*	*2,4*
Finland	333,9	0,2	0,1	0,0	0,0	0,2	0,1	0,2	0,1
France	547,9	227,8	41,6	44,0	8,0	271,8	49,6	191,9	35,0
Germany	356,7	48,5	13,6	33,7	9,4	82,1	23,0	44,9	12,6
Greece	130,2	30,0	23,0	23,4	18,0	53,4	41,0	35,3	27,1
Hungary	92,9	8,8	9,5	0,4	0,4	9,2	9,9	3,9	4,2
Iceland	102,5	0,0	0,0	0,0	0,0	0,0	0,0	0,0	0,0
Ireland (Republic)	69,5	32,4	46,6	0,0	0,0	32,4	46,6	23,9	34,4
Italy	300,2	78,6	26,2	5,8	1,9	84,4	28,1	57,4	19,1
Latvia	*64,5*	*8,6*	*13,3*	*0,0*	*0,0*	*8,6*	*13,3*	*7,7*	*12,0*
Liechtenstein	0,2	0,2	96,5	0,0	0,0	0,2	96,5	0,1	51,1
Lithuania	*64,9*	*18,6*	*28,6*	*0,0*	*0,0*	*18,6*	*28,6*	*15,7*	*24,1*
Luxembourg	2,6	1,7	66,1	0,0	0,0	1,7	66,1	1,6	61,1
Malta	0,3	0,3	93,8	0,0	0,0	0,3	93,8	0,3	93,8
Montenegro	13,8	11,7	85,3	0,0	0,0	11,7	85,3	11,0	80,1
Netherlands	34,9	0,0	0,0	0,3	0,8	0,3	0,8	0,1	0,2
Norway (incl. Svalbard)	382,1	12,1	3,2	1,0	0,3	13,1	3,4	10,0	2,6
Poland	311,2	15,8	5,1	30,6	9,8	46,4	14,9	21,6	6,9
Portugal	91,3	3,5	3,8	0,4	0,4	3,8	4,2	3,7	4,0
Republic of Macedonia	25,5	2,2	8,6	3,0	11,8	5,2	20,4	3,2	12,4
Republic of Moldova	*33,7*	*0,0*	*0,0*	*16,5*	*49,1*	*16,5*	*49,1*	*6,0*	*17,8*
Romania	237,3	6,3	2,7	21,0	8,8	27,3	11,5	5,5	2,3
Russia (Europ. part)	*4002,0*	*495,7*	*12,4*	*193,2*	*4,8*	*688,8*	*17,2*	*454,3*	*11,4*
Serbia and Kosovo	88,2	16,9	19,2	0,8	1,0	17,8	20,1	15,8	17,9
Slovakia	48,9	0,2	0,5	10,2	20,8	10,4	21,3	4,3	8,9
Slovenia	20,4	10,3	50,6	5,8	28,5	16,2	79,2	10,1	49,5
Spain	499,1	96,3	19,3	49,5	9,9	145,7	29,2	70,6	14,1
Sweden	444,3	14,7	3,3	0,0	0,0	14,7	3,3	12,4	2,8
Switzerland	41,5	14,8	35,7	1,1	2,6	15,9	38,3	7,9	19,0
Turkey	23,8	1,7	7,2	0,0	0,0	1,7	7,2	1,7	7,2
UK (incl. N. Ireland)	243,8	64,2	26,3	3,5	1,5	67,7	27,8	51,1	21,0
Ukraine	*597,0*	*90,1*	*15,1*	*156,6*	*26,2*	*246,7*	*41,3*	*123,4*	*20,7*
Europe	**9941,7**	**1509,8**	**15,2**	**635,1**	**6,4**	**2144,8**	**21,6**	**1374,8**	**13,8**

2.6. Conclusions

Karst is an expansive terrain that occurs on all continents. Its aquifers produce the world's largest springs while being the most vulnerable to contamination. Karst aquifers often cross international boundaries but until recently, the boundaries of karst were often poorly defined. Building on the Global Lithological Map (Hartmann and Moosdorf 2012) and growing databases and exploration of karst, and through the use of versatile GIS technology, the first World Karst Aquifer Map (WOKAM) is nearing completion. This paper describes the basic concepts and procedure of this world-wide mapping effort and examines a subset of the World Karst Aquifer Map by focusing on Europe.

WOKAM is prepared at a consistent working scale of 1:10 million and differentiates between areas of "continuous carbonate rocks" (typically > 65 % carbonate rock outcrops) and "discontinuous carbonate rocks" (typically 15 – 65 % outcrops). The updip boundaries of non-exposed karst aquifers are also delineated on WOKAM. The map and associated database include selected karst springs, wells and other freshwater abstraction structures, and selected caves.

As a well-studied continent with rich sources of information, Europe was an ideal region to test, refine, and prove the mapping concepts for WOKAM. Prior estimates that carbonate rock outcrops cover 35 % of Europe were found overestimates by the more accurate WOKAM process. We found that about 21.6 % of the European land surface is characterized by the presence of carbonate rock, including 15.2 % of "continuous" and 6.4 % of "discontinuous carbonate rocks". The total areas of actual carbonate rock outcrops is about 13.8 %. Much of this occurs beneath some of the continent's most densely populated regions where effective water resources management is especially critical, such as England, northern and southern France, parts of Germany, central Italy, and eastern Spain.

The georeferenced GIS structure of WOKAM and the associated database will allow its relatively easy updating and will make it possible to prepare specific maps by combining information presented on WOKAM with other relevant information, such as climate and global change, agriculture and irrigation, population density and water demand, or biodiversity. WOKAM and the subsequent special maps will make it possible to better define, understand and properly manage the world's karst aquifers and their associated natural resources.

Acknowledgements

Chapter 3

Modeling spatially and temporally varied hydraulic behavior of a folded karst system with dominant conduit drainage at catchment scale, Hochifen-Gottesacker, Alps

Abstract

Karst aquifers are important for freshwater supply, but difficult to manage, due to highly variable water levels and spring discharge rates. Conduits are crucial for groundwater flow in karst aquifers, but their location is often unknown, thus limiting the applicability and validity of numerical models. We have applied a conduit model (SWMM) to simulate highly variable flow in a folded alpine karst aquifer system, where the underground drainage pattern is comparatively well known from previous tracer studies. The conduit model was coupled with a reservoir model representing recharge, storage and transfer of water in the epikarst and unsaturated zone. The global optimization approach (GA) was applied to achieve an efficient model calibration. It was possible to simultaneously simulate the highly variable discharge characteristics of an estavelle, and overflow spring and a permanent spring draining the conduit system. The model allowed for the collection of spatially differentiated information on recharge, rapid flow and slow flow in four individual sub-catchments. The formation of backwater upgradient from conduit restrictions turned out to be a key process in activating overflow springs. The proposed modeling approach appears to be transferrable to other karst systems with predominant conduit drainage, but requires previous knowledge of the configuration of the conduit system.

3.1. Introduction

Numerical models are among the most powerful predictive tools for managing groundwater resources in alluvial aquifers, but their application in karst aquifers is more problematic (Scanlon et al., 2003; Worthington, 2009; Worthington et al., 2012) because these aquifers have complex characteristics, which make them very different from porous media (Bakalowicz, 2005; Ford and Williams, 2007). Karst aquifers show strong heterogeneity of water flow and storage, such as autogenic vs. allogenic recharge, diffuse vs. concentrated infiltration, as well as rapid and often turbulent flow in the conduits vs. diffuse flow and storage in the fractured rock matrix (Goldscheider and Drew, 2007; Kiraly, 2002; White, 2003).

Kovacs and Sauter (2007) reviewed various approaches applied for modeling karst aquifers. Lumped parameter or black-box models are often used to simulate the global hydraulic, physical and/or chemical response of a karst spring (output) to recharge events (input) in the spring catchment (Butscher and Huggenberger, 2008; Fleury et al., 2007; Hartmann et al., 2012; Jukić and Denić-Jukić, 2009; Scanlon et al., 2003). Such models help to understand the overall water balance and hydrologic dynamics of the karst system including the variability of water quality (Ghasemizadeh et al., 2012). However, spatial variations of flow patterns in the aquifer cannot be considered in this approach. In contrast, distributed numerical models discretize the model domain into a grid of homogeneous sub-units, for which groundwater flow can be described by flow equations derived from basic physical laws (Sauter et al., 2006). Due to the lack of spatially-distributed information on the hydraulic parameter field in karst systems, particularly concerning the location and geometry of the active conduit network, the application of such models is usually limited to simplified case studies or parameter studies (Birk et al., 2005; Liedl et al., 2003; Reimann, 2009; Reimann et al., 2011; Rooij et al., 2013). Moreover, most distributed models focus on the simulation of groundwater flow, while recharge is calculated independently. Jeannin (2001) applied a discrete conduit network approach to simulate the hydraulics of a variably saturated large cave system. To assess the complex, spatially heterogeneous hydrological process in a large-scale karst catchment, Doummar et al. (2012) and Janža (2010) presented an approach using an integrated catchment model (Mike She), in which lumped and distributed models are coupled. However, Mike She uses Darcy's law and optional conceptual drainage functions to simulate groundwater flow in the saturated zone, while turbulent conduit flow cannot be taken into account.

In this paper, we present an alternative modeling approach to assess hydrodynamic processes in a conduit-flow dominated, shallow karst aquifer system with very well-known drainage structure at a catchment scale, in which the spatial heterogeneity of hydraulic properties and its influence on discharge dynamics can be considered. This approach was tested in a complex alpine karst terrain, which has previously been studied by Goldscheider (2005) and Göppert and Goldscheider (2008). The numerical code Storm

Water Management Model (SWMM, version 5.0.022) by EPA (Rossman, 2010) was used as the basis for this work. As SWMM is originally designed for hydrodynamic modeling of sewer systems and performs very well for the simulation of unsteady and non-uniform flow in conduit systems, Campbell and Sullivan (2002) and Peterson and Wicks (2006) have already used it to study conduit drainage behavior in karst aquifers. SWMM combines lumped models and distributed model and thus has the potential to simulate the spatial heterogeneity of karst aquifer systems at a catchment scale. So far, the application of SWMM, just as with other distributed models, for simulating real karst systems is limited to a few examples (Peterson and Wicks, 2006; Wu et al., 2008), because modeling such system requires detailed information on hydraulic parameter fields, particularly concerning the location and geometry of conduits, which often are not available. To increase the adaptability of SWMM, we have implemented Genetic Algorithms (GA) in our modeling for an improved parameter estimation.

3.2. Study area

The study area is located in the Northern Alps at the border between Germany and Austria (Figure 3.1a). The altitude varies between 1000 m asl (the lowest part of the Schwarzwasser valley) and 2230 m asl (the summit of Mt Hochifen). The northward bordering Gottesacker covers an area of about 10 km^2 and is one of the most spectacular alpine karst landscapes. The total size of the investigated area is 35 km^2.

Geologically, the valley follows the contact between two tectonic units of the Alps (Wagner, 1950). The NW site of the valley belongs to Helvetic Säntis nappe, which consists of folded Cretaceous sedimentary rocks (Figure 3.1b). The Schrattenkalk limestone as the most prominent rock forms a relatively thin karst aquifer (about 100 m) above a thick marl formation acting as a regional aquitard, thus forcing groundwater to flow parallel to the strata, often in turbulent cave streams near the aquifer basis (Goldscheider 2005). The mountain range SE of the Schwarzwasser valley is formed by the sedimentary rocks of the Flysch zone. It is mainly characterized by low to moderate permeability and drains by surface runoff. The karst aquifer in the catchment of the springs is recharged directly from precipitation (diffuse as well as concentrated infiltration) and indirectly from surface streams that drain the part of the catchment area that consists of low permeable Flysch rocks (allogenic recharge). Several quantitative multi-tracer tests with fluorescent dyes and a total of 16 injection points demonstrated that the troughs of plunging synclines form the main underground flow paths (Figure 3.1b), with linear mean flow velocities often exceeding 200 m/h (Goldscheider, 2005). The crests of anticlines act as local groundwater divides in the higher karst zones where the base of the aquifer is above the level of the surrounding valleys. The southeastward adjacent Schwarzwasser valley receives underground inflow from four plunging synclines. Two parallel drainage systems exist in this valley: a surface stream and a continuous underground karst drainage system along the valley axis. An estavelle (QE) at 1120 m asl associated with a cave forms a hydraulic connection between these two flow systems:

during low flows, the surface stream sinks underground into the cave entrance; during high flows, it acts as a karst spring and discharges up to about 4 m³/s. Downstream, in the lower part of the valley, the large but intermediate Aubach spring (QA) at 1080 m asl discharges up to about 8 m³/s but runs dry in long dry periods and in winter. The Bürgermeister (1050 m asl) and Kesselschwand (1040 m asl) springs are permanent but discharge only about 0.04 and 0.015 m³/s respectively. Further downstream, the Sägebach spring (QS) at 1035 m asl presents the largest permanent spring in the valley and discharges up to about 3.5 m³/s.
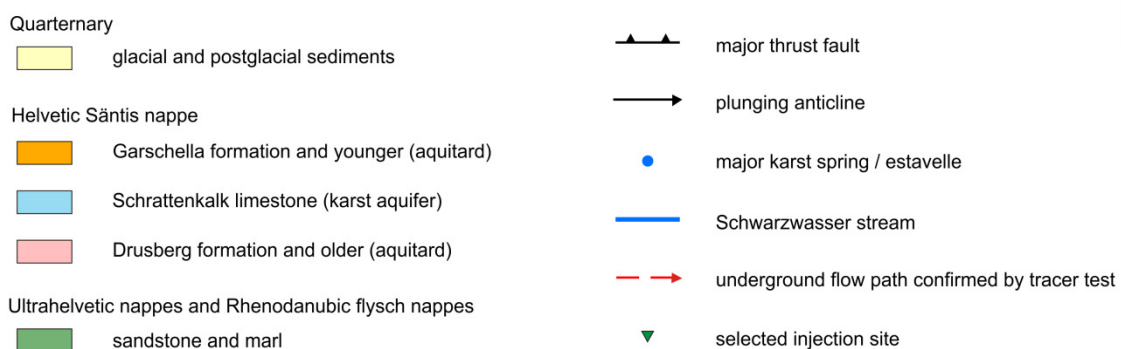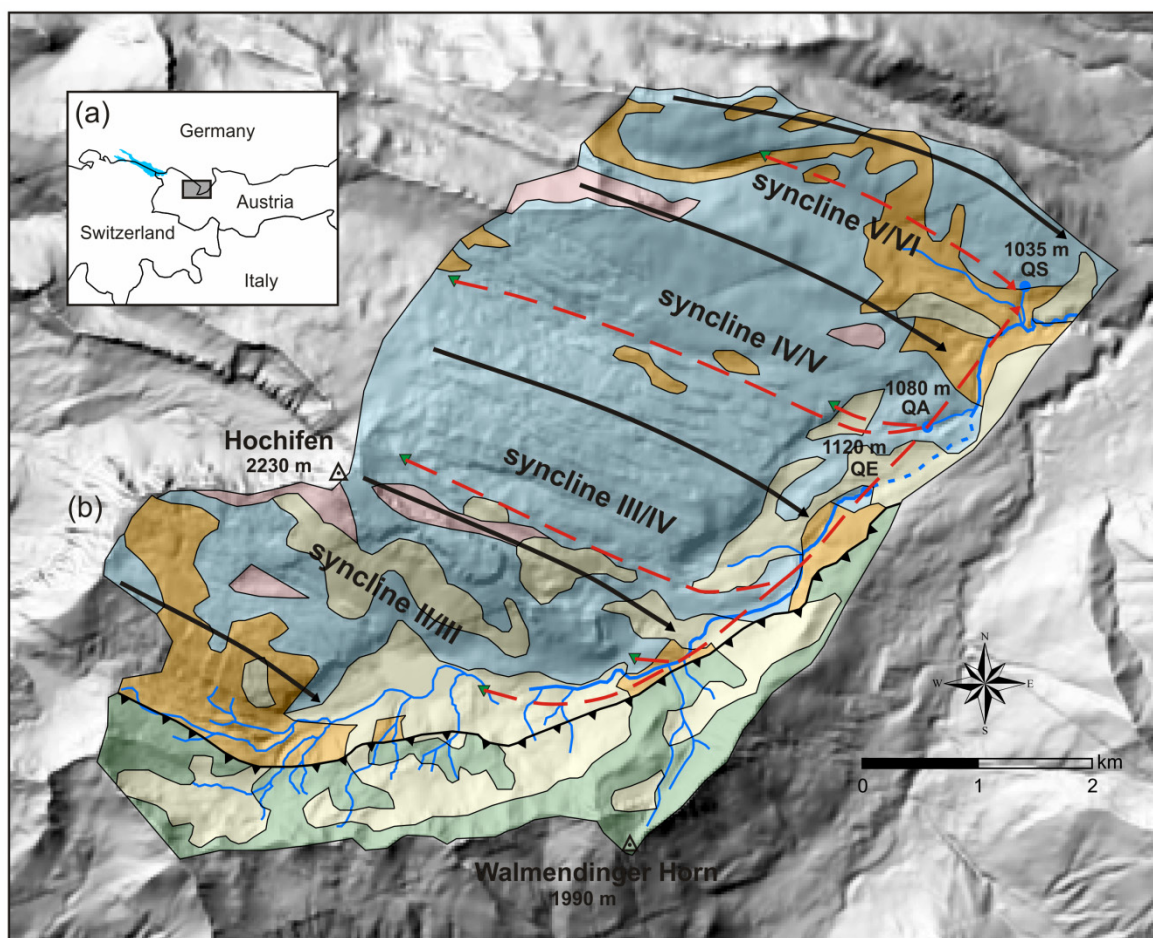
Figure 3.1: a) Location of study area, b) hydrogeological overview of Schwarzwasser stream catchment with the results of tracer tests (modified after Goldscheider (2005)).

The nearest permanent weather station is in the east, bordering Breitach valley at an altitude of 1140 m asl. There, the mean monthly temperature ranges from -2.2 °C in January to 13.6 °C in August, with an annual average of 5.7 °C. The mean annual precipitation is 1836 mm with a major maximum in June – August and a second maximum in December – January. Snow accumulates commonly between November and May.

3.3. Hydrological monitoring

A complete monitoring system was established in the study area, consisting of one meteorological station and four spring monitoring stations. As only one weather station was installed in the study area at 1500 m asl, a uniform time series of hourly meteorological parameters (precipitation, air temperature, relative humidity) was applied in the entire area. System output observations comprise quasi-continuous discharge series with time lags of 15 min observed at the two karst springs (QS, QA) and the estavelle (QE). Two monitoring stations were installed upstream and downstream of QE. The difference between the two values corresponds to allogenic recharge from the Flysch side when the estavelle acts as a swallow hole (negative values) or to discharge from the karst aquifer when it acts as a spring (positive values). Owing to difficult alpine terrain conditions, including massive snow and ice in winter, a complete series of discharge measurement at the estavelle and springs was only obtained for a relatively short period from July to October 2012. However, the investigated karst system is characterized by rapid hydraulic responses to hydrologic events, and the time series selected for model calibration and validation covers a wide range of hydrologic conditions, including several high-flow events and relatively long dry periods. Therefore, the available time series is suitable for model testing but does not allow for the study of long-term trends, seasonal patterns, or system behavior during snowmelt.

3.4. Conceptual model

The presented conceptual model can be divided into three sections: 1) epikarst zone, 2) vadose zone and 3) drainage conduit network. We considered the flow in the unsaturated zone of the karst aquifer as a lumped system that contains the epikarst and vadose zone (Figure 3.2a).

The epikarst contains a store module and a routing module. The store module represents the part of the epikarst that traps the infiltrated water. It is assumed that the store module contributes to the loss of moisture by evapotranspiration. The routing module contributes to the average retention of percolated water and the lateral distribution of recharge between shafts and fractures. The total outflow from shafts (rapid flow) and fractures (slow flow) from the vadose zone represents the main input to the conduit network that transfers water to the karst springs. Based on the previous tracer tests by Goldscheider

(2005), this karst drainage system can be described as a network of comparatively well known, discrete, hierarchically-organized conduits following the axes of plunging synclines and draining sub-catchments limited by anticlines (Figure 3.2b). All conduits from sub-catchments join into one major water collector below the axis of the main valley that is drained by QS (permanent spring), QA (overflow spring) and QE (estavelle) in the lower part of the valley. QE connects this underground master conduit with an allogenic surface drainage system from the adjacent non-karst (Flysch) area. Most of the conduit network is situated above the level of the springs and thus characterized by vadose open-channel flow, but some conduits in the lower part of the valley are situated below the level of the springs and thus permanently saturated (e.g. C14). Pressurized flow in these phreatic conduits is also considered in the model. Conduit-matrix interactions are not considered, although tracer tests during highly transient flow conditions point to possible gradient inversions (Goldscheider 2005). However, because of the mostly vadose conditions and the observed rapid spring recessions (and for reasons of simplicity), such conduit-matrix interactions are not implemented in the model. It is assumed that the system baseflow corresponds to the minimum discharge observed at the lowest spring (QS). This baseflow is introduced into the model by adding a constant flow value to the phreatic conduits in the valley. To reduce model complexity, we simplified our conceptual model as follows: 1) the complicated hydrogeological situation of the rock fall area in the upper Schwarzwasser valley (Sinreich et al., 2002) is not considered, 2) we assume that the estavelle is the only place receiving allogenic recharge.

3.5. Modeling approach

3.5.1. Model input

The hourly precipitation height P (mm/h) is used as a model input parameter. The daily potential evapotranspiration PET (mm/d) is estimated by using the Haude method (DVWK, 1996):

$$\text{PET} = f \cdot (e_{s14} - e_{a14}) \tag{3.1}$$

$$e_{s14} = 6.11 \cdot 10^{(\frac{7.48 \cdot T}{237+T})} \tag{3.2}$$

$$e_{a14} = U \cdot e_{s14} \tag{3.3}$$

where f is the Haude factor for the individual months (f = 0.25 for August, f = 0.23 for September and f = 0.22 for October) and $e_{s14} - e_{a14}$ is water vapor saturation deficit of air (hPa) at 14:00 MEZ, calculated using measured air temperature T (°C) and relative humidity U (%) at 14:00 MEZ.

3.5.2. Epikarst storage

The epikarst storage is constructed to calculate the percolation of water through the top layer of the karst aquifer. The simple approach used by Fleury et al. (2007) was adopted in this work:

$$H_{t1} = H_{t0} + P_{t1} - PET_{t1} - I_{t1} \qquad (3.4)$$

where H is the height of water in the reservoir, P is precipitation, PET is potential evapotranspiration and I is percolated water height through the epikarst reservoir at each time step. All the variables are water heights in mm. $H_{threshold}$ defines the reservoir saturation. Percolation occurs when $H > H_{threshold}$; otherwise, the epikarst reservoir is considered undersaturated and does not deliver water to vadose reservoirs. Therefore, the actual evapotranspiration ET generated by the epikarst storage model can be smaller than PET.

3.5.3. Vadose outflow

Rapid and slow flows in the vadose zone were generated using the non-linear reservoir model in SWMM (Huber and Dickinson, 1992):

$$A_c \cdot \frac{dd}{dt} = Q_{in} - Q_{out} \qquad (3.5)$$

where A_c is correspondent recharge area (m^2), d is water height in reservoir (m), t is simulation time step (s), Q_{in} is inflow (m^3/s) from percolated water from the epikarst, and Q_{out} is generated outflow (m^3/s) from the reservoir, calculated by Manning's equation:

$$Q_{out} = w \cdot \frac{k}{n} \cdot \left(d - d_p\right)^{\frac{5}{3}} \cdot s^{\frac{1}{2}} \qquad (3.6)$$

where w is flow path width (m), k is a conversion factor of 1 (m$^{1/3}$/s), n is Manning's roughness coefficient, d_p is depth of depression storage (m) and s is average conduit slope. Eq. (3.5) and (3.6) are combined into one non-linear differential equation that is solved at each time step by a finite difference scheme. The parameters w, n, d_p and s are used as calibration parameters to adjust vadose flow.

3.5.4. Conduit drainage

The Flow routing module of SWMM solves the conservation of mass and momentum equations that govern the unsteady flow of water through a drainage network of conduits

(Rossman, 2006). These equations, known as the Saint Venant equations, can be expressed in the following form for flow along an individual conduit:

$$\frac{\partial A}{\partial t} + \frac{\partial Q}{\partial x} = 0 \tag{3.7}$$

$$\frac{\partial Q}{\partial t} + \frac{\partial \left(\frac{Q^2}{A}\right)}{\partial x} + g \cdot A \cdot \frac{\partial H}{\partial x} + g \cdot A \cdot S_f + g \cdot A \cdot h_L = 0 \tag{3.8}$$

where x is distance along the conduit (m), A is flow cross-sectional area (m^2), Q is flow rate (m^3/s), H is hydraulic head of water in the conduit (m asl), S_f is the friction slope, h_L is the local energy loss per unit length of conduit and g is the acceleration of gravity (m/s^2). SWMM uses Manning's equation to calculate the friction slope when the conduit is not pressurized, while the Darcy-Weisbach equation will be selected to compute friction loss for conduits with pressurized flow. Eq. (3.7) and (3.8) are solved in the flow routing model by converting them into an explicit set of finite difference formulas that compute the flow in each conduit and head at each junction for each time step.

3.6. Model construction and calibration

3.6.1. Model setup

In our model, only the karst aquifer system and its autogenetic recharge area are spatially represented, (Figure 3.2b), while allogenic recharge from the Flysch side via the estavelle is simulated as a variable boundary condition. The karst area can be subdivided into four sub-catchments (I – IV) corresponding to plunging synclines separated by the crests of anticlines that act as local groundwater divides (Figure 3.1 and 3.2b). To demonstrate possible spatial variability of recharge between different sub-catchments, we used a pragmatic approach considering the limited availability of meteorological data. It is assumed that rainfall in each sub-catchment may differ from the one measured at the meteorological station. Deviations are represented by four variables, $x_1 - x_4$ (Table 3.1). In addition, the spatial variability of evapotranspiration between sub-catchments can be considered by using different threshold values (x5 – x8) of epikarst storage. Due to model structure uncertainty, we assume that each sub-catchment may have varied vadose flow dynamics. Consequently, there are 8 variables ($x_9 - x_{16}$) for the epikarst sub-models and 16 variables ($x_{17} - x_{32}$) for the vadose zone sub-models. To achieve numerical stability, each sub-catchment is discretized into 5 elements with different sizes (Table 3.2). The karst drainage network consists of 16 conduits, 14 junctions and 3 system outlets (the two springs and the estavelle). The overall configuration of the drainage conduit network is known from tracer experiments by Goldscheider (2005) and Göppert and Goldscheider (2008). As the precise geometry of the karst conduits is unknown, the drainage network is represented in a simplified way by a set of 16 conduit elements, where each individual element has a constant cross section and a circular shape. Peterson and Wicks (2006)

have studied the importance of conduit geometry parameters in karst systems using SWMM, and their work serves as a basis for our parameterization. Altogether, 46 variables ($x_{33} - x_{78}$) are required to describe the conduit network geometry: 16 for the diameter of the individual conduit elements, 16 for roughness, and 14 for junction elevations that determine the inclination (bottom slope) of the conduits (Table 3.1).
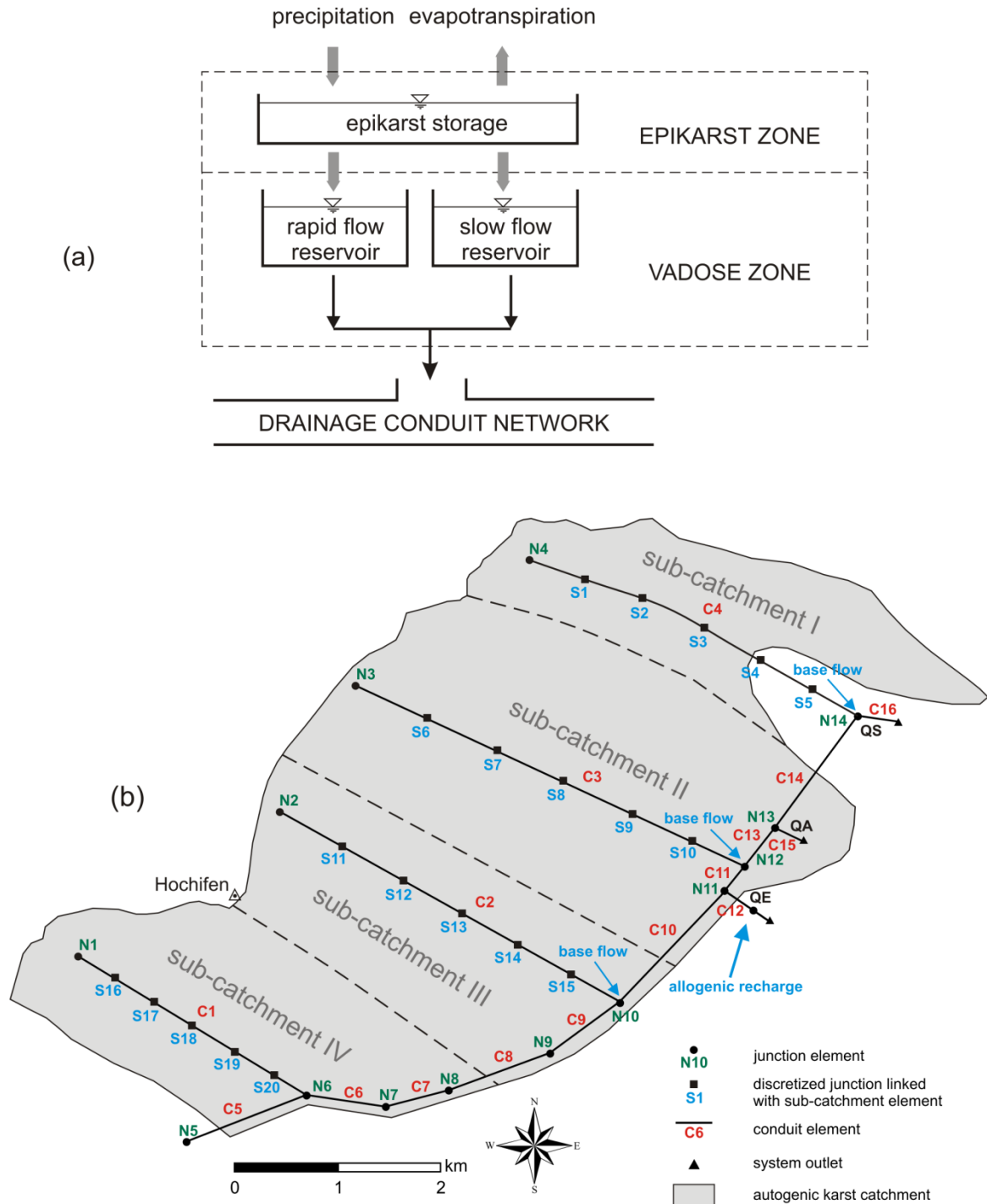
Figure 3.2: a) Structure of the conceptual model that describes hydrological processes in the unsaturated zone and b) configuration of the karst conduit drainage network in the SWMM model.

Table 3.1: Information on model parameters determined in the optimization procedure.

model part	model parameter	correspondent model location	description	unit	optimized value
input	x1	sub-catchment I	proportional deviation from unique measured rainfall	%	-43
	x2	sub-catchment II			-11
	x3	sub-catchment III			-4
	x4	sub-catchment IV			-48
epikarst zone	x5	sub-catchment I	infiltration threshold	mm	10
	x6	sub-catchment II			19
	x7	sub-catchment III			5
	x8	sub-catchment IV			29
	x9	sub-catchment I	proportion of recharge distributed into rapid flow reservoir	%	60
	x10	sub-catchment II			75
	x11	sub-catchment III			35
	x12	sub-catchment IV			75
	x13	sub-catchment I	average response delay	h	1
	x14	sub-catchment II			0
	x15	sub-catchment III			1
	x16	sub-catchment IV			2
vadose zone	x17	sub-catchment I	width of flow path for rapid flow reservoir	m	171
	x18	sub-catchment II			141
	x19	sub-catchment III			160
	x20	sub-catchment IV			128
	x21	sub-catchment I	width of flow path for slow flow reservoir	m	39
	x22	sub-catchment II			36
	x23	sub-catchment III			53
	x24	sub-catchment IV			23
	x25	sub-catchment I	Manning's roughness coeff. for rapid flow reservoir	-	0.010
	x26	sub-catchment II			0.012
	x27	sub-catchment III			0.015
	x28	sub-catchment IV			0.019
	x29	sub-catchment I	Manning's roughness coeff. for slow flow reservoir	-	0.160
	x30	sub-catchment II			0.167
	x31	sub-catchment III			0.143
	x32	sub-catchment IV			0.124
drainage conduit network	x33	N1	junction elevation	m asl	1839
	x34	N2			1834
	x35	N3			1662
	x36	N4			1626
	x37	N5			1441
	x38	N6			1302
	x39	N7			1283
drainage conduit network	x40	N8	junction elevation	m asl	1289
	x41	N9			1246
	x42	N10			1218
	x43	N11			1129
	x44	N12			1112
	x45	N13			1098
	x46	N14			1025
	x47	C1	conduit diameter	m	3.5
	x48	C2			2.3
	x49	C3			2.5
	x50	C4			2.1
	x51	C5			2.9
	x52	C6			3.6
	x53	C7			2.8
	x54	C8			3.1
	x55	C9			2.9
	x56	C10			3.2
	x57	C11			0.8
	x58	C12			3.4
	x59	C13			3.2
	x60	C14			0.7
	x61	C15			3.5
	x62	C16			3.8
	x63	C1	conduit roughness	mm	760
	x64	C2			678
	x65	C3			1802
	x66	C4			1209
	x67	C5			589
	x68	C6			861
	x69	C7			777
	x70	C8			139
	x71	C9			1666
	x72	C10			1965
	x73	C11			1258
	x74	C12			852
	x75	C13			110
	x76	C14			1377
	x77	C15			786
	x78	C16			1035

sub-catchment index	sub-catchment element index	recharge area, km²
sub-catchment I	S1	0.43
	S2	0.89
	S3	0.80
	S4	0.90
	S5	1.34
sub-catchment II	S6	1.37
	S7	1.57
	S8	1.67
	S9	1.77
	S10	2.73
sub-catchment III	S11	0.97
	S12	0.94
	S13	0.99
	S14	1.03
	S15	1.33
sub-catchment IV	S16	1.04
	S17	0.94
	S18	0.92
	S19	0.90
	S20	1.48

Table 3.2: Recharge areas of the individual sub-catchment elements.

3.6.2. Performance criteria

Model performance was measured using three different criteria: Root Mean Square Error (RMSE; Eq. 3.9), measure of deviation between the observed and simulated discharges; Nash-Sutcliffe Coefficient (NSC; Eq. 3.10), measure of the overall agreement of the shape of the hydrograph; Volume Error (Error$_v$; Eq. 3.11), agreement between the observed and simulated discharged total flow volumes.

$$\text{RMSE} = \sqrt{\frac{1}{N}\sum_{i=1}^{N}(Q_{o.i} - Q_{s.i})^2} \tag{3.9}$$

$$\text{NSC} = 1 - \frac{\sum_{i=1}^{N}(Q_{o.i} - Q_{s.i})^2}{\sum_{i=1}^{N}(Q_{o.i} - Q_o)^2} \tag{3.10}$$

$$\text{Error}_v = 100 \cdot \left(\frac{\sum_{i=1}^{N} Q_{s.i} - \sum_{i=1}^{N} Q_{o.i}}{\sum_{i=1}^{N} Q_{o.i}}\right) \tag{3.11}$$

where $Q_{s,i}$ is the simulated discharge at time i, $Q_{o,i}$ the observed discharge at time i, Q_o is the average observed discharge and N is the number of measurements in the test period.

3.6.3. Calibration procedure

As it is almost impossible to estimate 78 parameters manually, we adopted the global optimization approach GA (Goldberg, 1988) using the Matlab 7.0 GA Toolbox. GA has been applied for calibration of rainfall-runoff-models (Fazal et al., 2005), distributed groundwater flow models (Lakshmi Prasad and Rastogi, 2001), pipe networks (Dandy et al., 1996) and distributed catchment models (Fang and Ball, 2007; Liong et al., 1995). In this study, GA was used to estimate the deviated precipitations in the sub-catchments, the configuration of sub-models for the epikarst and vadose zone, as well as the geometry of the drainage conduit network. The objective function used in GA is the sum of the RMSE values of all three model outputs: $RMSE_{objective} = RMSE_{QE} + RMSE_{QA} + RMSE_{QS}$. Additionally, to optimize the conduit network storage efficiently, a time of low-flow conditions (22 Aug 2012) was defined as initial state for the simulation. A representative model parameter set must be able to simulate the hydrologic states of the three system outlets under these low-flow conditions (QE acts as swallow hole, QA is dry, and QS has minimal discharge). The proposed computational procedure of optimization using GA for the SWMM model is presented in Figure 3.3.
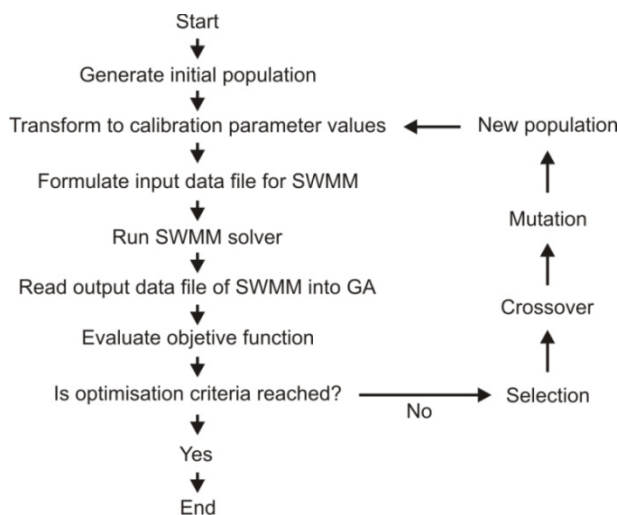
Figure 3.3: Implemented optimization procedure using GA.

3.7. Results and discussion

3.7.1. General model performance

The model is able to simultaneously simulate the transient and highly variable hydraulic behavior of all three outlets of the karst system: the estavelle (QE) alternately operates as a spring and as a swallow hole, QA acts as an intermittent overflow spring, while QS is permanent, although with marked discharge variations (Figure 3.4).

Moreover, the shapes of the spring hydrographs, total flow volumes, peak flows and subsequent recession periods are well reproduced. The quality of the model simulation

using the final parameter set is demonstrated by all three criteria, RMSE, NSC and Error$_v$. The result is very satisfactory: RMSE values are 0.120 for QE, 0.320 for QA and 0.073 for QS. NSC values are 0.946 for QE, 0.916 for QA and 0.927 for QS. Also the simulated flow volumes are very close to observed flows: Error$_v$ values are 4 % for QE, 4 % for QA and -2 % for QS.
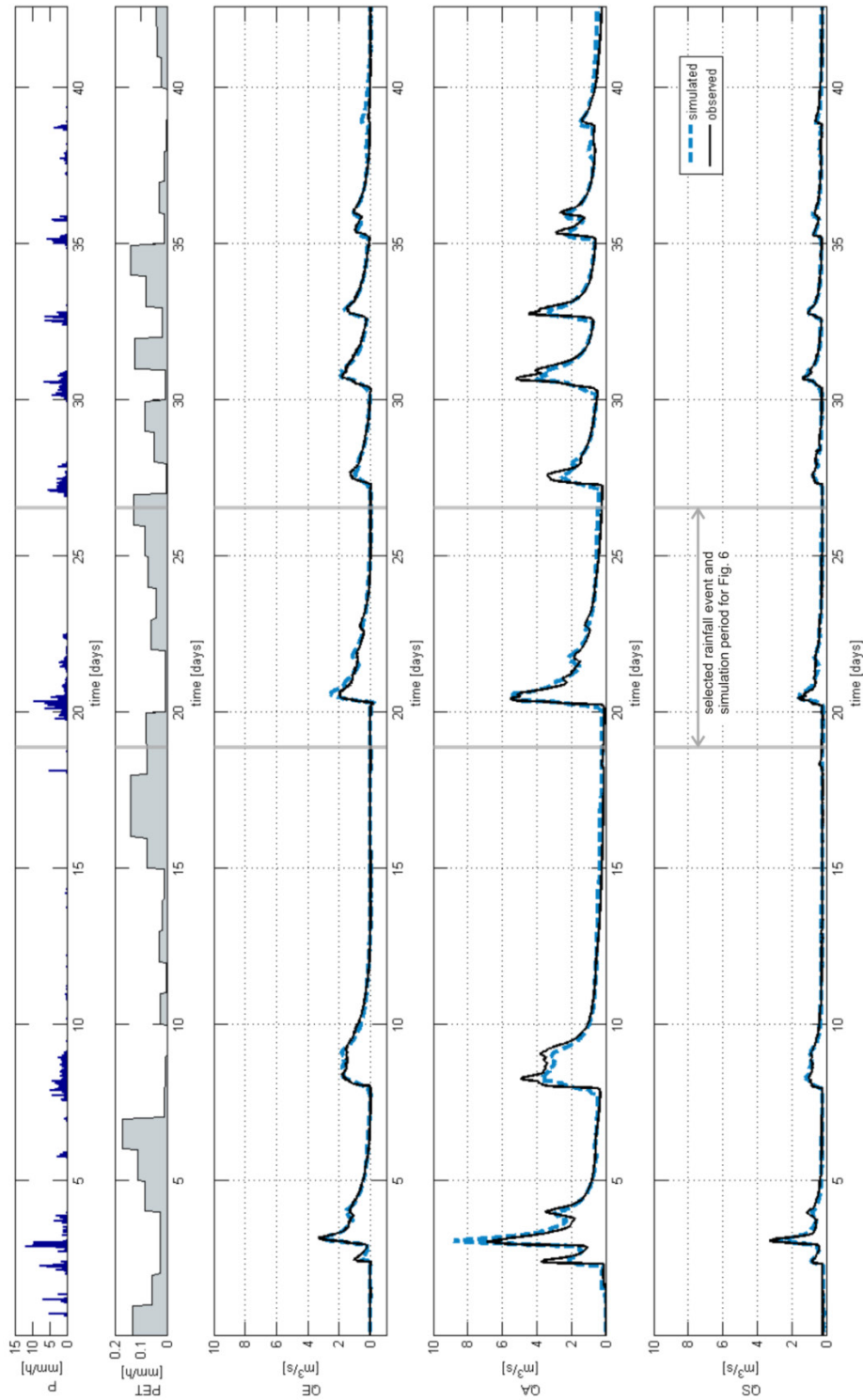
Figure 3.4: Observed and simulated discharges of springs QS, QA and QE using the optimized representative parameter set for the period 22 Aug – 04 Oct 2012.

3.7.2. Groundwater recharge and vadose flow

In the simulation period, precipitations estimated by model calibration are lower than the rainfall measured at the only available weather station (443 mm): 250 mm (-43 %) for sub-catchment I, 395 mm (-11 %) for sub-catchment II, 425 mm (-4 %) for sub-catchment III and 229 mm (-48 %) for sub-catchment IV. This general negative derivation could be explained by the position of the weather station above the tree line, whereas interception losses in the wide forested areas further below reduce effective precipitation heights. Calculated evapotranspiration plus epikarst storage are 64 mm for sub-catchment I, 73 mm for sub-catchment II, 53 mm for sub-catchment III and 82 mm for sub-catchment IV. These variations result in spatially varied groundwater recharge: 186 mm for sub-catchment I, 321 mm for sub-catchment II, 373 mm for sub-catchment III and 147 mm for sub-catchment IV.

Due to the lack of spatially distributed information on meteorological parameters, the estimation of spatially distributed groundwater recharge leads to unavoidable uncertainties. However, with these spatially adapted recharge values, the model performed very well and highly consistent under the strongly varied hydrological conditions during the entire test period. This suggests that the recharge estimations are reliable. Furthermore, the heterogeneous pattern of recharge estimated by the model calibration is consistent with field observations, such as distribution of soil, vegetation and bare karst limestone outcrops.

The distribution of recharge water into the different reservoirs, calculated by the epikarst routing module, also presents a spatially heterogeneous pattern. In general, recharge contributes predominantly to the rapid flow reservoir: 60 % in sub-catchment I, 75 % in sub-catchment II, 35 % in sub-catchment III and 75 % in sub-catchment IV.

Figure 3.5 shows that the simulated vadose outflow dynamics varies from sub-catchment to sub-catchment due to spatially heterogeneous estimated groundwater recharge and different hydraulic properties of the respective vadose reservoirs. The duality of flow dynamic in the vadose zone is well demonstrated in the simulation. In general, rapid flow components dominate in vadose zone flow, mainly during peak flow and short-term recession, whereas the subsequent relatively gentle recession is mainly formed by slow flow components. However, while the overall model performance can be validated by observed discharge series from three outlets of the conduit system (QE, QA, QS), a direct and specific validation of the simulated vadose flows is not possible. Therefore, the simulation results are associated with inherent uncertainties, but they are plausible and consistent with field observations in the test site, e.g. with the general flow dynamics observed in cave streams (Höhlenverein Sonthofen, 2006).
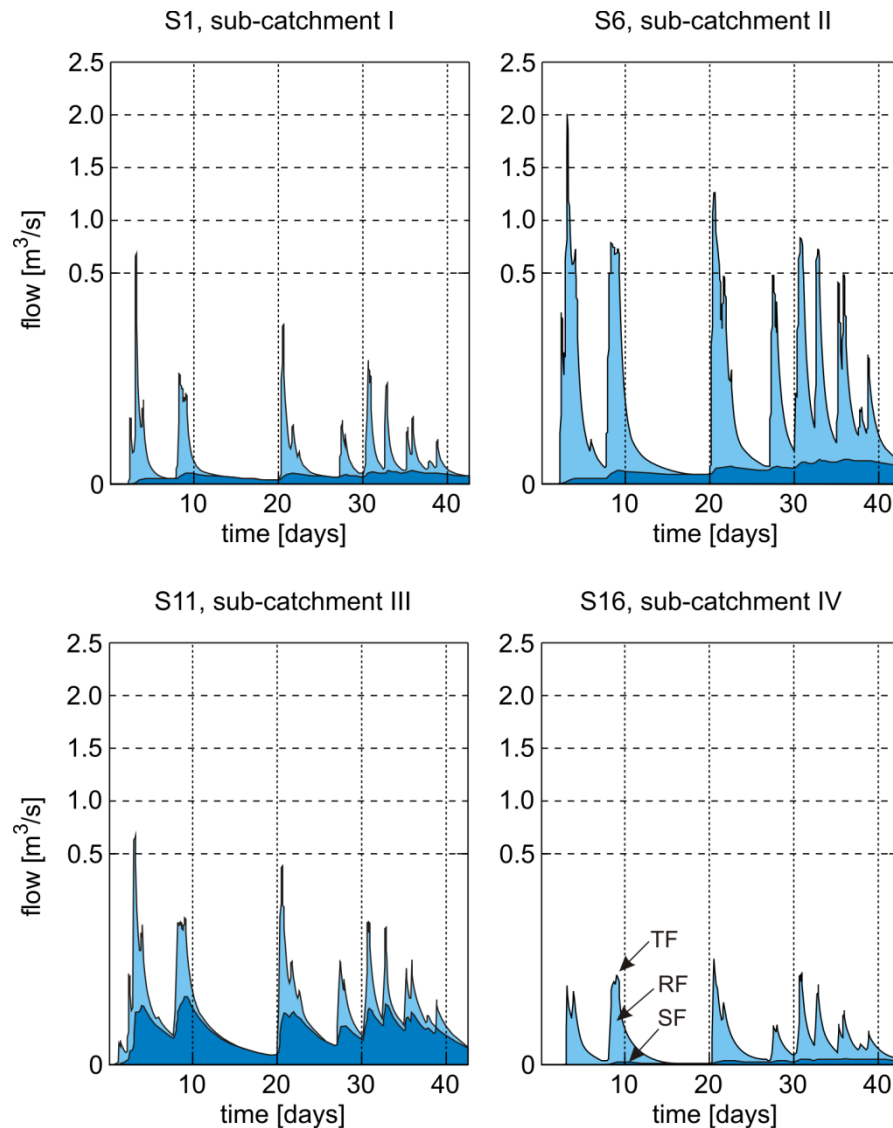
Figure 3.5: Simulated vadose outflows of sub-catchment element S1, S6, S11 and S16 for the period in 22 Aug – 04 Oct 2012. The flow components are presented as rapid flow (RF), slow flow (SF) and total flow (TF).

3.7.3. Discharge pattern in conduit network

Figure 3.6 presents six characteristic stages of a complete hydraulic response of the drainage conduit network to an intense rainfall event. Initially (stage I), the estavelle (QE) is dry and the discharge at QA and QS is low, 0.18 and 0.20 m^3/s, respectively. During the event, the estavelle first acts as a swallow hole (stage I) and then into a spring (III-V), while discharge at QA and QS increases up to 5.63 and 1.55 m^3/s (III), followed by a recession period during which the estavelle runs dry again (VI). This cycle corresponds to the observed dynamics of the estavelle and the two springs (Goldscheider 2005), but the model delivers additional and new insights into the flow and hydraulic pressure dynamics inside the inaccessible conduit network.
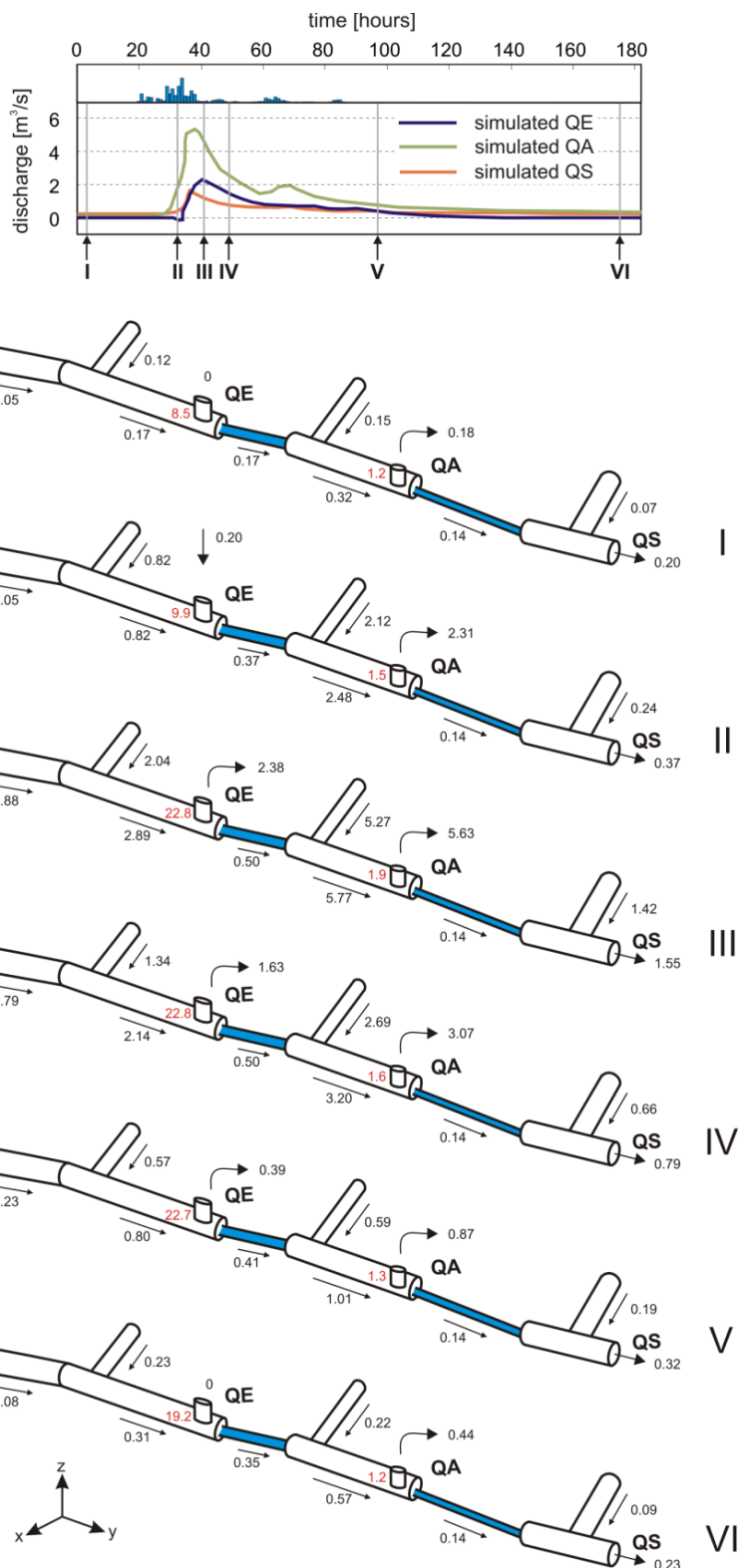
Figure 3.6: a) Simulated hydrographs of QE, QA and QS during a high-flow event, with indication of time steps I to VI presented in the six sketches below. b) Flow rates in the conduit network during this high-flow event. Blue conduits present pressurized parts of the network, red numbers indicate hydraulic head (m) over the end of the respective conduit element, and black numbers represent simulated discharge (m³/s) in the conduit element or at the springs. Note that the highly dynamic behavior of the estavelle is correctly simulated: it is dry in time step I, acts as a swallow hole in II, transforms into a spring in III to V and runs dry in VI.

The geometry (diameter, length, slope) of the conduit network in Figure 3.6 is presented proportionally. Conduits C11 and C14 represent hydraulic restrictions, owing to their smaller diameters (0.8 m and 0.7 m) and higher roughness (1258 mm and 1377 mm). The conduit restrictions down gradient from QE (C11) and QA (C14) are already fully saturated (phreatic conduits with pressurized flow) before the rainfall event, but show different dynamics during the event: the flow in conduit restriction C11 increases further when the water level (hydraulic head) in the estavelle increases, associated with increasing spring discharge. In contrast, flow in C14 remains nearly constant (0.14 m³/s) during the complete rainfall event, probably because of the permanently saturated and artesian confined conditions in this lowermost part of the conduit network. Furthermore, the overflow spring QA at the upper end of this conduit limits the hydraulic head variations. Observed discharge variations at QS (located at the downstream end of C14) are thus mainly caused by variable inflow from sub-catchment I (syncline V/VI in Figure 3.1), which is consistent with observations from tracer tests (Goldscheider 2005, Göppert and Goldscheider 2008). The proposed conduit restrictions occur down gradient from QE and QA, in zones where the aquifer is confined by low-permeability formations. At these places, increased flow can cause backwater and thus activate the overflow spring (QA) and the estavelle (QE). Although the three system outlets (QE, QA, QS) are connected by a series of conduits along the valley axis (Figure 3.1b and 3.2b), the model simulations demonstrated that the discharge dynamics of the individual springs are mainly driven by the recharge and flow dynamics of the corresponding sub-catchments. This finding can be explained by landscape evolution and speleogenesis: the drainage systems of the individual sub-catchments (synclines divided by anticlines) could have developed separately, probably since the Pliocene, when the Schrattenkalk limestone of the Hochifen-Gottesacker area had been exposed by erosion of overlying formations (Wagner 1950). The connecting conduits below the valley axis had surely developed later, probably after the last glaciation that had shaped the Schwarzwasser valley in its present form.

3.7.4. Discussion of model limitations

In general, the model is able to simulate the hydraulic behavior and hydrologic variability of this karst system for the entire simulation period. Excellent fits between observed and simulated discharge were achieved for QE and QS; the hydrograph of QA was also generally well reproduced. However, the model did not very accurately simulate the discharge behavior of QA in response to heavy rain events following relatively long dry periods. This could be due to intermediate storage of water in the epikarst or vadose zone in sub-catchment II or due to a more complex structure of the hydrogeology than the one represented in the conceptual model.

Due to the lack of reliable data concerning snow accumulation and snow melt, the current model was calibrated for a summer to autumn period without snow and can only be used for such periods. Better spatiotemporal, meteorological and snow input data would

significantly extend the applicability of our model. As the model does not consider conduit-matrix interactions, it will not be able to simulate hydraulic processes or transport phenomena related to such gradient inversions. Furthermore, as the baseflow is currently introduced as a constant value (corresponding to the minimum discharge of the lowest drainage point, QS), the model is not able to predict system behavior during extremely long dry periods related to climate change.

3.7.5. Model optimization

During the optimization procedure, 24000 model runs were evaluated, whereas the best representative parameter set reached a fitness of 0.513. Figure 3.7 shows the evolution of average and best fitness during model optimization. The two curves converge and reach stable levels after about 30 generation steps. Figure 3.8 presents the evolution of individual model performance for the three system outlets ($RMSE_{QE}$, $RMSE_{QA}$, $RMSE_{QS}$) during the optimization procedure versus the global model performance, expressed as $RMSE_{objective}$. It can be observed that both the individual and the global model performance improve significantly during the process. The performance of the model optimization strongly depends on the initial parameter ranges, which are estimated based on earlier studies (Goldscheider 2005, Göppert and Goldscheider 2008) and our improved system understanding, achieved during the monitoring period.
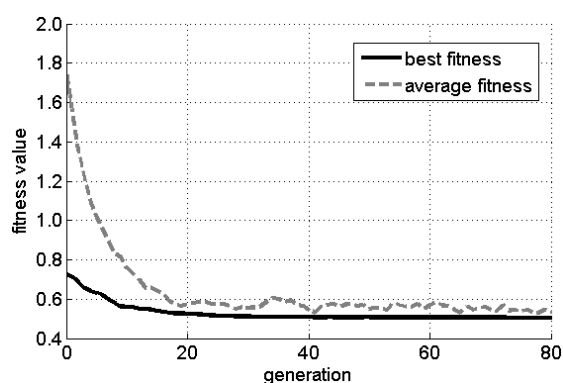
Figure 3.7: Evolution of average and best-fit values during the model optimization.
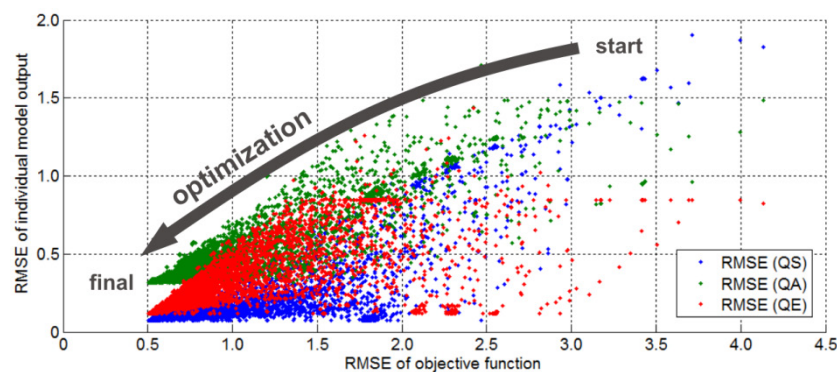
Figure 3.8: Scatterplot of RMSE values for the individual springs ($RMSE_{QE}$, $RMSE_{QA}$ and $RMSE_{QS}$) versus RMSE value of the objective function ($RMSE_{objective}$) at each model evaluation during the optimization procedure.

3.8. Conclusions

In this work, we presented a concept-based modeling approach to assess hydrodynamic processes in shallow karst aquifer systems with dominant conduit drainage at catchment scale. The approach was tested in a complex alpine karst terrain, whose drainage pattern was previously very well known through tracer experiments, geological mapping and cave observation. Results of the tested modeling approach showed its general ability of modeling spatially heterogeneous hydrological processes in complex karst terrains under varied hydrological condition. The presented model structure enables incorporation of the main hydrological processes and hydrogeological elements of the studied karst aquifer (epikarst, vadose zone, conduit network). The hydrographs of three system outlets (a permanent spring, an overflow spring and an estavelle) were simulated simultaneously. The obtained results are very satisfactory. The model performed consistently under strongly varied flow conditions. Moreover, the model is able to simulate transient hydrodynamic behavior of phreatic and epiphreatic conduits and to reproduce the hydraulic behavior of a permanent spring, an overflow spring and an estavelle under varied hydrological conditions. Simulated vadose outflows show strong temporal variations and spatial differences between the individual sub-catchments. The processes in our hydrogeological conceptual model, which determine rainfall-runoff-dynamics in this karst aquifer, can be demonstrated in the simulation: duality of flow dynamics in the vadose zone (rapid flow vs. slow flow), and the formation of backwater due to hydraulic restrictions in the conduit system down gradient from the estavelle and overflow spring.

Due to incomplete measurement data concerning the spatiotemporal distribution of recharge, the model has some limitations. However, this study represents an access to complex hydrodynamic processes in a shallow karst aquifer with dominant conduit network drainage at a catchment scale and serves to better understand spatial heterogeneity of aquifer hydraulic properties and its influence on discharge dynamics based on available measurement data.

For the use in applied water management, this modeling approach could be transferred to other karst systems with similar characteristics, i.e. unconfined, shallow karst aquifers that are predominantly drained by conduits. Good knowledge about the conduit system from tracer tests and/or speleological investigations (Goldscheider et al., 2008) is required to establish a proper conceptual model. The most significant strength of this modeling approach for water management is its capability to simulate temporally and spatially varied hydrodynamic behavior in complex karst conduit networks with simultaneous consideration of storage and flow in the unsaturated zone. In terms of modeling technique, the global optimization approach GA was successfully implemented. With this approach, the modeling limitations caused by input and parameter uncertainty can be overcome and the applicability of SWMM for karst aquifer modeling can be facilitated.

Measurements of hydrological and meteorological data in remote and alpine terrain are always associated with difficulties and uncertainties, mainly during extreme events. Therefore, it would be sensible to perform an uncertainty analysis to define behavioral parameter ranges with consideration of uncertainty from different sources. Due to the high dimension of the parameter set and model complexity, a sensitivity study could help to better characterize key processes and parameters in the model, and to facilitate its further application, extension and transfer to other karst aquifer systems.

Acknowledgements

Chapter 4

A new approach to evaluate spatiotemporal dynamics of controlling parameters in distributed environmental models

Abstract

Distributed environmental models are usually high-dimensional and non-linear. To comprehensively evaluate the spatiotemporal dynamics of model controls, we propose a novel multi-step approach based on Sobol's method to evaluate parameter sensitivity as well as interactions with respect to different model outlet points, using different objective functions to assess different hydrodynamic conditions; all varying through time. This complete sensitivity analysis can be performed for prior and posterior parameter ranges. The difference between them can be used to assess the influence of parameter constraints on the results of sensitivity analyses. We applied this holistic approach to an existing distributed karst watershed model. The results demonstrated that 1) a limited number of spatially-distributed parameters control the varying flow pattern, 2) the model is nonlinear and the influential parameters are highly correlated in the model domain and 3) the spatial patterns of identified parameter sensitivity and interactions are strongly influenced by given parameter bounds.

4.1. Introduction

Distributed modelling is widely applied to simulate broad classes of pathways for water movement through space, e.g., overland flow, unsaturated flow in the vadose zone, and saturated groundwater flow (Kampf and Burges, 2007). In recent years, these distributed hydrological models have become very popular in many applications, such as advancing scientific understanding of underlying hydrological processes at the surface (Lehning et al., 2006) and in the subsurface (Worthington, 2009); analyzing the potential impacts of land use (Andrew and Dymond, 2007) and climate change (Krysanova et al., 2007); and developing water quantity and quality management options for informed decision making (Ahrends et al., 2008; Peña-Haro et al., 2011).

Sensitivity analysis (SA) methods are often used for developing and evaluating complex distributed hydrological models (Christiaens and Feyen, 2002; Gamerith et al., 2013; Herman et al., 2013; Hill and Tiedeman, 2007; Nossent et al., 2011; Pappenberger et al., 2008; Sieber and Uhlenbrook, 2005; Tang et al., 2007a; van Werkhoven et al., 2008). Generally, SA is used to assess the contribution of individual inputs or groups of inputs on model outputs and to identify key inputs that control model outputs (Razavi and Gupta, 2015). Mostly, SA is assessed with respect to signatures or error metrics that are applied to model outputs. Performing a SA in model space domain may enhance understanding of the model response to not only variation in model inputs, but also their spatial distribution (Fisher et al., 1997; McIntyre et al., 2005; Moreau et al., 2013). Consequently, according to Wagener et al. (2009a), the SA results can be used to: 1) select input parameters to include in a calibration procedure or enable a more focused planning of future research and field measurement, 2) evaluate the realism of parameter values and boundary conditions, 3) prove that the model is sufficiently sensitive to represent the behavior of a natural system, and 4) reduce a model to its essential structures.

SA can be categorized into local and global methods (Saltelli et al., 2000). Compared to local methods, global methods vary all parameters simultaneously within predefined regions to quantify their importance and possible interactions (Saltelli, 2004). A global sensitivity analysis method that is very popular in many fields is the variance-based Sobol's method (Sobol', 1990). In general, variance-based sensitivity analysis methods aim to quantify variance in model output based on variance in model inputs and their interactions with one another. For Sobol's method, these responses, caused either by a single parameter or by the interaction of two or more parameters, are expressed as sensitivity indices. These indices represent fractions of the unconditional model output variance. In recent years, this powerful SA technique has been increasingly applied to complex distributed models, because of its ability to incorporate parameter interactions and its relatively straightforward interpretation (Hall et al., 2005; Nossent et al., 2011; Pappenberger et al., 2008; Song et al., 2012; Tang et al., 2007a; van Werkhoven et al., 2008; Wagener et al., 2009b; Zhang et al., 2013). A powerful extension of the conventional application of Sobol's method is to evaluate event-scale spatial sensitivities

(Tang et al., 2007a; van Werkhoven et al., 2008). Wagener et al. (2009b) demonstrated that the results strongly depend on the chosen objective function (i.e. considered system state) and suggested using a multi-objective approach to explore spatial parameter controls limited by event-scale. Focusing on the event-scale independence, dynamic controls of distributed models have been explored at a predefined time step throughout the model simulation by using the Method of Morris (Herman et al., 2013) and the Fourier amplitude sensitivity test (Reusser et al., 2011).

However, in past studies (e.g. Nossent et al., 2011; Sieber and Uhlenbrook, 2005; Song et al., 2012; Zhang et al., 2013), the distributed parameter field was mostly assumed to be spatially-homogenous. Only a few studies (Herman et al., 2013; Tang et al., 2007a; van Werkhoven et al., 2008) have investigated the sensitivity of model behavior to heterogeneous spatially-distributed parameters. Furthermore, the effects of spatially-distributed parameters are only assessed by analyzing the variance of non-spatially-distributed model output. To fill this knowledge gap, the present work will focus on characterizing uncertainty for spatially-heterogeneous distributed parameters, and their apportionment on spatially-distributed model outputs. Additionally, the issue of parameter constraints and their influence on the results of sensitivity analyses is generally not considered in any detail. The final aim of the present work is to develop a balanced approach based on Sobol's method for 1) spatial and temporal sensitivity analysis which is suitable for non-stationary, spatially-distributed models with high complexity, high parameter interactions, and high non-linearity, 2) identifying the spatiotemporal processes controlling model behavior, 3) comprehensive evaluation of parameter realism across model time and space domains and 4) assessing the impact of parameter constraints on previous sensitivity analysis results.

We applied our method to the existing distributed karst watershed model by Chen and Goldscheider (2014). In general, karst aquifers are highly sensitive to environmental changes and more vulnerable to contamination than other aquifer types due to their specific hydraulic properties (Goldscheider and Drew, 2007). The model case study focused on a complex karstified alpine carbonate aquifer system in the Schwarzwasser Valley (Austria/Germany), where the aquifer drainage dynamics are characterized by extreme hydraulic spatial heterogeneity (Goldscheider, 2005). Our new method is used to evaluate the spatiotemporal dynamics of model controls in the watershed model.

4.2. Study area

The Hochifen-Gottesacker karst system is located in the Northern Alps on the Germany/Austria border (Figure 4.1a). It has an area of about 35 km^2, and an altitude varying between 1000 m asl (the lowest part of the Schwarzwasser valley) and 2230 m asl (the summit of Mt. Hochifen). It should be noted that in this study, we consider summer periods when snow processes are not important. A hydrogeological conceptual model was developed through geological mapping and several quantitative multi-tracer tests

(Goldscheider, 2005; Göppert and Goldscheider, 2008). In the study area, the Schrattenkalk limestone with a thickness of about 100 m acts as the main karst aquifer, and is underlain by marl formations. Flow paths in the karst aquifer are controlled by geologic structures and generally follow plunging synclines. Hydrologically, the karst aquifer is directly recharged (autogenically) from precipitation and indirectly (allogenically) from surface streams, which drain the part of the catchment area that consists of low permeability Flysch rocks. The tracer tests confirmed that two parallel drainage systems exist in this valley: a surface stream and a continuous underground karst drainage system along the valley axis (Goldscheider, 2005). The karst aquifer is mainly drained by three outlets: 1) an estavelle (QE) at 1120 m asl associated with a cave forms a reversible hydraulic connection between the two drainage systems and discharges up to about 4 m^3/s, 2) a large but intermittent and intermediate overflow spring (QA) at 1080 m asl discharges up to about 8 m^3/s but is inactive in extended dry periods and in winter and 3) a permanent spring (QS) at 1035 m asl in the valley that discharges between 0.16 and about 3.5 m^3/s.

4.3. Methodology

Three basic research questions guided us to design this holistic approach to evaluating spatiotemporal dynamics of controlling parameters in distributed environmental models:

1. What are the sensitive model parameters in space and time across the model domain? We evaluated parameter sensitivity using Sobol's method with respect to different model outlet points, using different objective functions to assess different hydrodynamic conditions as a function of time.

2. How do parameter interactions influence the model behavior? We quantified interactions between model parameters using Sobol's method in model space and time domains, in order to better understand model complexity and model internal process dynamics.

3. How are our results influenced by the choice of parameter ranges? We used the DREAM algorithm to constrain the model and to explore posterior parameter bounds derived from the posterior distributions. The complete sensitivity analysis was performed for both initial (prior) and posterior parameter ranges. So we could assess differences between the parameter sensitivity based on prior and posterior information, and assess the influence of parameter constraints on previous sensitivity analysis results.

4.3.1. Model setup

For the present work, we used a slightly modified version of the existing distributed watershed model by Chen and Goldscheider (2014), which is mainly based on the distributed hydrology-hydraulic water quality simulation model – Storm Water Management Model (SWMM, version 5.0) developed by the EPA (Rossman, 2010). In our model, recharge, storage and drainage of water in the karst catchment are represented by a concept-based reservoir module, which is directly coupled to a downstream conduit drainage module simulating highly variable flow in the underground karst drainage system along the valley axis (Figure 4.1b and 4.1c). The karst catchment is divided into four sub-catchments (I – IV) corresponding to local tectonic structures. The recharge for individual sub-catchments is calculated separately using interpolated meteorological input data over the study area, while allogenic recharge from the Flysch site via the estavelle is simulated as a variable boundary condition. Hence, using spatial attribution by sub-catchments to calculate recharge, plus a fully-distributed hydraulic model to simulate conduit dynamics, our model is very similar to true fully-distributed models. In total, 54 model parameters were considered for the testing: model parameters $x_1 - x_{20}$ define the main hydrological processes of the epikarst and vadose zone in the individual sub-catchments, while parameters $x_{21} - x_{54}$ describe the geometry and hydraulic properties of the drainage conduit network in the valley (Table 4.1).

The model was evaluated for the period from 22 August to 04 October 2012 on an hourly time step. We interpolated the data (hourly precipitation, air temperature and relative humidity) from seven meteorological stations around the studied catchment with 1km × 1km grid resolution over the investigated area using a combined inverse distance weighting and linear regression gridding. Mean areal precipitation and potential evapotranspiration for individual sub-catchments are determined based on the interpolated meteorological data field, in which hourly potential evapotranspiration is estimated using a modified Turc-Ivanov approach after Wendling and Müller (1984). For model evaluation, hourly measured discharges at the two karst springs (QS, QA) and the estavelle (QE) are applied.
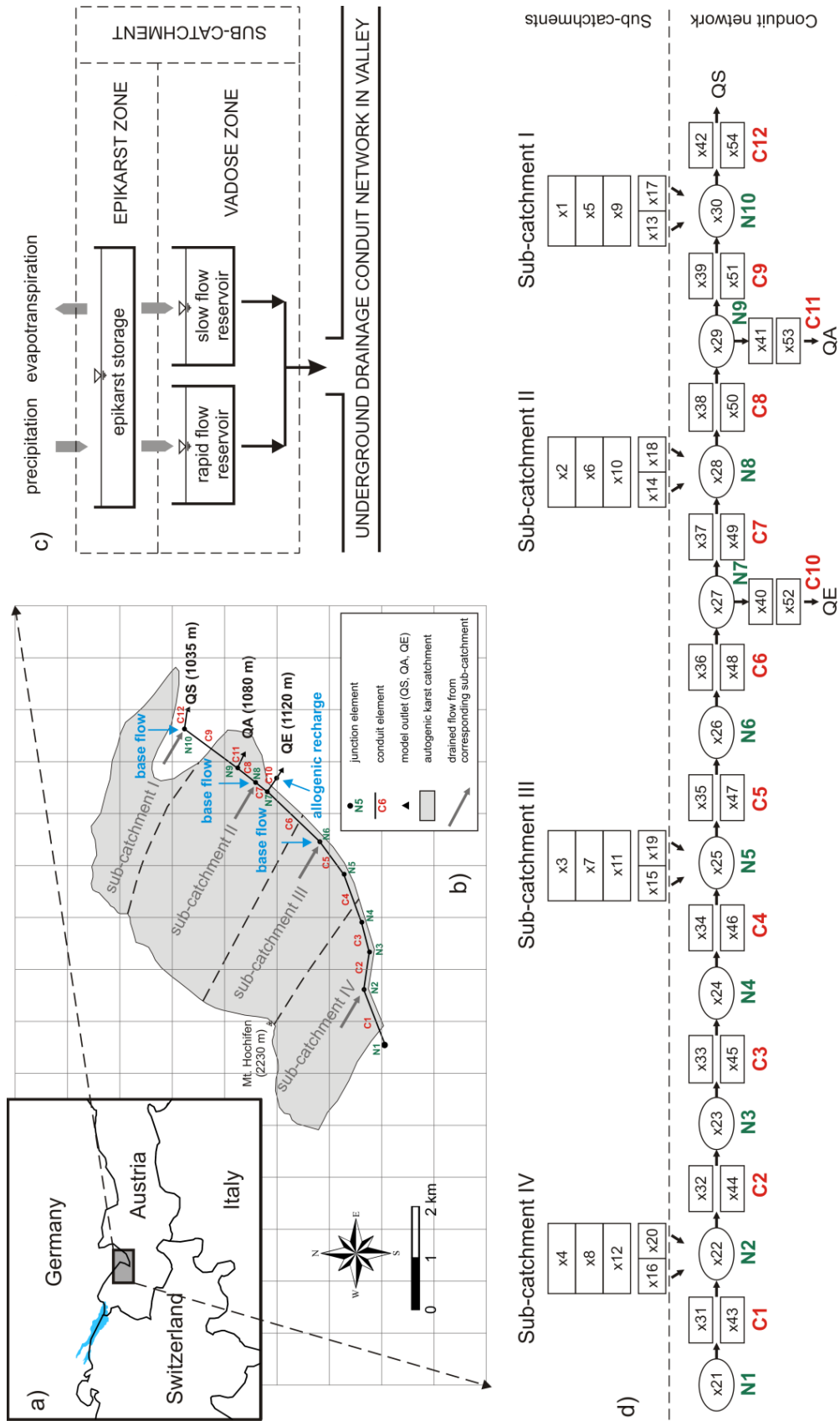
Figure 4.1: a) Location of the study area, b) map representation of the conduit network configuration in the valley and the connected sub-catchments, established by tracer tests (Goldscheider, 2005), modified after Chen and Goldscheider (2014), c) model concept for the sub-catchments and d) generalized schematic illustration of model structure and parameters listed in Table 4.1.

Table 4.1: Summary of model parameters (spatial illustration see Figure 4.1).

model part	model parameter	model location	description	unit	prior parameter bounds lower	prior parameter bounds upper	posterior parameter bounds lower	posterior parameter bounds upper
epikarst zone (catchment)	x_1	sub. I	average response delay	h	0	5	0	3
	x_2	sub. II			0	5	0	1
	x_3	sub. III			0	5	1	4
	x_4	sub. IV			0	5	2	5
	x_5	sub. I	infiltration threshold	mm	5	60	5	37
	x_6	sub. II			5	60	24	56
	x_7	sub. III			5	60	5	32
	x_8	sub. IV			5	60	31	60
	x_9	sub. I	proportion of recharge distributed into rapid flow reservoir	%	30	100	30	60
	x_{10}	sub. II			30	100	80	100
	x_{11}	sub. III			30	100	30	70
	x_{12}	sub. IV			30	100	60	100
vadose zone (catchment)	x_{13}	sub. I	effective flow width for rapid flow reservoir	m	75	500	376	500
	x_{14}	sub. II			75	500	405	500
	x_{15}	sub. III			75	500	254	500
	x_{16}	sub. IV			75	500	75	212
	x_{17}	sub. I	effective flow width for slow flow reservoir	m	10	50	10	50
	x_{18}	sub. II			10	50	10	50
	x_{19}	sub. III			10	50	27	50
	x_{20}	sub. IV			10	50	10	46
drainage conduit network	x_{21}	N1	junction elevation	m asl	1430	1450	1431	1450
	x_{22}	N2			1300	1320	1300	1320
	x_{23}	N3			1280	1300	1289	1300
	x_{24}	N4			1270	1290	1273	1290
	x_{25}	N5			1240	1260	1241	1260
	x_{26}	N6			1210	1230	1217	1230
	x_{27}	N7			1120	1130	1120	1130
drainage conduit network	x_{28}	N8	junction elevation	m asl	1105	1115	1105	1114
	x_{29}	N9			1095	1105	1096	1105
	x_{30}	N10			1020	1030	1023	1030
	x_{31}	C1	conduit diameter	m	2.0	4.0	3.3	4.0
	x_{32}	C2			2.0	4.0	2.0	4.0
	x_{33}	C3			2.0	4.0	2.0	3.7
	x_{34}	C4			2.0	4.0	2.0	2.9
	x_{35}	C5			2.0	4.0	2.9	4.0
	x_{36}	C6			2.0	4.0	2.0	3.2
	x_{37}	C7			0.6	1.0	0.6	0.9
	x_{38}	C8			2.0	4.0	2.0	4.0
	x_{39}	C9			0.6	1.0	0.6	0.8
	x_{40}	C10			2.0	4.0	2.0	4.0
	x_{41}	C11			2.0	4.0	2.0	4.0
	x_{42}	C12			2.0	4.0	2.1	4.0
	x_{43}	C1	conduit roughness	mm	10	2000	10	1999
	x_{44}	C2			10	2000	10	1568
	x_{45}	C3			10	2000	10	2000
	x_{46}	C4			10	2000	10	2000
	x_{47}	C5			10	2000	10	2000
	x_{48}	C6			10	2000	10	1379
	x_{49}	C7			10	2000	298	2000
	x_{50}	C8			10	2000	1121	2000
	x_{51}	C9			10	2000	1439	2000
	x_{52}	C10			10	2000	10	2000
	x_{53}	C11			10	2000	330	2000
	x_{54}	C12			10	2000	657	2000

4.3.2. Model optimization

We used the DiffeRential Evolution Adaptive Metropolis (DREAM) by Vrugt et al. (2009) to explore posterior parameter ranges. The simultaneous minimization of the sum of the squared errors (SSE) of multiple criteria {QS, QA and QE} was applied to constrain the model parameters. The DREAM algorithm allows an initial population of parameter sets to converge to a stationary sample, which maximizes the likelihood function. In this study, we used the initial parameter bounds based on the study by Chen and Goldscheider (2014). In total, 10000 parameter sets are generated within the prior parameter ranges. For the posterior exploration the last 2000 parameter sets of the converged sample are used to represent the posterior distribution of "behavioral" parameter sets. The posterior parameter bounds were determined using the 90 % confidence interval for these 2000 parameter sets.

4.3.3. Advanced sensitivity analysis

4.3.3.1. Sobol's method

We used Sobol's method (Sobol', 1990) for sensitivity analysis. This method has been increasingly applied for environmental modelling (e.g. Butler et al., 2014; Confalonieri et al., 2010; Hall et al., 2005; Nossent et al., 2011; Tang et al., 2007a; van Griensven et al., 2006; van Werkhoven et al., 2008; Yang, 2011; Zhan and Zhang, 2013). In Sobol's method, the variance of the model output[1] is decomposed into components that result from inputs or parameters:

$$\text{Var}[Y] = \sum_{i=1}^{k} V_i + \sum_{i=1}^{k} \sum_{j>i}^{k} V_{ij} + \cdots + V_{12\ldots k} \tag{4.1}$$

$$V_i = \text{Var}[\text{E}(Y \,|\, X_i)] \tag{4.2}$$

$$V_{ij} = \text{Var}[\text{E}(Y \,|\, X_i, X_j)] - \text{Var}[\text{E}(Y \,|\, X_i)] - \text{Var}[\text{E}(Y \,|\, X_j)] \tag{4.3}$$

---

[1] In our study, the model output is calculated in the form of the model performance metric defined in subsection 4.3.3.2.

where Var is the variance value, E the expected value, Y the model response, Var[Y] the total variance, V_i the variance contribution due to the effect of the parameter X_i and V_{ij} the variance contribution due to the interaction of the parameters X_i and X_j. If Eq. (4.1) is normalized by the total variance:

$$1 = \sum_{i=1}^{k} S_i + \sum_{i=1}^{k} \sum_{j>i}^{k} S_{ij} + \cdots + S_{12\ldots k} \tag{4.4}$$

The corresponding sensitivity indices are defined as:

$$S_i = \frac{\mathrm{Var}[\mathrm{E}(Y|X_i)]}{\mathrm{Var}[Y]} \tag{4.5}$$

$$S_{ij} = \frac{\mathrm{Var}[\mathrm{E}(Y|X_i,X_j)] - \mathrm{Var}[\mathrm{E}(Y|X_i)] - \mathrm{Var}[\mathrm{E}(Y|X_j)]}{\mathrm{Var}[Y]} \tag{4.6}$$

$$S_{Ti} = S_i + \sum_{\substack{j=1 \\ j\neq i}}^{k} S_{ij} + \sum_{\substack{i=1 \\ j\neq i, j\neq l}}^{k} \sum_{\substack{l=1 \\ l\neq i, l\neq j}}^{k} S_{ijl} + \cdots + S_{12\ldots k} \tag{4.7}$$

$$= 1 - \frac{\mathrm{Var}[\mathrm{E}(Y|X_{-i})}{\mathrm{Var}[Y]} = \frac{\mathrm{E}(\mathrm{Var}[Y|X_{-i})}{\mathrm{Var}[Y]} \tag{4.8}$$

where the first order index S_i is a measure for the variance contribution of the individual parameter X_i to the total model variance. The impact on the model output variance of the interaction between parameters X_i and X_j is given by S_{ij}, while S_{Ti} is the result of the main effect of X_i and all its interactions with the other parameters. It is impossible to calculate the variances using analytical integrals for numerical models. Hence, Monte Carlo integrals are applied in this research. Sensitivity indices S_i and S_{Ti} can be estimated after Saltelli et al. (2010) by using two independent input samples. Furthermore, the quasi-random sampling technique of Sobol' (1967; 1976) was chosen to create input samples for model evaluations.

Yang (2011) commented that monitoring the convergence and estimating the uncertainty of the sensitivity indices are crucial for environmental modeling, especially for distributed models due to their high non-linearity, non-monotonicity, highly-correlated parameters, and intensive computational requirements. We visually monitored the convergence of the calculated sensitivity indices with increasing sample size, and applied the standard bootstrap technique recommended by Archer et al. (1997) to ensure the statistical significance of the result.

4.3.3.2. Calculation procedure

The advanced sensitivity analysis is based on Sobol's method and consists of four work stages (Figure 4.2): 1) generating parameter sets using Sobol's sampling and model

evaluations for sampled parameter sets, 2) evaluation of parameter sensitivity using a multi-objective approach, 3) evaluation of parameter sensitivity using a time-varying approach and 4) illustration of Sobol's sensitivity index for model parameters in model space and time domains.
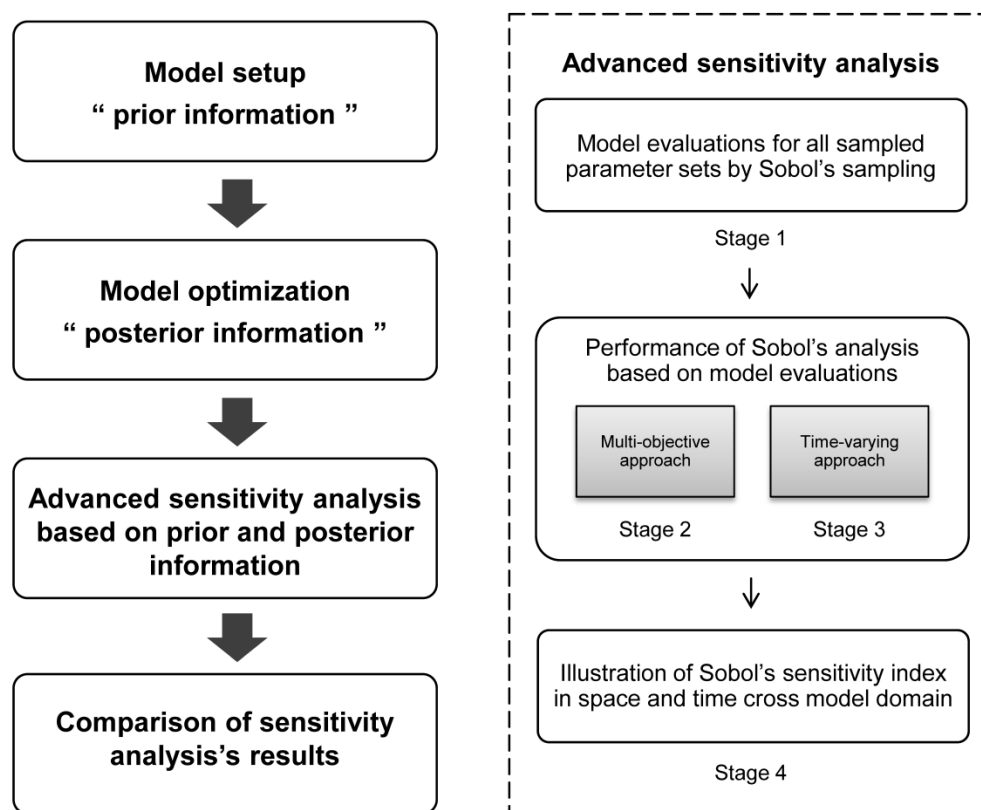
Figure 4.2: Flow chart of the proposed model evaluation approach.

At Stage 1, the sampling bounds for each model parameter in Table 4.1 are defined initially using values from the literature (prior parameter bounds) and then by posterior exploration as described in subsection 4.3.2 (posterior parameter bounds). We applied Sobol's quasi-random sampling technique (Sobol', 1967; Sobol', 1976) to sample parameter sets, and the method introduced by Saltelli (2002) to calculate the first order and total sensitivity indices using $N \times (k + 2)$ model evaluations, wherein N represents the sample size and k the parameter dimension. For a complete sensitivity analysis based on prior or posterior parameter ranges, a sample size of $N = 12000$ (corresponding to 672000 randomly-sampled parameter sets) was used, resulting 672000 model evaluations to calculate the sensitivity indices.

In distributed environmental models, parameter sensitivity could vary under different system states within the model domain (Wagener et al., 2009a). We accommodate this by performing Sobol's analysis for the different model outlet points during different hydrodynamic conditions at Stage 2. In earlier studies (e.g. Wagener et al., 2009b; Zhang

et al., 2013), various metrics were used to achieve multi-objective assessment of parameter sensitivities. In the current study, we followed the approach of Hartmann et al. (2013) and used the exceedance probability of the observed discharge at QS in the testing period. This was derived from its cumulative frequency distribution to define high flows (exceedance probabilities 0 – 0.1), medium flows (0.1 – 0.9) and low flows (0.9 – 1.0). The high, medium and low flow periods thus determined are applied to the two model outlet points QA and QE to define their high, medium and low flows. This is necessary to ensure consistency between the three hydraulically-linked springs. Sobol's analysis was performed by applying RMSE at predefined high, medium and low flow periods for individual model outlets.

The division into high, medium and low flow periods at Stage 2 was subjective and could have done in many other ways. To avoid subjective definitions of system state dependent processes, we assessed the dynamic parameter sensitivity across the entire model time domain at Stage 3. We computed Sobol's sensitivity indices using the RMSE metric repeatedly for each simulation time step for individual model outlets. It should be mentioned that this time varying sensitivity analysis can be done directly on the modelled flow since the variance of residuals and variance of simulated flows are identical when looking at a single time step and location. Thus, the analysis at Stage 3 can also be done without observation data.

At Stage 4, we elaborate the first order sensitivities of individual model parameters in space (calculated using a multi-objective approach) and time (calculated using a time-varying approach) across our model domain to identify model behavior controlling parameters. We considered $S_i < 0.01$ as insensitive and $S_i \geq 0.01$ as sensitive. In order to better understand model complexity and model internal process dynamics, we also illustrated interactions between model parameters in model space and time domains, which are defined by the residual between the total and first order sensitivity index ($S_{Ti} - S_i$) and could be identified with a threshold of 0.01.

4.3.4. Influence of parameter ranges on sensitivity analysis results

To determine the influence of parameter constraints on previous sensitivity analysis results, we compared the first order sensitivity indices and parameter interactions obtained using the prior parameter ranges with the sensitivities obtained using the posterior parameter ranges (subsection 4.3.2). A parameter with a difference of prior and posterior range sensitivity greater than 0.01 provides an increased impact on model output. For a sensitivity difference between -0.01 and 0.01, the impact on model output is unchanged, and with a difference less than -0.01, there is a decreased impact on model output.

4.4. Results

4.4.1. Parameter sensitivity under different hydrological conditions

Figure 4.3 maps the model parameter sensitivity for individual model outlets during high, medium and low flows in model space. There is a clear general spatial pattern of parameter sensitivity: the sensitivity of model parameters is closely-related to the sub-catchments of the individual springs and the conduit network in the lower part of the valley.

During low flows, conduits 7 and 9 in the drainage network were identified as sensitive. Conduit 7 hydraulically connects QA downstream and QE upstream. Conduit 9 represents the hydraulic connection between QS and QA. The sum of first order indices of their diameter and roughness parameters (x_{37}, x_{39}, x_{49} and x_{51}) is 0.18 for QS, 0.10 for QA and 0.23 for QE; i.e. corresponding to 18 %, 10 % and 23 % of the total variance of QS, QA and QE. Additionally, the parameter x_{29} (junction 9), which defines the outlet elevation of QA, contributed 31 % and 28 % to the total variance of QS and QA respectively. In comparison, the variance caused by epikarst and vadose zone parameters are clearly lower, accounting for 26 %, 6 % and 1 % for QS, QA and QE, respectively. This indicates that the conduit network geometry controls the simulated system discharge behavior during low flows. Furthermore, a characteristic pattern of contribution from sub-catchments to outlet discharge behavior could be seen: all four sub-catchments I – IV contributed to QS and sub-catchments II – IV to QA.

The conduit network geometry also controls hydrodynamic processes in the system during medium flows (Figure 4.3). Influence from the unsaturated zone in the catchment area is significantly decreased for QS and QA. The epikarst and vadose parameters contributed only 1 % to the total variance of QS, QA and QE. The connection between QS and QA (conduit 9, accounting for 78 % and 37 %) gains more importance for QS and QA than for low flow, similar to the connection between QA and QE (conduit 7, accounting for 85 %) for QE. The parameter x_{29}, which defines the QA outlet geometry, only contributed 6 % and 8 % to the total variance of QS and QA, respectively. The previous pattern of contribution from sub-catchments to outlet discharge behavior becomes "focused": sub-catchment I contributed to QS and sub-catchment II to QA.
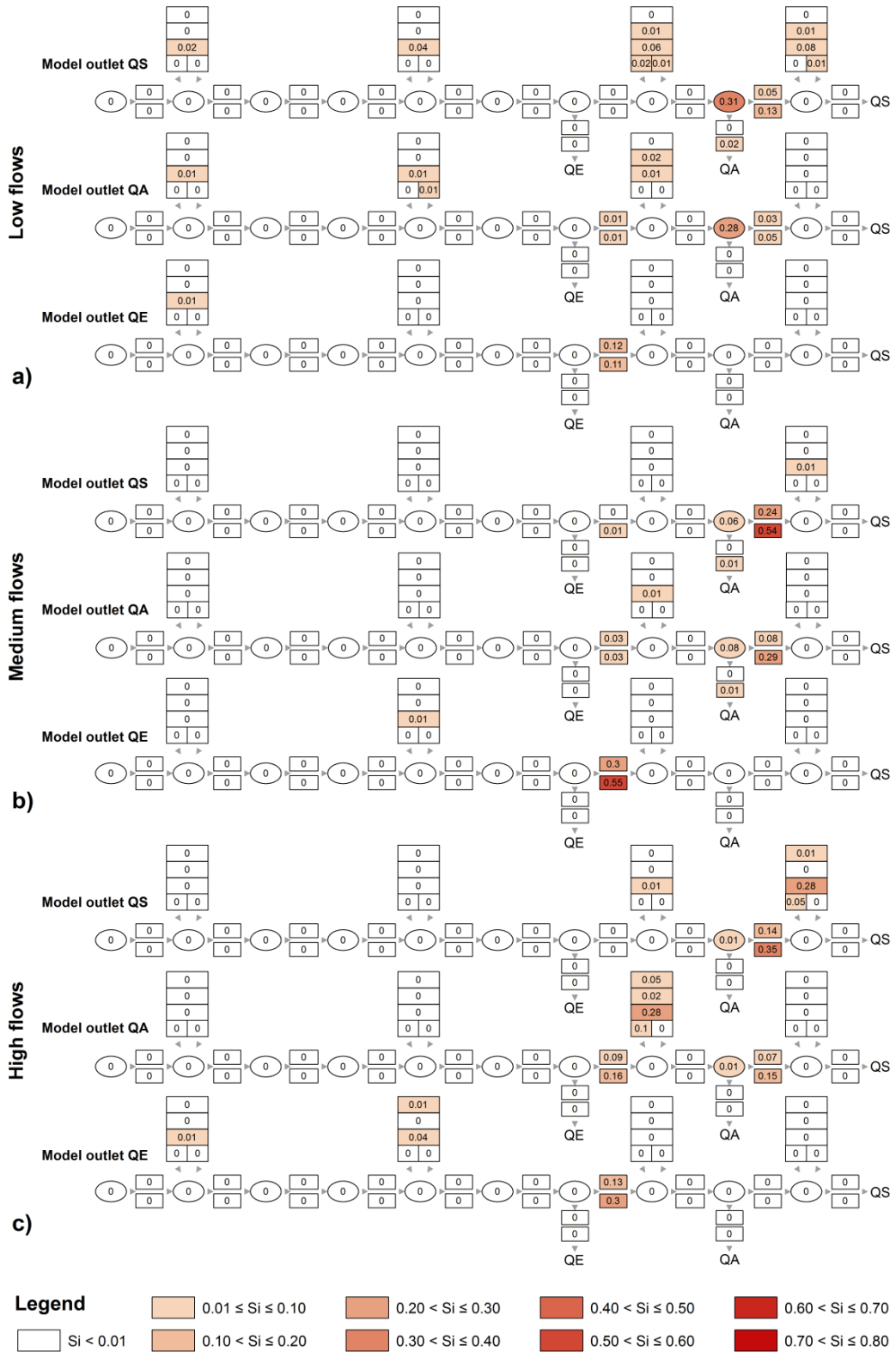
Figure 4.3: Spatial illustration of the model parameter sensitivity based on prior information for the three model outlets (QS, QA and QE) during a) low flows, b) medium flows and c) high flows.

During high flows, the previous spatial pattern of parameter sensitivity changes dramatically. The system discharge behavior is increasingly controlled by infiltration in the epikarst and rapid flow dynamics in the vadose zone (Figure 4.3). For QS, the parameters x_1, x_9 and x_{13} in sub-catchment I controlled the discharge behavior and contributed 34 % of the total variance. Similarly, the sub-catchment II corresponding parameters for QA (x_2, x_6, x_{10} and x_{14}) have strong influence on the performance of simulated high flows, accounting for 45 % of the total variance. For QE, the catchment parameters show increased parameter sensitivity relative to low and medium flows, accounting for 6 % of the total variance. For QS, QA and QE, the conduit network parameters still play a very important role, but have decreased influence relative to medium flow; contributing 50 %, 48 % and 43 % to the total variance of QS, QA and QE.

4.4.2. Time-varying parameter sensitivity

The functioning parameters known from the previous analysis and identified as sensitive during different flow conditions display temporally-varied influence on individual model outlets (Figure 4.4). A general pattern could be recognized: catchment parameters show increased influence on the system discharge behavior during the rising limb of a hydrograph, and at peak flow, when the system directly responds to rainfall. After that, i.e. during the falling limb, conduit network parameters control the system drainage behavior. This result agrees with the previous analysis. Furthermore, this information was used to identify the highly dynamic model processes, which are strongly depending on the system state.

During and immediately after rainfall events, the model parameters which represent flow mechanisms like infiltration delay, recharge distribution in slow/fast flow path in epikarst, and rapid flow in vadose zone contribute significantly to the variance of outlet discharge. These include the parameters x_1, x_9 and x_{13} for QS, the parameters x_2, x_{10} and x_{14} for QA, as well as the parameters x_3, x_4, x_{11}, x_{12}, x_{15} and x_{16} for QE. The temporal patterns of their sensitivities are relatively consistent during the different simulated rainfall events. In comparison, the epikarst storage parameters x_5, x_6, x_7 and x_8 show clearly increased sensitivity during a heavy rainfall event after a long dry period at the beginning of the testing period; because the system was under-saturated (the observed discharge of QS was minimal, while QA and QE discharges were zero). In contrast, no appreciable sensitivity for the same parameters could be measured during other rainfall events. This indicates that the epikarst storage parameters exert significant influence on the hydrodynamic behavior of the system when it is under-saturated and experiences an intense rainfall event. Also, we can observe that during dry conditions; i.e. at end of a relatively long dry period, the catchment parameters x_9, x_{10}, x_{11} and x_{12} show significantly increased impact on QS.
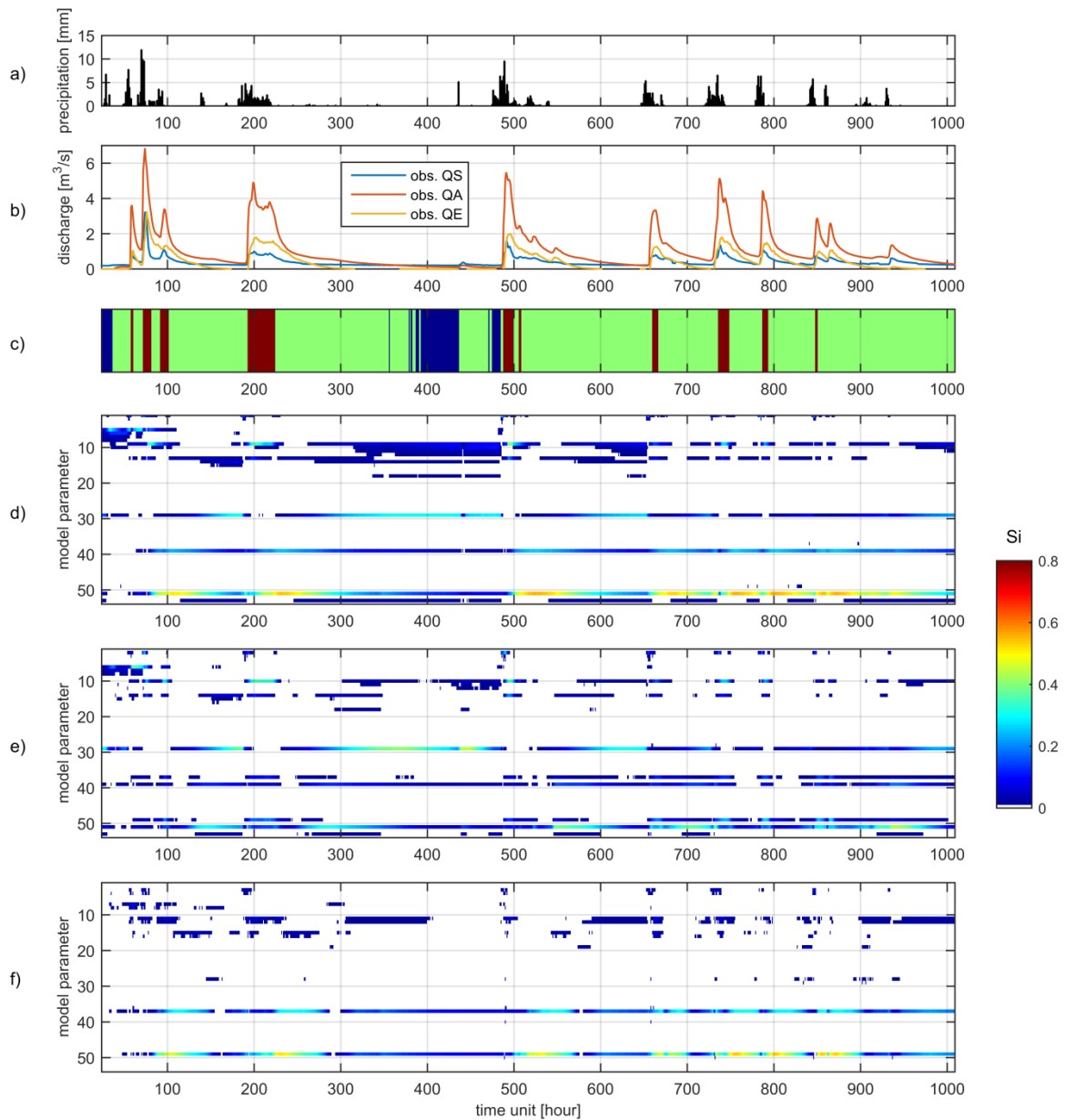
Figure 4.4: a) Mean precipitation in the study area, b) observed discharge at three system outlets QS, QA and QE, c) identified hydrological conditions (low flows in blue, medium flows in green and high flows in red), d) temporal developments of the parameter sensitivity based on prior information for the three model outlets d) QS, e) QA and f) QE during the whole testing period.

In the conduit network, changing the pressure head at QA and QE is controlled by conduit 9 (x_{39} and x_{51}) and conduit 7 (x_{37} and x_{49}), and their variations result in drainage flow variations for QA and QE directly. Because QS, QA and QE are hydraulically connected, conduits 9 and 7 simultaneously influence inflow behavior for QS and QA in the conduit network. It could be considered that conduit 9's sensitivity development for QS is related to the discharge behavior of QA, and conduit 7's sensitivity development for QA is related to the discharge behavior of QE. Because of the pressure drops at QA, the parameter x_{29}, which describes the geometry of outlet QA, influences both QA and QS drainage behavior during drought. In addition, it correlated temporally with the falling

limb behavior of QA. Moreover, the sensitivity development of x_{39} and x_{51} for QA as well as x_{37} and x_{49} for QE shows that they are characterized by high temporal variation. The reason for this could be a simulated backwater effect in the conduit network. For instance, in the case of QE; 1) the increase of the parameter sensitivity correlates well with peak flows and 2) the parameters are identified as highly sensitive during periods when QE is already dry. These indicate that the basic discharge behavior of QE and even its activation are totally dependent on the downstream conduit geometry.

4.4.3. Identification of simulated processes

We combined the information from previous analyses and found clearer evidence with respect to the state dependent processes by using the analysis of time-varying parameter sensitivity. The following spatiotemporal dynamics of the model controlling mechanisms in the modeled karst system could be identified:

1) During rainfall events and immediately after, the response from individual sub-catchments strongly influence the discharge dynamics of the outlets QA and QS, whereas the drainage flows in sub-catchments are mainly characterized by concentrated infiltration in the epikarst and rapid flow in the vadose zone. The similar hydrological characteristics of the epikarst and vadose zones were observed and described by Bakalowicz (2005); and Ford and Williams (2007). This process is also consistent with observations made inside the local cave system "Hölloch" (Höhlenverein Sonthofen, 2006).

2) In the absence of rainfall events (i.e. during drought) the influence of the diffuse flow component in sub-catchments on system discharges QA and QS is increased. The spatial contribution pattern of sub-catchments changes from "focused" during rainfall events to "distributed" during drought. By using this varied contribution pattern, the hydrodynamic link between sub-catchments and individual outlets could be evaluated in the model. The herein-identified hierarchically-structured drainage pattern across the catchment domain (QS drained sub-catchments I – IV, QA sub-catchments II – IV and QE sub-catchments III – IV) mirrors exactly results from tracer studies by Goldscheider (2005).

3) The basic system discharge behavior is predominantly controlled by the geometry of the drainage conduit network in the lower part of the valley. There, the mechanism is represented by a combination of back flooding and pressure drops in hydraulically-connected conduit systems. Similar hydrodynamic processes in real karst conduit systems were observed by Jeannin (2001), and Prelovšek et al. (2008).

4.4.4. Parameter interactions

Figure 4.5 maps the interaction between the model parameters for individual model outlets during high, medium and low flows in the model domain. We could classify three types of parameters:

1) non-influential parameters ($S_i < 0.01$ and $S_{Ti} - S_i < 0.01$)

2) insensitive but interactive parameters ($S_i < 0.01$ and $S_{Ti} - S_i \geq 0.01$)

3) sensitive and interactive parameters ($S_i \geq 0.01$ and $S_{Ti} - S_i \geq 0.01$).

In general, we found that parameter interactions varied spatially for different model outlets during different hydrodynamic conditions. During low flows, junction 9 (x_{29}), conduit 7 (x_{37} and x_{49}), conduit 9 (x_{39} and x_{51}) and conduit 11 (x_{53}) show high interactions, contributing 102 % and 124 % to the total variance of QA and QE. Also the catchment parameters x_{10}, x_{11} and x_{12} interact strongly, providing 31 % and 34 % to the total variance of QA and QE. During medium flows, a clear decrease of parameter interactions in model space could be determined for all three model outlets, except for the parameters x_{37} and x_{49}, which show clearly increased interactions for QA. During high lows, an extensive decrease of parameter interactions is observable for QA. In comparison, parameter interactions for QS are slightly increased. Also for QE, a significant increase of parameter interactions (e.g. x_{11}, x_{12}, x_{37} and x_{49}) was found, contributing 87 % to the total variance. The identified spatially-varied interactions between the model parameters indicate a highly non-linear model behavior.

To better understand the mechanism behind the spatially-varied patterns of parameter interactions during different system states, we investigated the parameter interactions calculated using the time-varying approach (step 3, Figure 4.6). This analysis identified a clear temporal correlation (especially during drought) between the conduit network geometry parameters (which describe the hydraulic connection between model outlets and model outlet's geometry), and the catchment parameters (which represent the recharge distribution in slow/fast flow path in epikarst, and rapid flow in vadose zone). Temporal correlations were identified as follows:

1) for QS, between x_9, x_{10}, x_{11}, x_{12}, x_{39}, and x_{51}

2) for QA, between x_{10}, x_{11}, x_{12}, x_{14}, x_{39}, and x_{51}

3) for QA, between x_{18} and x_{29}

4) for QE, between x_{11}, x_{12}, x_{15}, x_{16}, x_{37}, and x_{49}.
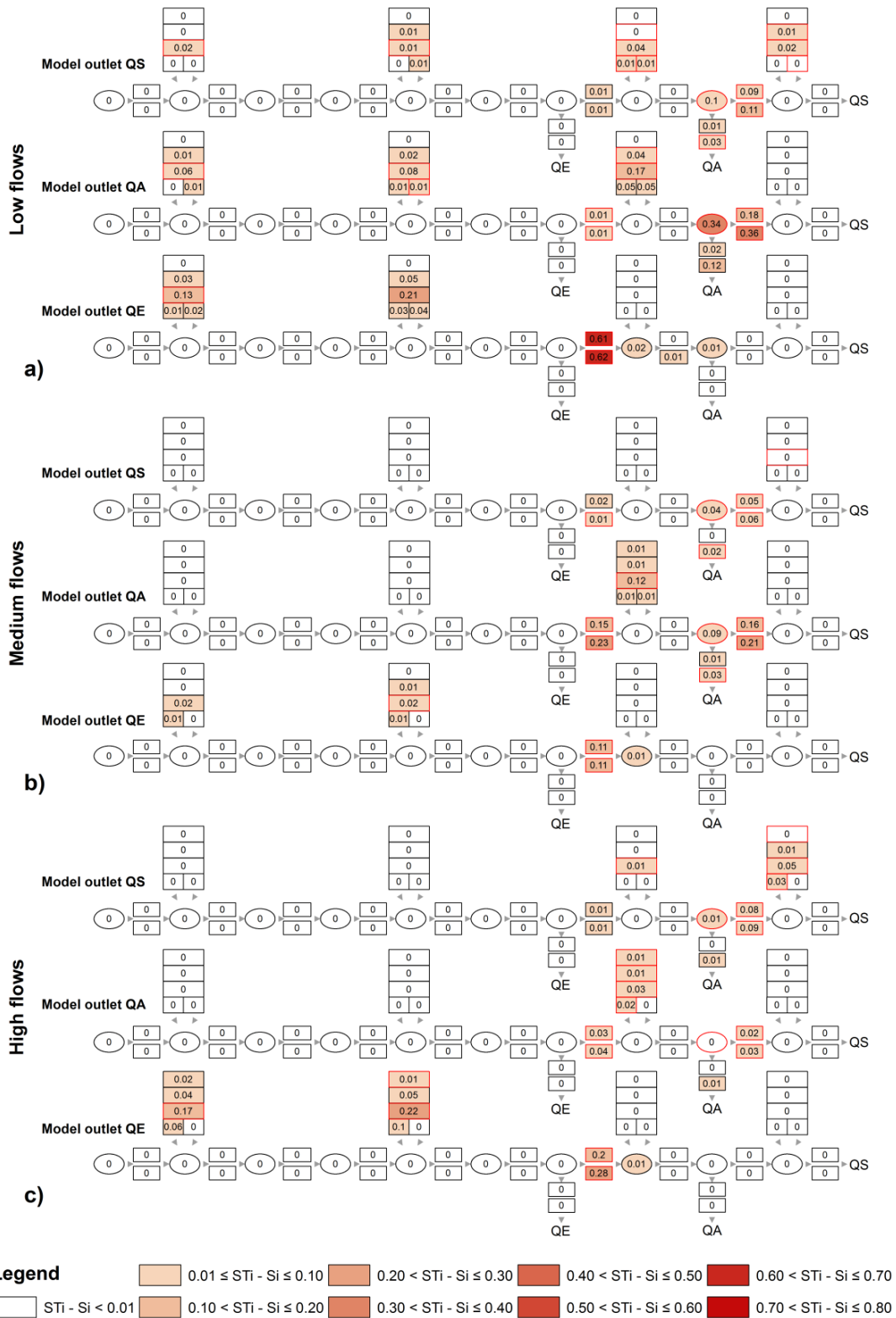
Figure 4.5: Spatial illustration of the model parameter interactions based on prior information for the three model outlets (QS, QA and QE) during a) low flows, b) medium flows and c) high flows. The parameters, which are identified as sensitive in the analysis using prior parameter ranges, are marked with red outline.
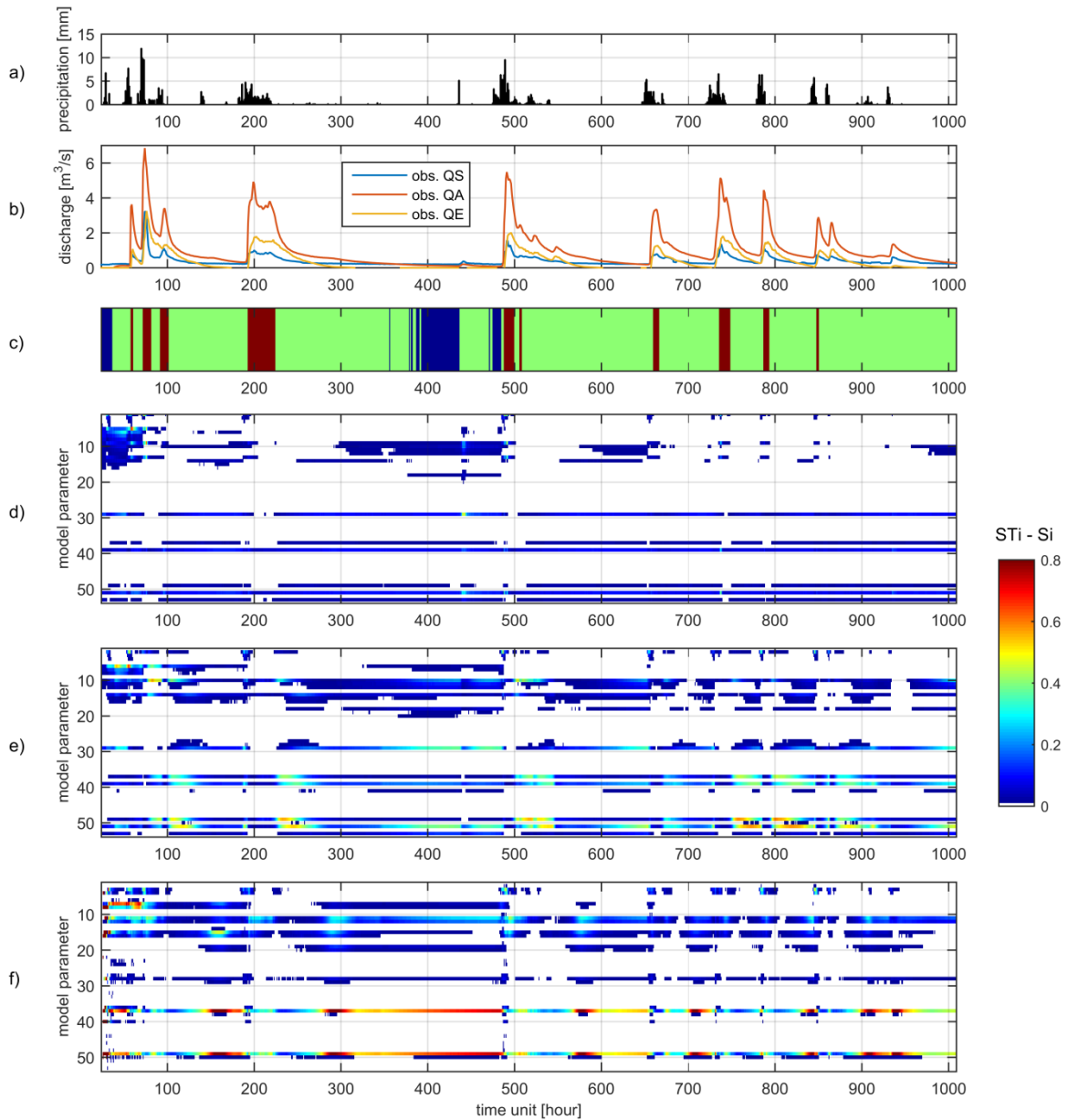
Figure 4.6: a) Mean precipitation in the study area, b) observed discharge at three system outlets QS, QA and QE, c) identified hydrological conditions (low flows in blue, medium flows in green and high flows in red), d) temporal developments of the parameter interactions based on prior information for the three model outlets d) QS, e) QA and f) QE during the whole testing period.

These correlations indicate that the model discharge behavior is temporally influenced by the interactions between hydrological and hydraulic components in the model and the temporal variations of the interactions are strongly dependent on the system saturation. It should be noted that the exact quantification of the contribution of different parameter pairs to model output variance was not possible, as the difference between the total sensitivity index and first order index lumps the interactions with all other parameters together. However, the temporal correlation between different parameter groups did give us some ideas as to where these interactions arise.

4.4.5. Influence of parameter constraints on SA's result

We assessed the model uncertainty caused by prior and posterior parameter ranges by using two different statistical metrics; RMSE and Nash-Sutcliffe Coefficient (NSC). The median of the RMSE values calculated using prior parameter ranges and posterior parameter ranges (with posterior in parentheses) are 0.47 (0.22), 0.82 (0.45), 0.41 (0.26) for QS, QA and QE (Figure 4.7). The corresponding median NSC values are -2.09 (0.52), 0.45 (0.83) and 0.37 (0.76). This shows that the tested model is able to simultaneously reproduce the discharge behavior of three hydraulically differently-functioning model outlets with the posterior parameter ranges, whereas the prior parameter ranges resulted in significantly more "bad" model runs (especially for QS), i.e. the model was constrained significantly by the DREAM algorithm.
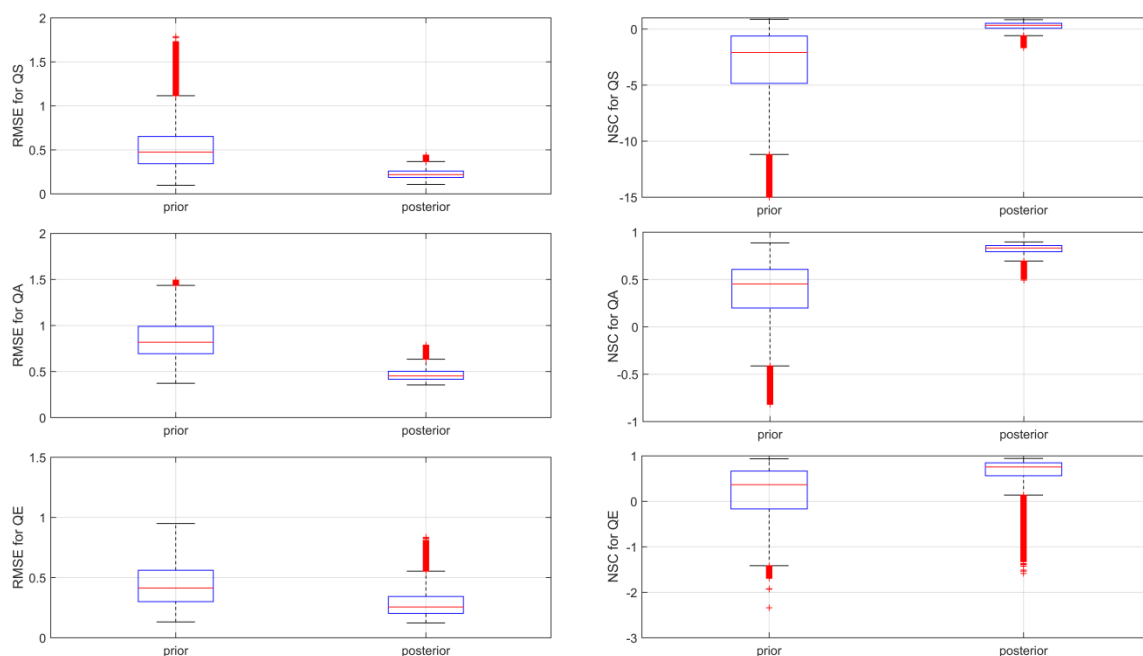
Figure 4.7: Boxplots of RMSE and Nash-Sutcliffe Coefficient values for the three model outlets (QS, QA and QE) during the whole sensitivity analysis for prior and posterior parameter ranges.

Figure 4.8 maps the impact of the parameter constraining procedure on the calculated parameter sensitivity. We see that the influence varied spatially for different model outlets during different hydrological conditions. This reveals that constraining the parameters influences the sensitivity analysis results significantly. In the conduit network, junction 9 (x_{29}), conduit 7 (x_{37} and x_{49}), conduit 9 (x_{39} and x_{51}) and conduit 11 (x_{53}) still controlled model discharge behavior. But several changes for individual parameters could be determined: 1) the impact of the roughness of conduit 10 (x_{51}) is clearly decreased for all three model outlet points during all hydrodynamic conditions, 2) the diameter of conduit 10 (x_{39}) shows increased impact on QS during different flow conditions and on QA during low flows, 3) for QA, conduit 7's sensitivity is increased during medium and high flows, and 4) for QE, conduit 7's sensitivity is increased during low flows, but

decreased during medium and high flows. Moreover, it could be seen that the spatial contribution pattern of sub-catchments changes distinctly during low flows: 1) the impact of sub-catchment II, III and IV on QS dramatically decreased, 2) for QA, only sub-catchment III contributed to outlet discharge behavior, and 3) instead of sub-catchment IV, sub-catchment III contributed to QE. In comparison with our previous results based on prior information, there are some model parameters that could be identified as sensitive at first time: 1) during low flows, x_7 for QA and x_{11} for QE, 2) x_5 and x_{17} for QS during medium and high flows and 3) x_4 for QE during high flows.

We also compared the parameter interactions calculated based on prior and posterior parameter samples (Figure 4.9). As expected, the change varied spatially for different model outlets during different system states. During low flows, parameter interactions are clearly lower for all model outlets. During medium flows, conduit 7 (x_{37} and x_{49}) clearly shows increased interactions for QA and QE, whereas the interactions of other model parameters are still small. During high flows, several catchment parameters become interactive again: 1) x_5, x_9 and x_{17} for QS, 2) x_6 and x_{10} for QA and 3) x_8, x_{11} and x_{16} for QE.
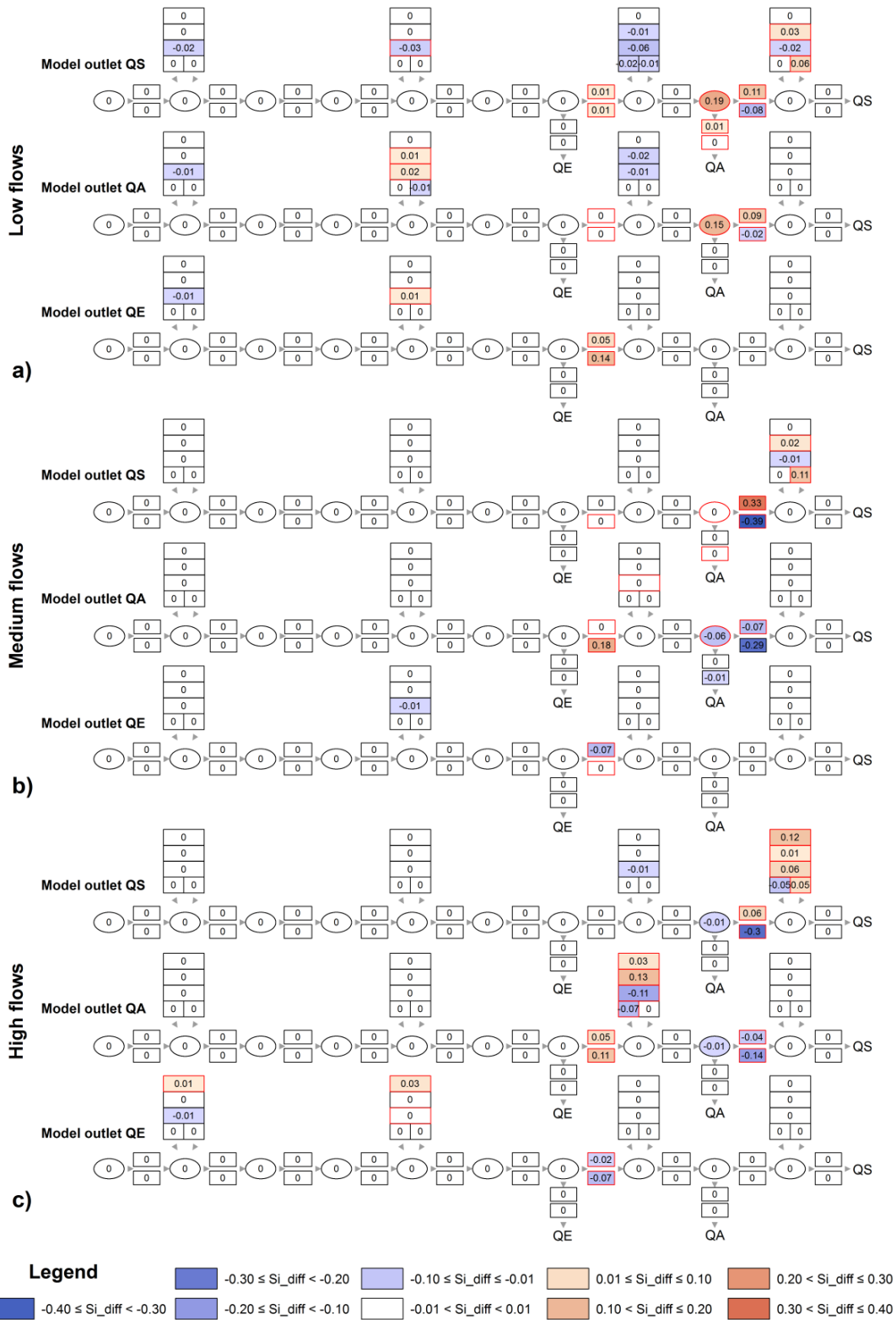
Figure 4.8: Spatial illustration of the impact of the parameter constraints on parameter sensitivity for the three model outlets (QS, QA and QE) during a) low flows, b) medium flows and c) high flows. The parameters, which are identified as sensitive in the analysis using posterior parameter ranges, are marked with red outline.
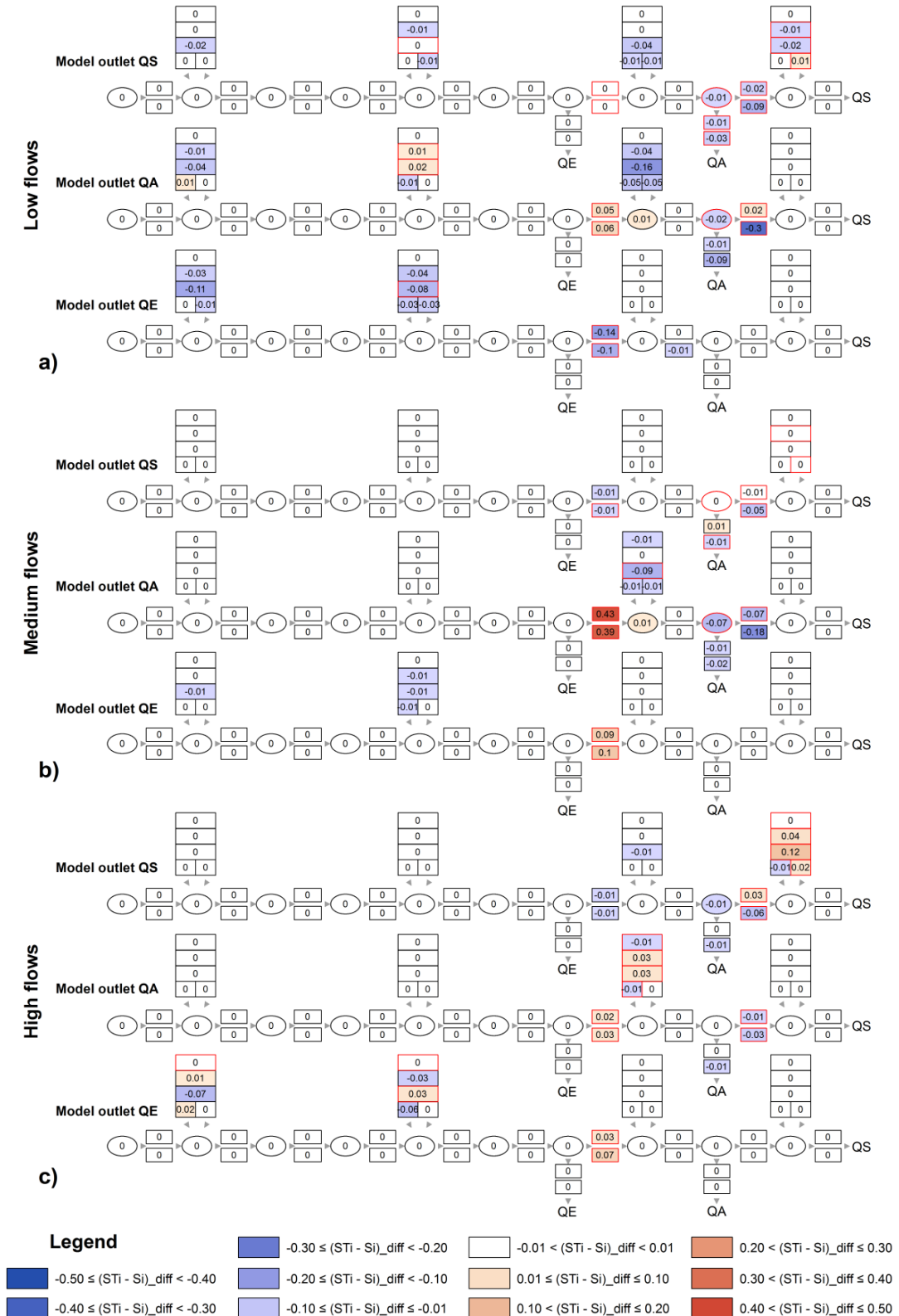
Figure 4.9: Spatial illustration of the impact of the parameter constraints on parameter interactions for the three model outlets (QS, QA and QE) during a) low flows, b) medium flows and c) high flows. The parameters, which are identified as sensitive in the analysis using posterior parameter ranges, are marked with red outline.

4.4.6. Reliability of the sensitivity analysis

A recent study revealed that, especially for small sample sizes (N), the Sobol sensitivity indices do not always converge (Yang, 2011). Therefore, we analyzed the convergence of the calculated sensitivity indices for high, medium and low flows with increasing sample size (Supplementary material). It could be shown that the sample size employed (12,000) was enough to converge for all values of S_i and S_{Ti}. For most of the parameters, even less than 6000 samples were sufficient to reach a stable value. Parameters with S_i and S_{Ti} close to 0 reach their final value very quickly, mostly at less than 2000 samples. This means that the sample size of 6000 should be sufficient for the executed sensitivity analysis. In other words, half of the computation time and cost could be saved.

4.5. Discussion

For the present work, a proper schematic model of the system functioning was available. It was established from knowledge of the conduit system obtained from tracer tests (Goldscheider, 2005; Göppert and Goldscheider, 2008) and speleological investigations (Höhlenverein Sonthofen, 2006). Across the catchment domain, hydrological properties of the epikarst and vadose zones in individual sub-catchments and the effective geometry of conduits in the drainage network lead to uncertainty regarding the main parameters/structure of the model. This uncertainty could be quantified by evaluating model performance. Accordingly, not all sampled parameter sets could represent the observed discharge behavior of springs (Figure 4.7). However these "non-behavioral" parameter sets were contained in the analysis and their contribution to model sensitivities helped us to understand the parameterization deficit and the mechanism controlling model behavior. To achieve this, we evaluated the model performance based on parameter sets which were randomly sampled from prior and posterior parameter bounds. The prior parameter bounds are based on literature values and the posterior parameter bounds are based on exploration using model optimization. In this way, we could obtain more "behavioral" parameter sets in the posterior sample. The information of "behavioral" and "non-behavioral" parameter sets were studied by comparing parameter sensitivity and interactions in the full model space domain. We assumed that the change of parameter sensitivity as well as interactions reflects the influence of removal of the "non-behavioral" parameter sets. This information provides a basis for future research. After we constrained the prior parameter sample, the remaining sensitive parameters caused the most uncertainty. Focusing on the locations and parameters requiring more accurate measurement in order to reduce the main model uncertainty could guide us to a more optimized measurement campaign for the future research.

Two approaches were used to perform sensitivity analysis: a multi-objective sensitivity analysis and a time-varying sensitivity analysis. The analyses demonstrated that the complexity of information is clearly increasing from the multi-objective sensitivity analysis approach to the time-varying sensitivity analysis approach, in turn leading to

increased knowledge about the model complexity and model internal process dynamics. A critical aspect of using the multi-objective approach for the parameter sensitivity is the choice of objective function; i.e. the separation of hydrographs for definition of different flows, which is actually quite subjective. A consequence is that parameters whose overall influence on the chosen global objective function is small, are found to be insensitive, even if they are important at specific times for the analysis (Wagener et al., 2009b). In comparison, much more complete information was obtained by using the time-varying approach, in which clearer evidence with respect to system state-dependent processes was found (demonstrated in subsection 4.4.2 and 4.4.4). However, the drawback to this approach is that the estimates could be influenced by outliers in the data (Massmann et al., 2014) which may bias the interpretations for individual time periods. For that reason, we suggest combining these two approaches. The consideration and interpretation of information from the two analyses complement each other, and lead to a more complete understanding of the dominant processes in the model.

Tang et al. (2007b) comprehensively compared Sobol's method with three other sensitivity analysis tools including the Parameter Estimation Software (PEST) (Doherty, 2004), Regional Sensitivity Analysis (RSA) (Hornberger and Spear, 1981; Young, 1978) and Analysis of Variance (Mokhtari and Frey, 2005; Neter et al., 1996). They found that Sobol's method is the most effective and robust approach to globally characterize single- and multi-parameter interactive sensitivities. Obviously, their findings are not directly transferable to our study but our analysis also revealed that the use of Sobol's method brought some detailed understanding of the model functioning and process realism (see previous subsection).

The complete work flow applied in this study can potentially be transferred to more complex true fully-distributed models, as the sensitivity measures we used are model-independent. Furthermore, Sobol's method has already been successfully applied for fully-distributed watershed models (e.g. Tang et al., 2007a; van Werkhoven et al., 2008). However the main challenges will be increased analysis and computation cost for the user. Concerning analysis cost, for a fully-distributed model the evaluation of sensitivity indices in space must be done across many locations, where the number of locations or grid cells is two or three orders of magnitude greater than in our study. Moreover, the model execution time of a complex fully distributed model could be significantly increased. This will lead to an extremely high computation cost for a complete sensitivity analysis. In this context, monitoring convergence of calculated sensitivity indices would be especially useful, as it can help to explore an optimal sample size to minimize the total computation cost. Additionally, the importance of using parallel computing to support Sobol's analysis was already highlighted by Tang et al. (2007a).

4.6. Conclusions

In this work, we proposed a novel approach based on global sensitivity analysis (Sobol's method) to evaluate the spatiotemporal dynamics of model controls in distributed environmental models. We applied our approach to an existing distributed watershed model, which is able to simulate spatially- and temporally-varied hydrodynamic behavior of a geologically complex alpine karst aquifer system. In the case study, we quantified the influence from individual model parameters by performing Sobol's analysis for spatially-distributed model outlets QS, QA and QE 1) under different hydrodynamic system conditions i.e. during low, medium and high flows in the testing period (a multi-objective approach) and 2) at hourly time steps throughout the whole testing period (a time-varying approach). The information about parameter sensitivity derived and combined from these two work stages made it possible to identify the spatial and temporal dynamics of simulated drainage flow processes in the model, and the model parameters controlling these dynamics. The results demonstrated that the identified spatiotemporally-varied drainage pattern is caused mainly by dynamics of high permeability flow in individual sub-catchments and flooding mechanisms in major conduit networks: 1) during and immediately after rainfall events, concentrated infiltration in the epikarst and rapid flow in the vadose zone from individual sub-catchments strongly influence the discharge dynamics of individual outlets. 2) After rainfall events, the influence of diffuse flow components in sub-catchments on system discharge is increased and the spatial contribution pattern of sub-catchments to the discharge behavior of individual outlets changed from "focused" to "distributed". 3) The basic system discharge behavior during dry periods is predominantly controlled by the drainage mechanism in the hydraulically-connected conduits system in the lower part of the valley. This valuable knowledge confirms that the tested model represents the conceptualization of our understanding of the relevant flow processes observed in the studied karst system and is able to transform them into realistic catchment responses. Furthermore, the results highlighted that during the evaluation of parameter sensitivities, the progression from the multi-objective approach to the time-varying approach provided valuable knowledge about the model complexity, and combining the information gained by these two approaches lad to a more complete understanding of the processes controlling the model behavior.

Also in this research, we quantified the interactions between model parameters in space and time across the model domain. The results demonstrated that the model is nonlinear and the influential parameters are highly correlated in the model space and time domain. Furthermore, the influence of parameter constraints on spatially-varying parameter sensitivity and interactions was assessed by performing complete sensitivity analysis for prior and posterior parameter ranges, in which the prior parameter bounds were based on literature values and the posterior parameter bounds were constrained using model optimization. The sensitivity indices calculated based on different parameter bounds were compared, and the results demonstrated that the parameter constraints influence the previous SA's results significantly; i.e. the spatial patterns of identified parameter

sensitivity and interactions are strongly influenced by the used parameter bounds. This highlights the importance of a proper choice of parameters bounds for SA. Within the same analysis, we could also learn about information in different model runs. In the sampling, more "non-behavioral" parameter sets were contained in the prior sampling, with more "behavioral" parameter sets in posterior sampling. The information contained in the "behavioral" and "non-behavioral" parameter sets were studied by comparing parameter sensitivity and interactions in full model space domain. The change of parameter sensitivity as well as interactions reflected the influence of the eliminated "non-behavioral" parameter sets. These results demonstrated that differences among the two parameter samples varied spatially for different model outlet points and during different hydrodynamic conditions. This allowed better differentiation between the parameter sensitivity caused by "behavioral" and "non-behavioral" parameter sets, and exploration of the parameterization deficit.

In general, it can be concluded that the new approach based on Sobol's method can be transferred to other non-stationary, spatially-distributed models of water-driven environmental systems with high complexity, high parameter interactions, and high non-linearity in order to comprehensively evaluate the spatiotemporal dynamics of model controls. For this application, the proposed calculation procedure has the advantage that the time-consuming model runs can be done once for the given parameter ranges at the beginning. The actual sensitivity analyses can just go back to the existing results of the model evaluations. Therefore, calculation of parameter sensitivity will not entail extra computation cost. However the complexity of the model under investigation should be optimized, as Sobol's sampling normally demands a large number of model runs. In this context, monitoring the convergence of sensitivity indices with increasing sample size could be used to determine the most efficient significant sample size, and to help in optimizing the implementation of Sobol's method for sensitivity analysis.

Acknowledgments

Supplementary material
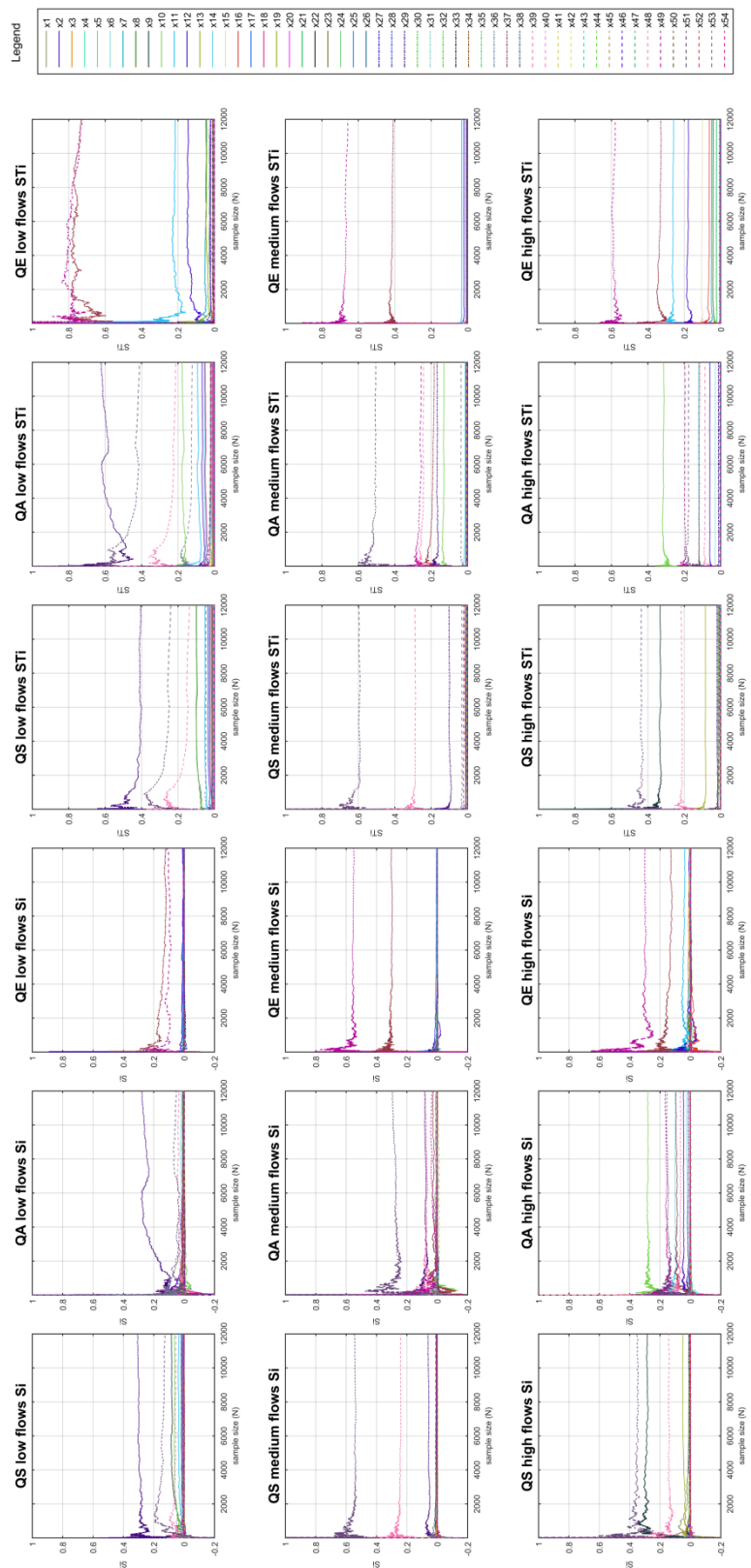
Figure S4.1: Evolution of sensitivity indices during sensitivity analysis based on prior parameter ranges.
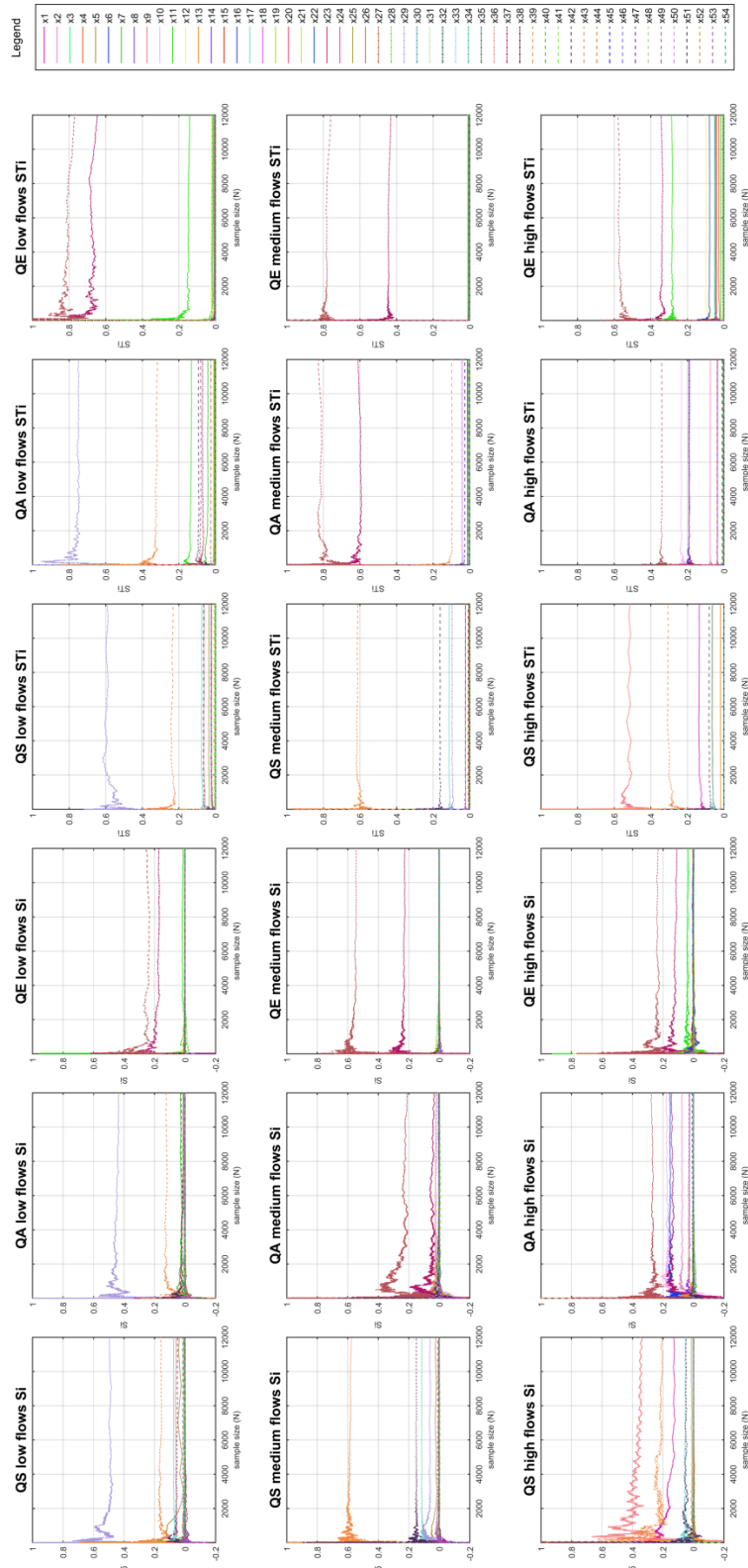
Figure S4.2: Evolution of sensitivity indices during sensitivity analysis based on posterior parameter ranges.

Chapter 5

Dynamics of water fluxes and storages in an Alpine karst catchment under current and potential future climate conditions

Abstract

Climate change projections indicate significant changes to precipitation and temperature regimes in European karst regions. Alpine karst systems can be especially vulnerable under changing hydro-meteorological conditions since snowmelt in mountainous environments is an important controlling process for aquifer recharge, and is highly sensitive to varying climatic conditions. The current study presents an investigation of present and future water fluxes and storages at an Alpine karst catchment using a distributed numerical model. A delta approach combined with random sampling was used to assess the potential impacts of climate changes. The study site is characterized by high permeability (karstified) limestone formations and low permeability (non-karst) sedimentary flysch. The model simulation under current conditions demonstrates that a large proportion of precipitation infiltrates into the karst aquifer as autogenic recharge. Surface runoff in the adjacent non-karst areas partly infiltrates into the karst aquifer as allogenic point recharge. Moreover, the result shows that surface snow storage is dominant from November to April, while subsurface water storage in the karst aquifer dominates from May to October. The climate scenario runs demonstrate that varied climate conditions significantly affect the spatiotemporal distribution of water fluxes and storages: (1) the total catchment discharge decreases under all evaluated future climate conditions. (2) The spatiotemporal discharge pattern is strongly controlled by temperature variations, which can shift the seasonal snowmelt pattern, with snow storage in the cold season (December to April) decreasing significantly under all change scenarios. (3) Increased karst aquifer recharge in winter and spring, and decreased recharge in summer and autumn, partly offset each other. (4) Impacts on the karst springs are distinct; the permanent spring presents a "robust" discharge behavior, while the estavelle is highly sensitive to changing climate. This analysis effectively demonstrates that the impacts on subsurface flow dynamics are regulated by the characteristic dual flow and spatially

heterogeneous distributed drainage structure of the karst aquifer. Overall, our study suggests that bespoke hydrological models tailored to the specific subsurface characteristics of an Alpine karst catchment are needed to understand climate change impact.

5.1. Introduction

The Alps, called the "water tower of Europe", form headwaters for important regional river systems (Viviroli et al., 2007). Alpine catchments are generally characterized by above-average precipitation due to orographic effects, as well as by colder temperatures resulting in lower evapotranspiration and temporary water storage in the form of snow and ice (Zierl and Bugmann, 2005). Climate projections indicate that a shift in snow and precipitation patterns is likely to alter catchment runoff regimes (Gobiet et al., 2014). Additionally, extreme events, such as floods and droughts, are expected to increase in frequency and intensity (Dobler et al., 2013; Rössler et al., 2012). For sustainable management of water resources in Alpine areas, it is imperative to understand the complex mountain hydrological processes (Kraller et al., 2012).

In this context, numerical models are usually applied to describe the hydrological processes in Alpine catchments (Abbaspour et al., 2007; Achleitner et al., 2009; Benischke et al., 2010; Braun and Renner, 1992; Junghans et al., 2011; Kraller et al., 2012). Lumped conceptual simulation models are easy to use in gauged catchments because their parameters can be effectively found via calibration. On the other hand, distributed simulation models are required for studying the spatial patterns of hydrological processes across a catchment. However, spatially-distributed models face challenges in Alpine areas concerning the assessment of input variables and model parameters (Kraller et al., 2012; Kunstmann and Stadler, 2005). Furthermore, most distributed models focus on surface hydrological variables (e.g. vegetation, soil and snow cover) or/and anthropogenic variables (e.g. land use and water use), with relatively poor subsurface representations. Few studies (e.g. Kraller et al., 2012; Kunstmann et al., 2006; Kunstmann and Stadler, 2005) explicitly considered subsurface processes such as recharge, drainage and storage in their models. It is generally accepted that the geological and lithological setting for mountainous catchments are often complex and could have significant impact on the catchment flow regime (Goldscheider, 2011; Rogger et al., 2013). The situation is even more complex when mountain ranges within a catchment consist of highly permeable limestone formations characterized hydraulically by fissures and/or conduit drainage networks, and concentrated discharge via springs (Goldscheider, 2005; Gremaud et al., 2009; Lauber and Goldscheider, 2014). In order to better understand complex hydrological processes at mountainous karstic catchment as well as quantify their dynamics, this study presents a spatially-distributed investigation of the water fluxes and storages in a high-elevation Alpine catchment considering its complex subsurface heterogeneous drainage structure. The study catchment constitutes an optimal

test case to explore complex hydrological processes since it includes many typical characteristics of Alpine catchments, such as a seasonal snow cover, a large range of elevations and a highly varied catchment flow regime. Furthermore, the hydrogeology in the investigated catchment is complex. It is characterized by high permeability limestone formations (karst areas) and low permeability flysch[2] sedimentary rocks (non-karst areas) as described by Goldscheider (2005). Here, we expanded an existing model (Chen and Goldscheider, 2014) by adding a snow accumulation/melting routine with high spatiotemporal resolution. We also developed a tailored calibration strategy, building on a previous sensitivity analysis by Chen et al. (2017), to calibrate the proposed catchment model reasonably and effectively.

Several recent studies indicated the significant impact of climate change on the catchment discharge behavior of Alpine areas, and demonstrated the changing characteristics of flow regimes including amount, seasonality, minima and maxima, as well as impacts on other hydrological variables, e.g. soil moisture and snow cover (Dobler et al., 2012; Jasper et al., 2004; Kunstmann et al., 2004; Middelkoop et al., 2001; Rössler et al., 2012; Zierl and Bugmann, 2005). However, the relationship between subsurface hydrological processes (recharge, storage and discharge) and changing climate conditions has not yet been considered in any detail. Gremaud et al 2009 and Gremaud and Goldscheider 2010 studied a geologically complex, glacierised karst catchment in Alps by combining tracer tests and hydrological monitoring and found that the changing hydro-meteorological conditions affect the water storage in snow and ice significantly, which have high impact on the aquifer recharge processes and discharge dynamics. Finger et al 2013 investigated glacier meltwater runoff in a high Alpine karst catchment under present and future climate conditions using tracer experiments, karst structure modeling and glacier melt modeling. The results indicated that parts of the glacier meltwater are drained seasonally by underlying karst system and the expected climate change may jeopardize the water availability in the karst aquifer. In order to better understand climate change effects on complex hydrological processes in Alpine karstic environment, we assessed the impacts of varied climate conditions on the water fluxes and storages in the simulated model domain, and we identified the hydrological processes most sensitive to potential climate change. For this analysis, we used a pragmatic and widely used delta approach to project the climate change in the model domain (e.g. Dobler et al., 2012; Lenderink et al., 2007; Singh et al., 2014).

---

[2] The flysch formations consist of an interstratification of claystone, impure sandstone, marl and thin-bedded limestone

5.2. Study area

The study catchment is located in the northern Alps on the Germany/Austria border (Figure 5.1a). It has an area of about 35 km^2, and an altitude varying between 1000 m asl (the lowest part of the Schwarzwasser valley) and 2230 m asl (the summit of Mt. Hochifen). The climate in the area is cool-temperate and humid. The nearest permanent weather station lies to the east in the Breitach valley at an altitude of 1140 m asl. There, the mean monthly temperature ranges from -2.2 °C in January to 14.4 °C in July, with an annual average of 5.7 °C (based on data from 1961 to 1990, available from Water Authority Vorarlberg). The mean annual precipitation is 1836 mm with a maximum in June-August and a secondary maximum in December-January. Snow accumulates commonly between November and May.

Hydrogeologically, the investigated catchment can be divided into karst and non-karst areas, whose boundary is more or less marked by the Schwarzwasser river. The karst area is characterized by the highly permeable Schrattenkalk limestone formation (with about 100 m thickness), which is underlain by marl formations. The underground flow paths in the karst system are controlled by local folds and follow plunging synclines. The karst aquifer system discharges in several springs (a permanent spring QS, a large but intermittent overflow spring QA and an estavelle [3] QE) at different elevations (and recharged directly from precipitation) as well as indirectly in surface streams that drain the non-karst area. These are formed by low to moderately permeable flysch sedimentary rocks. Several quantitative multi-tracer tests (Goldscheider, 2005; Göppert and Goldscheider, 2008; Sinreich et al., 2002) revealed two parallel drainage systems in this valley: a surface stream and a continuous underground karst drainage system along the valley axis, which are hydraulically connected in the upper part of the valley.

---

[3] Opening in karstic terrane which acts as a discharge spring during high flow conditions and as a swallow hole during low flow conditions
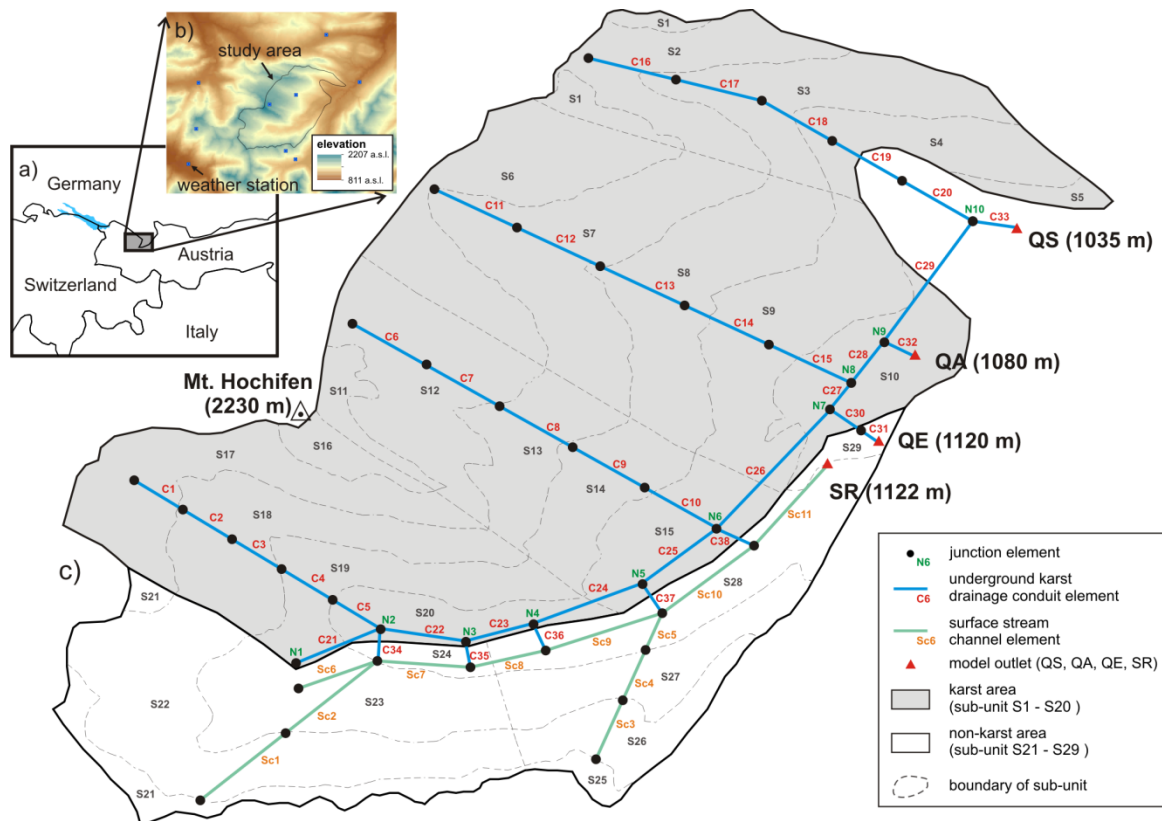
Figure 5.1: a) Location of the study area, b) digital elevation model with grid size 100 m × 100 m for the studied catchment and its surrounding area with weather stations used for the interpolation of meteorological parameters and c) model configuration (modified after Chen and Goldscheider 2014).

5.3. Methodology

5.3.1. Setup of the catchment model

Our model is based on the existing distributed karst catchment model by Chen and Goldscheider (2014), which in turn has been derived from the distributed hydrologic-hydraulic water quality simulation model – Storm Water Management Model (SWMM, version 5.0) developed by the U.S. Environmental Protection Agency (Rossman, 2010). The hydrological conceptual model was developed mainly based on the geologic study by Wagner (1950), the speleological investigation by the regional caving club (Höhlenverein Sonthofen, 2006) and numerous hydrogeological field experiments by Goldscheider (2005). Additional tracer experiments by Göppert and Goldscheider (2008) and Sinreich et al. (2002) improved this conceptual model.

Compared to the existing karst catchment model, new developments are: (1) the model domain is extended to the non-karst area of our study site to consider the surface runoff generated from low permeability flysch formations, which can infiltrate into the underground karst drainage network in the upper part of the valley (Figure 5.1c and 5.2a),

(2) we considered the slow flow for individual karst sub-catchments, which should approximately represent long term matrix flow (Figure 5.2), and (3) the space- and time-varying snow accumulation and melt are included (described in section 5.3.3). In line with these changes, the whole model domain is divided into 4 karst sub-catchments due to underground drainage systems and 2 non-karst sub-catchments due to surface streams, which consist of 29 sub-units, divided by 6 elevation bands. The karst and non-karst catchments are hydraulically connected, i.e. the underground karst drainage conduits are connected with the surface stream channels in the upper part of the valley. In total, 76 model parameters (Supplementary material) are considered for the model setup: (1) Model parameters x1 – x20 define the main hydrological processes of the unsaturated zone in the individual karst sub-catchments and the top layer of the low permeable flysch rocks, (2) model parameters x21 – x76 describe the geometry and hydraulic properties of the karst drainage conduit network as well as surface stream channels in the non-karst area.
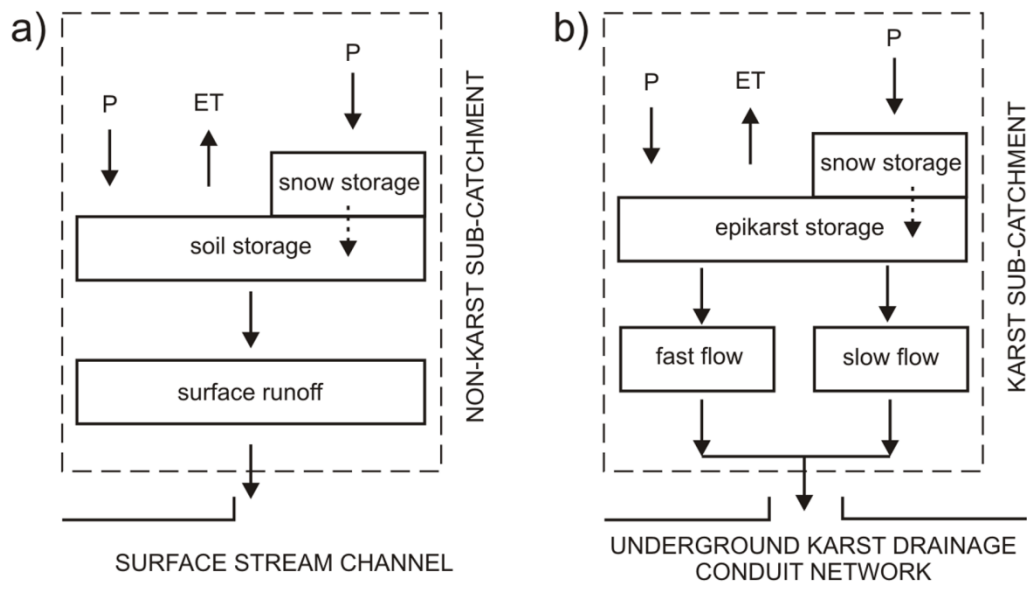
Figure 5.2: a) Model concept for the sub-catchments in the non-karst area and b) model concept for the sub-catchments in the karst area.

5.3.2. Monitoring network and data availability

Four observation locations in the studied catchment were considered here: (1) QS at 1035 m asl in the valley, (2) QA at 1080 m asl, (3) QE at 1120 m asl and (4) a gauging station (SR) at 1122 m asl quantifying the surface runoff from the upper part of Schwarzwasser valley. Hourly measured discharges at the above-mentioned monitoring stations are used, whereas the measurements for QS and QA are available from November 2013 to October 2014, for QE and SR only from July to October 2014. For the

same period, we interpolated the meteorological data (hourly precipitation, air temperature and relative humidity) from nine weather stations (Figure 5.1b) across the study catchment at a 100 m × 100 m grid resolution using combined inverse distance weighting and linear regression gridding. Mean areal precipitation and potential evapotranspiration for individual sub-units are determined based on the interpolated meteorological data, in which hourly potential evapotranspiration is estimated using a modified Turc-Ivanov approach after Wendling and Müller (1984).

5.3.3. Modeling snow accumulation and melting

We adopted a simple, widely used (e.g. Bergström, 1975; Kollat et al., 2012; Seibert, 2000) degree-day approach to modeling snow. We further modified the calculation of snowmelt using the approach proposed by Hock (1999), to simulate more realistic hourly varied snow melting in mountainous catchments:

$$M = \begin{cases} (MF + \alpha \times I) \times (t - Ts), & t > Ts \\ 0, & t \leq Ts \end{cases} \qquad (5.1)$$

Where M is snowmelt (mm h^{-1}), MF is melt factor (mm h^{-1} °C^{-1}), α is radiation coefficient, I is potential clear-sky direct solar radiation at surface (W m^{-2}), t is measured hourly air temperature (°C) and Ts is threshold temperature (°C) for snow melting. The melt factor and the radiation coefficient are empirical coefficients and can be estimated by model calibration. The distributed potential clear-sky direct solar radiation is dependent on surface topography and calculated with 100 m × 100 m grid resolution for the investigated area using the approach developed by Kumar et al. (1997).

5.3.4. Model calibration

5.3.4.1. Model optimization

We used the DiffeRential Evolution Adaptive Metropolis (DREAM) by Vrugt (2016) to calibrate the model. The simultaneous minimization of the sum of the squared errors (SSE) of multiple observed time series was applied to constrain the model parameter space (described in section 5.3.4.2), which was defined based on our previous experience in the study region (Chen and Goldscheider, 2014; Chen et al., 2017). The DREAM algorithm allows an initial population of parameter sets to converge to a stationary sample.

5.3.4.2. Calibration strategy

In a previous comprehensive sensitivity analysis we demonstrated that the controlling parameters exhibit varying sensitivity for different hydrodynamic conditions and for different spatially-distributed model outlets (Chen et al., 2017). Based on this information,

we designed four steps to calibrate the model using different hydrodynamic system conditions and the observed time series for different outlets. Additionally, to explicitly consider or completely remove the snow dynamic during calibration, we divided the whole simulation period into a snow period (November 2013 – June 2014) and a rainfall period (June 2014 – October 2014). There was no snow cover anywhere in the catchment during the rainfall period.

		Hydrodynamic conditions	Simulation period		Target model domain	Observation time series
Constraining parameter ranges	Step 1	MF - HF		No melt	Unsaturated zone + drainage network	QS, QA, QE and SR
	Step 2	MF - HF	Snow and melt		Snow storage	QS and QA
	Step 3	LF	Snow and melt		Snow storage + unsaturated zone + drainage network	QS and QA
	Step 4	LF - HF	Snow and melt	No melt	Snow storage + unsaturated zone + drainage network	QS, QA, QE and SR

Figure 5.3: Strategy for the multi-step model calibration, where LF / MF / HF are for low / medium / high flow conditions.

The multi-step calibration procedure applied here is illustrated in Figure 5.3. In step 1, we used the rainfall period to constrain the model parameters of the unsaturated zone and the drainage network during medium and high flows. The different hydrodynamic conditions are defined using the exceedance probability of the observed discharge at QS. In step 2, we used the snow period to constrain the parameters of snow storage during medium and high flows, whereas in the observation data the snow accumulation and melting dynamics in the catchment are clearly reflected. The time series of QS and QA are used for this calibration step. In step 3, we focused on the low flows in the same simulation period as during step 2 to further constrain the parameters of storage in snow, unsaturated zone and drainage network using the observation data of QS and QA. In step 4, the ranges of the previous parameters were constrained continuously using all flow conditions and observation time series from all four outlets.

The error function used in DREAM is the sum of the SSE values defined in individual calibration steps (Eq. 5.3 for step 1 and 4; Eq. 5.4 for step 2 and 3):

$$SSE = \sum_{t=1}^{N}\left(Q_{t,o} - Q_{t,s}\right)^2 \tag{5.2}$$

Where $Q_{t,o}$ is the observed discharge at time step t, $Q_{t,s}$ is the simulated discharge at time step t and N is the number of measurements in the selected time series.

$$SSE_{Objective1} = SSE_{QS} + SSE_{QA} + SSE_{QE} + SSE_{SR} \tag{5.3}$$

$$SSE_{Objective2} = SSE_{QS} + SSE_{QA} \tag{5.4}$$

For each calibration step, 5000 parameter sets were generated using Latin Hypercube sampling within the defined prior parameter ranges. The last 1000 parameter sets of the converged sample in each calibration step are used to represent the posterior distribution of "best" parameter sets. Posterior parameter bounds are determined using the 95 % confidence interval for these 1000 parameter sets. The parameter bounds of a previous step were adopted as a-priori parameter bounds for the subsequent calibration step.

5.3.5. Estimation of water storage

To understand water storage processes within the catchment, we estimated the temporary water storage volumes for the entire catchment (Eq. 5.5), karst area (Eq. 5.6) and non-karst area (Eq. 5.7):

$$S_{t,catchment} = \sum_{t_0}^{t} (P_{t,catchment} - ET_{t,catchment} - Q_{t,catchment}) \tag{5.5}$$

$$S_{t,karst} = \sum_{t_0}^{t} (P_{t,karst} + R_{t,allogenic} - ET_{t,karst} - Q_{t,karst}) \tag{5.6}$$

$$S_{t,nonkarst} = \sum_{t_0}^{t} (P_{t,nonkarst} - R_{t,allogenic} - ET_{t,nonkarst} - Q_{t,nonkarst}) \tag{5.7}$$

Surface runoff from the non-karst area can infiltrate into the underground karst drainage network because the non-karst and karst areas are hydraulically connected in the upper part of the valley. Infiltration is considered as allogenic recharge for the karst area and was taken into account for the storage calculation for the non-karst area. Additionally we simulated the temporary subsurface water storage volume for the karst aquifer (Eq. 5.8):

$$S_{t,karstaquifer} = \sum_{t_0}^{t} (R_{t,autogenic} + R_{t,allogenic} - Q_{t,karst}) \tag{5.8}$$

Where S_t, P_t, ET_t, R_t and Q_t are the storage, precipitation, evapotranspiration, recharge and discharge in volume at time step t (t_0 is first simulation time step). The simulated temporary storage volumes for the whole catchment ($S_{t,catchment}$), karst area ($S_{t,karst}$) and karst aquifer ($S_{t,karstaquifer}$) are not the absolute volumes, as the calculation is referred to the initial water storage volume in the karst aquifer, which is set at t_0 and cannot be taken into account.

5.3.6. Climate change projections

The focus of this analysis is to quantify the impact of varying climate conditions on the water fluxes and storages throughout the model domain and to identify the hydrological processes most sensitive to potential climate change within the study catchment. We chose the probabilistic scenarios of precipitation and temperature by Frei (2004) for the northern Alps as the basis for our study. The median values (q0.5) and the confidence intervals (q0.025 to q0.975) of the probabilistic scenarios for years 2030, 2050 and 2070 were derived in Frei (2004) and given in Table 5.1. We used a delta approach to project the potential climate change scenarios in the investigated catchment by changing precipitation and temperature time series for the pre-defined months (December – February, March – May, June – August and September – November) by a given delta (percentage or value). For the analysis, we first focused on the median climate scenarios of 2030, 2050 and 2070 (described in section 5.4.3.1) to better understand the general trend of the climate change projections. In the second part of the analysis, we considered the uncertainty in the climate scenario for 2070 and estimated its impact on the simulated water fluxes and storages across the model domain (described in section 5.4.3.2). To consider the climate change scenario uncertainty, 1000 uniformly distributed random samples within the defined confidence intervals for the deltas of precipitation and temperature are used.

5.4. Results

5.4.1. Model performance

Figure 5.4 shows the simulated karst spring discharges as well as the surface runoff generated from the non-karst area of the final calibrated model. The transient and highly variable discharge behavior at the four spatially-distributed model outlets is simultaneously simulated at an hourly time step. The quality of the model simulation is demonstrated by two different statistical criteria, RMSE and Nash-Sutcliffe Coefficient (NSC): RMSE values are 0.118 m^3/s for QS, 0.448 m^3/s for QA, 0.419 m^3/s for QE and 0.248 m^3/s for SR. NSC values are 0.71 for QS, 0.80 for QA, 0.74 for QE and 0.66 for SR.

Table 5.1a: The median (q0.5) and the confidence intervals (q0.025 and q0.975) of the probabilistic precipitation scenarios for year 2030, 2050 and 2070 are explicitly given as percentage change (compared to 1990) and applied for the analysis described in section 5.3.6.

season	precipitation scenario (%)								
	2030			2050			2070		
	q0.025	q0.5	q0.975	q0.025	q0.5	q0.975	q0.025	q0.5	q0.975
Dec/Jan/Feb	-1	+4	+11	-1	+8	+21	-1	+11	+30
Mar/Apr/May	-6	0	+5	-11	-1	+10	-15	-1	+13
Jun/Jul/Aug	-18	-9	-3	-31	-17	-7	-41	-23	-9
Sep/Oct/Nov	-8	-3	0	-14	-6	-1	-20	-9	-1

Table 5.1b: The median (q0.5) and the confidence intervals (q0.025 and q0.975) of the probabilistic temperature scenarios for year 2030, 2050 and 2070 are explicitly given as absolute change (compared to 1990) and applied for the analysis described in section 5.3.6.

season	temperature scenario (°C)								
	2030			2050			2070		
	q0.025	q0.5	q0.975	q0.025	q0.5	q0.975	q0.025	q0.5	q0.975
Dec/Jan/Feb	+0.4	+1	+1.8	+0.9	+1.8	+3.4	+1.2	+2.6	+4.7
Mar/Apr/May	+0.4	+0.9	+1.8	+0.8	+1.8	+3.3	+1.1	+2.5	+4.8
Jun/Jul/Aug	+0.6	+1.4	+2.6	+1.4	+2.7	+4.7	+1.9	+3.8	+7
Sep/Oct/Nov	+0.5	+1.1	+1.8	+1.1	+2.1	+3.5	+1.7	+3	+5.2
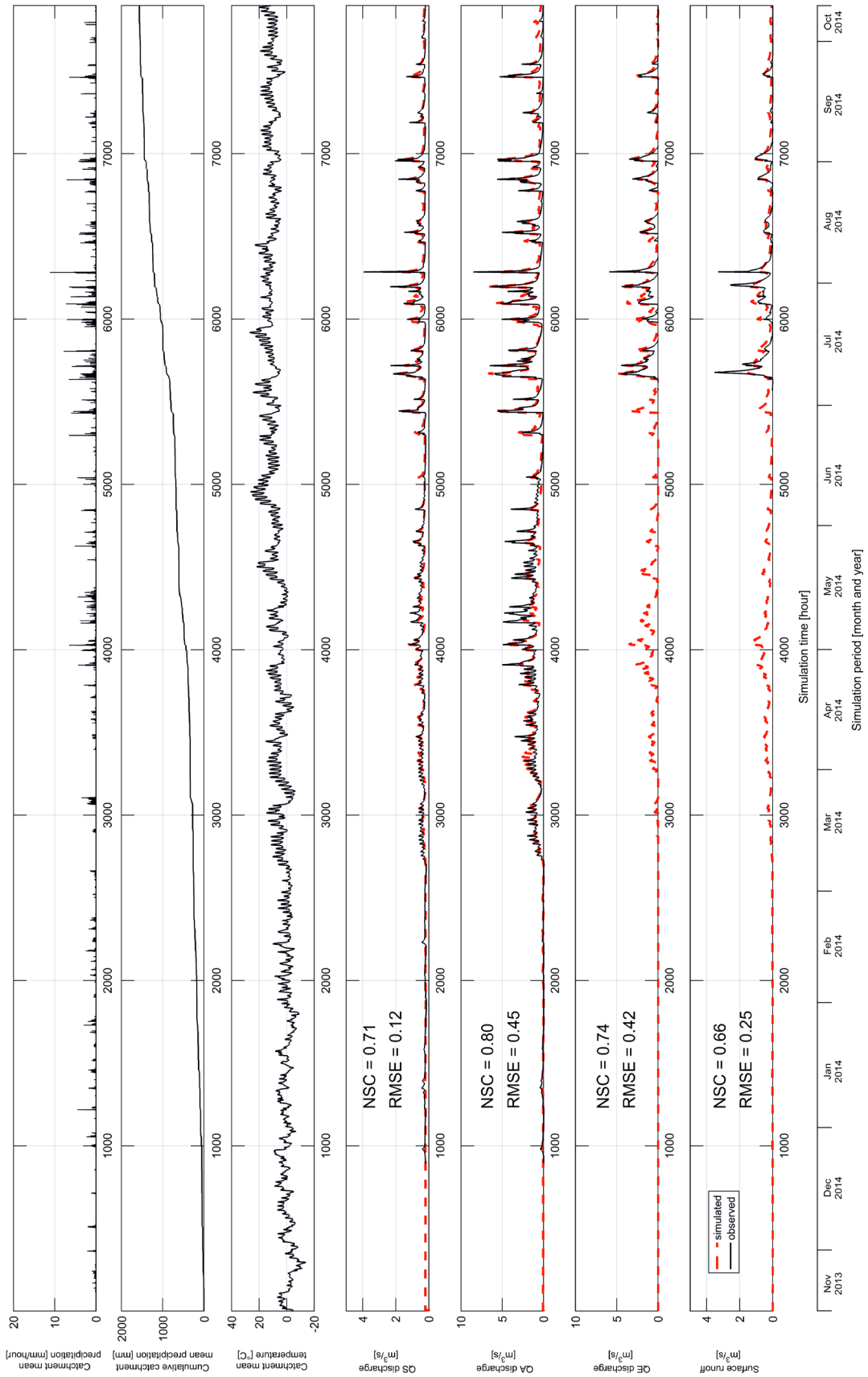
Figure 5.4: Observed and simulated discharge of four spatially-distributed model outlets QS, QA, QE and SR using the best calibrated model parameter set for the period November 2013 – October 2014. Additionally, the mean catchment precipitation and temperature for the same period are shown.

5.4.2. Estimated water fluxes and storages

For a simulation period of about 330 days, we estimated that about 5 % of the total precipitation (52.79 MCM[4]) left the catchment as evapotranspiration (2.39 MCM) (Figure 5.5). Furthermore we calculated that about 84 % of the recharge (44.02 MCM) to the karst aquifer is contributed by diffuse infiltration (36.78 MCM) over the karst area. The remaining 16 % of the recharge is contributed by the allogenic recharge (7.24 MCM); i.e. direct infiltration of the surface runoff from the non-karst area into the underground karst drainage network in the upper part of the valley. The catchment is mainly drained by the karst springs. About 20 % of the total catchment discharge (49.41 MCM) is provided by QS (10.09 MCM), 44 % by QA (21.81 MCM), 23 % by QE (11.29 MCM) and 13 % by the surface runoff (6.23 MCM).
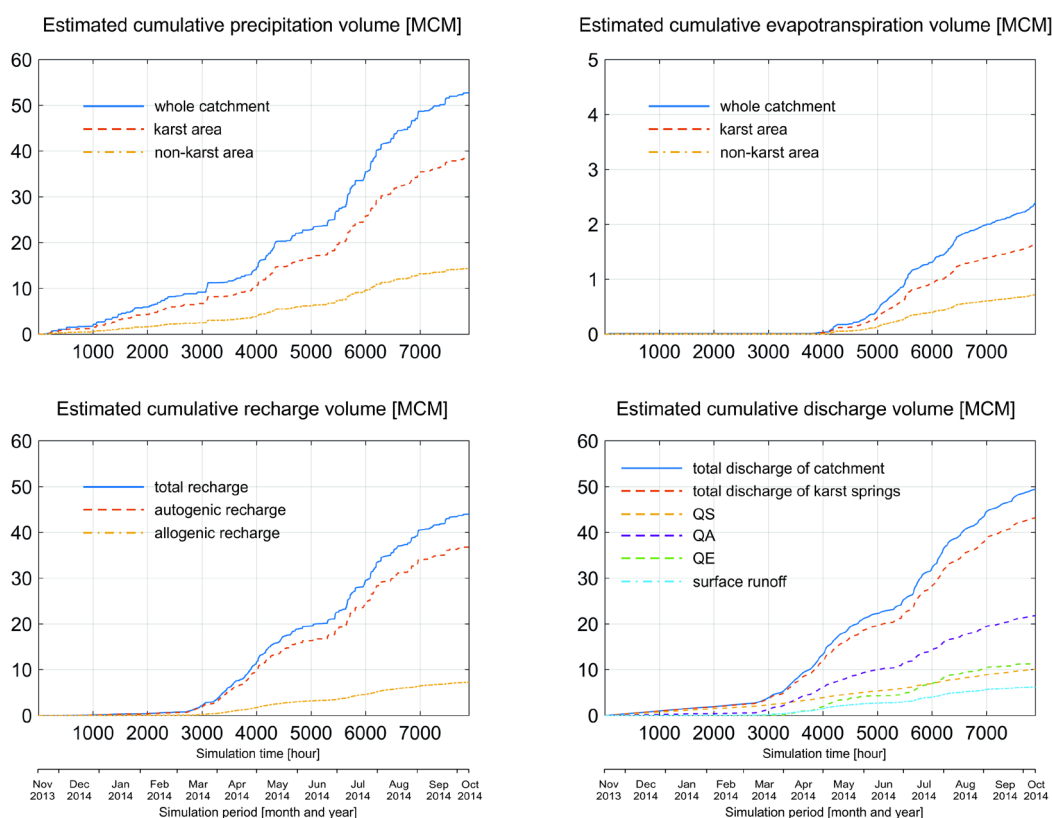
Figure 5.5: Estimated cumulative volumes of precipitation, evapotranspiration, recharge and discharge for the studied catchment for the period November 2013 – October 2014 on an hourly time step in million cubic meters (MCM).

[4] MCM for million cubic meters

We compared the estimated water storages for the whole catchment, karst area, non-karst area and karst aquifer to better understand different storage processes (snow storage, soil water storage and subsurface water storage) in the model domain (Figure 5.6). It is considered that in the simulated winter and early spring (November 2013 – March 2014), the catchment water storage is mainly characterized by snow storage in both the karst and non-karst areas. Afterwards, snow melt (April – May 2014) led to rapidly decreasing catchment snow storage, but increasing storage in the karst aquifer as subsurface water in both fast and slow paths. During the rainfall season in the simulated summer and autumn (June – October 2014), the catchment storage is mainly characterized by subsurface water storage in the karst aquifer, while during medium and high flows the water is also stored intermittently in the top layer of the non-karst area.
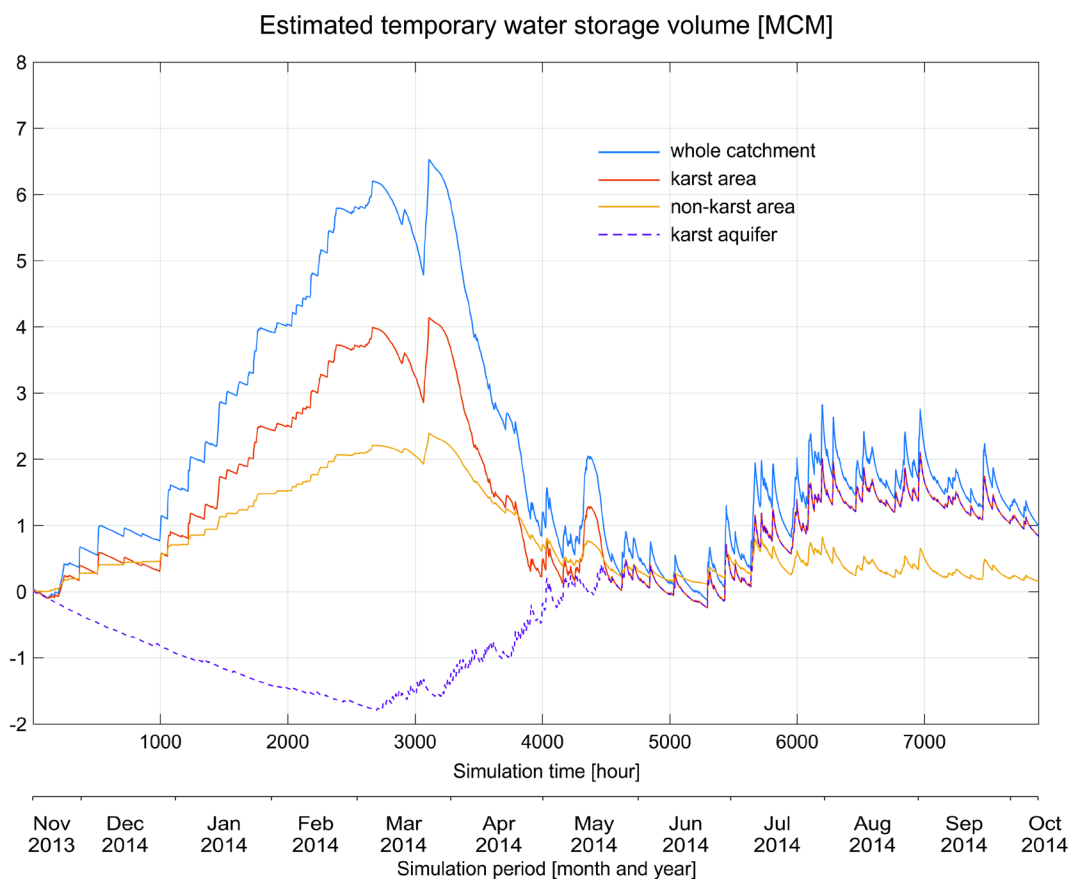
Figure 5.6: Estimated temporary water storage volumes for the whole catchment, karst area, non-karst area and karst aquifer for the period November 2013 – October 2014 on an hourly time step in million cubic meters (MCM).

5.4.3. Assessing the impact of climate projections

An overview about the change in water fluxes and storages under changing climate conditions (median climate scenarios and uncertainty of the climate scenario 2070) is given in Table 5.2.

Table 5.2a: Estimated total volume of precipitation (P), evapotranspiration (ET), recharge (R) and discharge (Q) under varied climate conditions (median climate scenarios of 2030, 2050 and 2070 as well as the uncertainty of the climate scenario of 2070) for the simulated time period of 330 days and their units are MCM.

climate condition	P	ET	R	Q
	catchment	catchment	catchment	catchment
current	52.79	2.39	44.02	49.41
2030	50.58	2.52	42.08	47.32
2050	48.48	2.66	40.15	45.33
2070	46.97	2.77	38.76	43.91
2070 max	53.15	3.34	43.74	49.33
2070 min	38.87	2.35	32.10	36.80

climate condition	Q			
	QS	QA	QE	SR
current	10.09	21.81	11.29	6.23
2030	9.88	21.35	10.26	5.83
2050	9.69	20.99	9.14	5.51
2070	9.56	20.89	8.17	5.28
2070 max	10.15	23.96	10.09	6.04
2070 min	8.80	17.70	5.27	4.28

Table 5.2b: Estimated temporary water storage volumes (S) for the whole catchment, karst area, non-karst area and karst aquifer at time step of 2665 (March) and 7896 (October) under varied climate conditions (median climate scenarios of 2030, 2050 and 2070 as well as the uncertainty of the climate scenario of 2070) and their units are MCM.

climate condition	S			
	at time step of 2665 (March)			
	whole catchment	karst area	non-karst area	karst aquifer
current	6.20	3.99	2.21	-1.77
2030	5.97	3.82	2.15	-1.70
2050	5.37	3.41	1.96	-1.58
2070	4.23	2.54	1.69	-1.38
2070 max	5.28	3.32	1.97	-0.41
2070 min	0.19	-0.10	0.28	-1.68

climate condition	S			
	at time step of 7896 (October)			
	whole catchment	karst area	non-karst area	karst aquifer
current	0.99	0.84	0.16	0.84
2030	0.73	0.58	0.15	0.58
2050	0.49	0.34	0.15	0.34
2070	0.29	0.14	0.15	0.14
2070 max	0.67	0.52	0.15	0.52
2070 min	-0.29	-0.43	0.14	-0.43

5.4.3.1. Median climate scenarios

The simulations (Figure 5.7 – 5.9) show that the water fluxes and storages are sensitive to varying climate conditions. Compared to the current situation, the precipitation over the catchment area is gradually decreasing (medians of -4.2 %, -8.2 % and -11.0 %) for the climate scenarios of 2030, 2050 and 2070, whereas the evapotranspiration is increasing (medians of +5.5 %, +11.4 % and +16.0 %). The modeled precipitation, temperature and evapotranspiration for future contribute to the decreased recharge (medians of -4.4 %, -8.8 % and -12.0 %) to the karst aquifer, whereas the recharge pattern is shifted, i.e. the recharge is increasing in winter and spring and decreasing in summer and autumn (Figure 5.7).
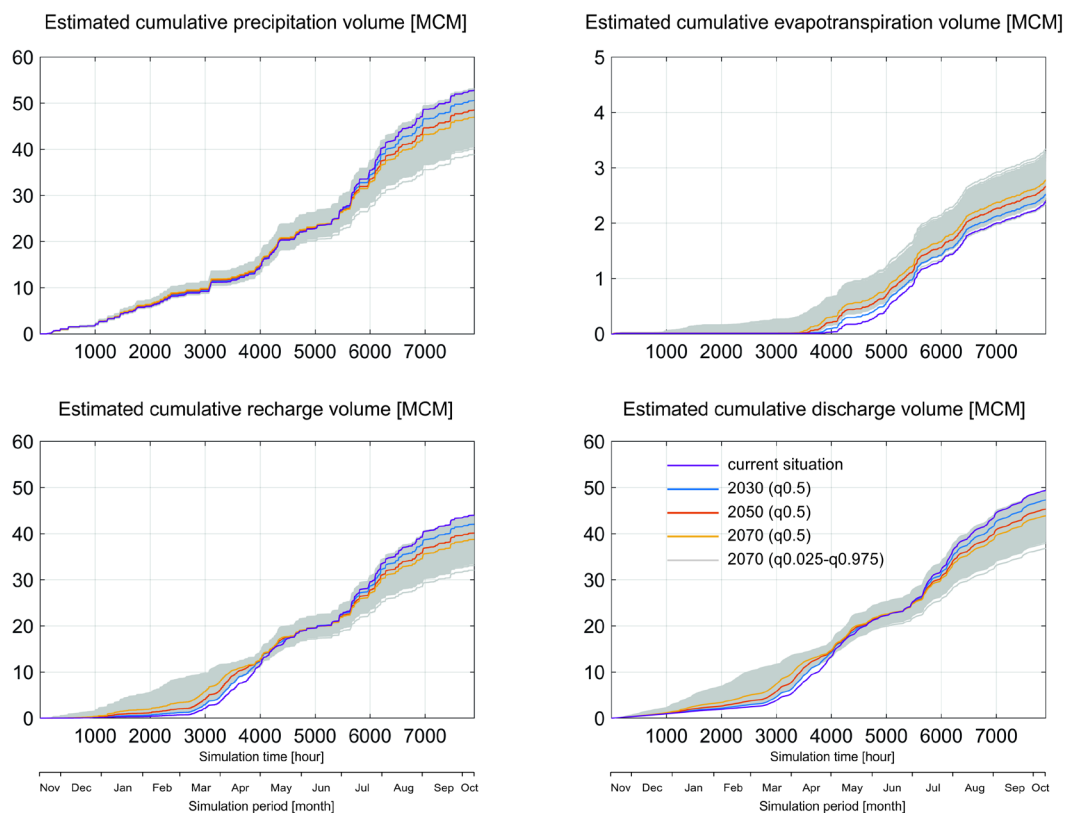
Figure 5.7: Impacts of the median climate scenarios (q0.5) for 2030, 2050 and 2070 as well as the uncertain climate scenarios (1000 random sampled combinations) for 2070 on the simulated hydrological variables (precipitation, evapotranspiration, recharge and discharge) for the studied catchment.

Furthermore, the catchment water storage pattern changes significantly, especially during the normally "cold" period (from January to April). Under the current condition, maximal 6.50 MCM water is stored in snow, whereas at the same time, only 3.27 MCM as snow storage is estimated there under the conditions of 2070 (Figure 5.8). This indicates that the simulated future climate conditions affect the snow storage massively. Comparatively, the catchment water storage during the rainfall season is much less influenced. For the karst aquifer, the shift of recharge pattern towards increased recharge in winter and spring,

and decreased recharge in summer and autumn produces compensation, i.e., the annualized balance between recharge and discharge for the karst aquifer is constant for the simulations of 2030, 2050 and 2070. Furthermore, the influence of the varied climate conditions on the intermediate water storage in the karst aquifer (epikarst and fast flow path) and top layer of the non-karst area are limited.

Our simulations (Figure 5.9) show that the catchment discharge amount varies under changing climate conditions. The total discharge of QE is decreasing gradually (medians of 9.1 %, -19.0 % and -27.6 %) for 2030, 2050 and 2070, compared to the current situation. However, the deficit for QA (medians of -2.1 %, -3.8 % and -4.2 %) and QS (medians of -2.0 %, -3.9 % and -5.2 %) is less significant. For the total surface runoff generated from the non-karst area, climate change effects are clearly perceptible with the total runoff decreasing (medians of -6.4 %, -11.4 % and -15.1 %) for 2030, 2050 and 2070. Also, the catchment discharge pattern is influenced significantly. The simulated increasingly warming winters and springs from 2030 to 2070 shift the discharge pattern of QA, QE and surface runoff continuously, while the discharge pattern of QS is quite stable until 2070.
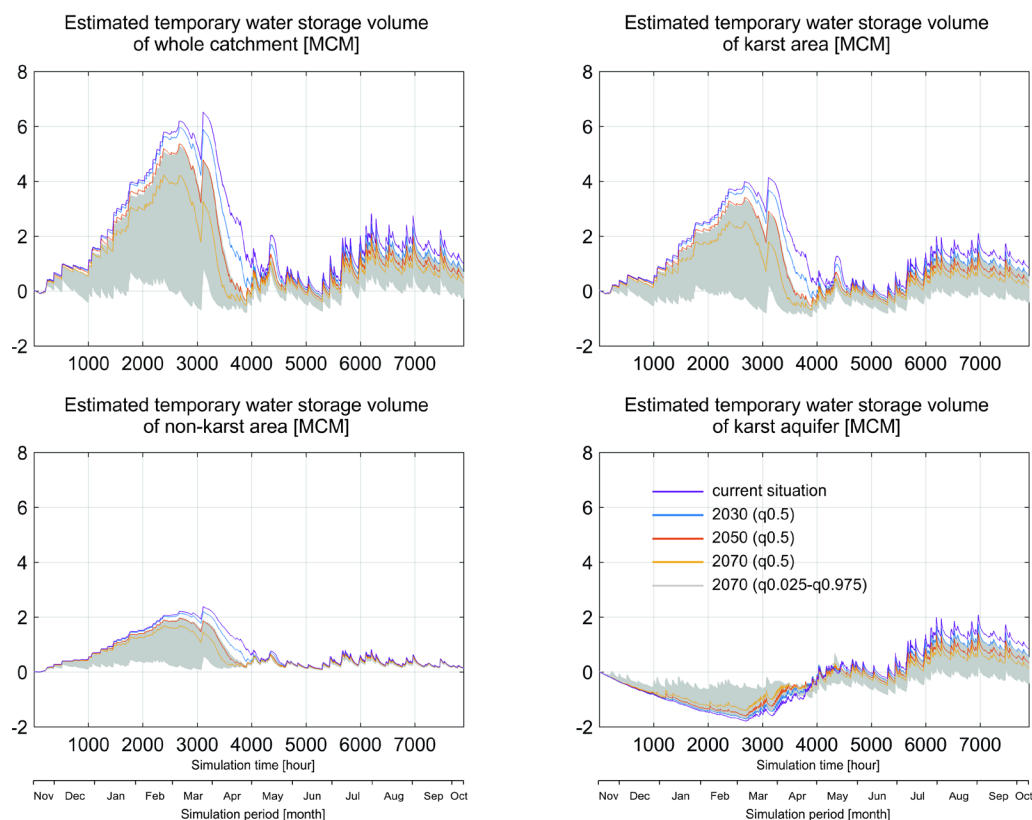
Figure 5.8: Impacts of the median climate scenarios (q0.5) for 2030, 2050 and 2070 as well as the uncertain climate scenarios (1000 random sampled combinations) for 2070 on the simulated water storages of the whole catchment, karst area, non-karst area and karst aquifer.
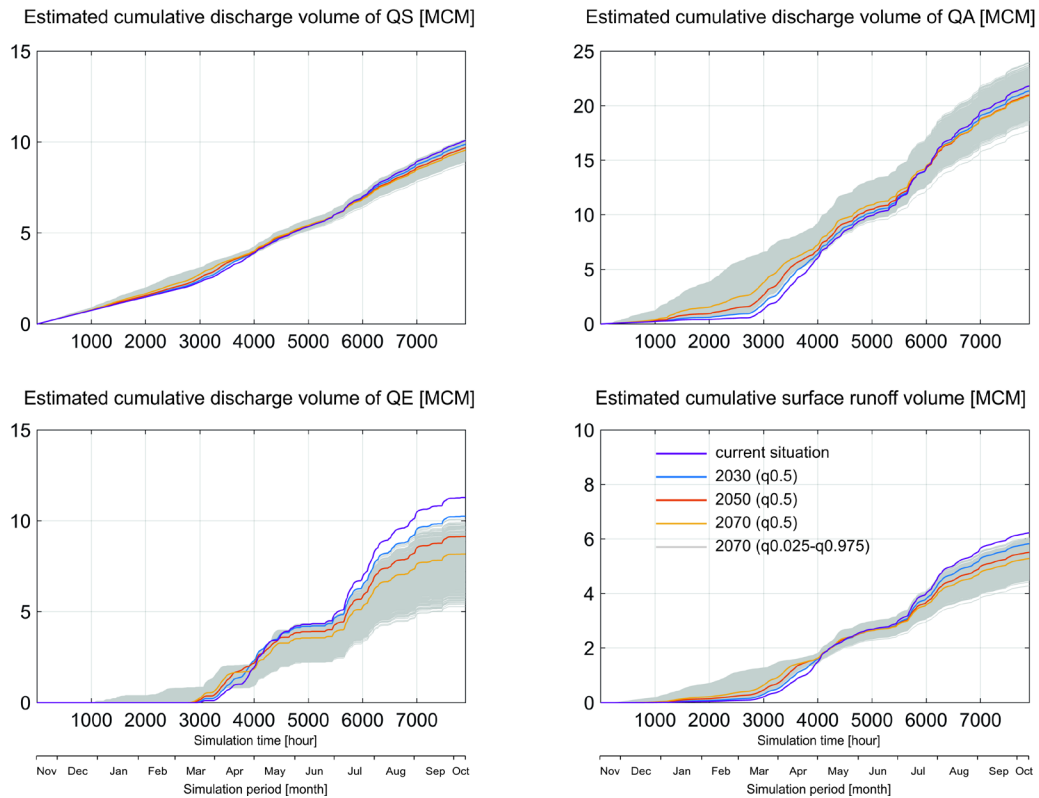
Figure 5.9: Impacts of the median climate scenarios (q0.5) for 2030, 2050 and 2070 as well as the uncertain climate scenarios (1000 random sampled combinations) for 2070 on the simulated discharge of QS, QA, QE and surface runoff from the non-karst area.

5.4.3.2. Uncertainty of the climate scenario 2070

The results show (Figure 5.7) that the impacts of the possible climate scenarios for 2070 on the precipitation, evapotranspiration, recharge and catchment discharge are uncertain. Compared to the current situation, a general trend with the decrease of precipitation, recharge and catchment discharge or with the increase of evapotranspiration can be expected. In the most extreme cases, the change of precipitation varies between -26.4 % and 0.7 %, evapotranspiration between -1.8 % and 39.6 %, recharge to the karst aquifer between -27.1 % and -0.6 % and catchment discharge between -25.5 % and -0.2 %, compared to the current situation. Furthermore, the scenario runs indicate a shift of evapotranspiration, recharge and catchment discharge pattern towards increased recharge as well as catchment discharge in winter and spring and constantly increased evapotranspiration throughout the year.

Moreover, the scenario runs indicate a clear trend with the decrease of water storages for the simulated catchment (Figure 5.8). Under the condition "extremely warm" of 2070, the snow storage of the catchment changes so dramatically that almost no water can be stored in snow during the normally "cold" period (from December to April). Simultaneously, the water storage pattern in the karst aquifer can be significantly shifted due to the earlier-

starting snow melt. Also, the water storage in the karst aquifer in summer and autumn are influenced strongly due to the significantly decreased recharge. This contributes to a clearly negative "balance" at the last time step of the simulation under the "extremely dry" conditions of 2070. If this negative water storage could be transferred to the coming year, it would cause more negative "balance" for the simulated karst aquifer based on the simulated climate condition. Accordingly, the stored water resources in the karst aquifer would be decreased significantly.

Regarding to the impacts of the uncertain scenarios on the karst spring discharges and surface runoff, distinct trends are identified (Figure 5.9): (1) a clear trend with the decrease of QE and SR, (2) impacts on QA are highly uncertain even an increase of its total discharge is projected and (3) impacts on QS are clearly less uncertain and a general trend with decrease of QS can be expected. In the most extreme cases, compared to the current situation, the change of QS varies between -25.5 % and 0.7 %, QA between -18.8 % and 9.9 %, QE between -53.3 % and -10.6 % and surface runoff between -31.3 % and -2.9 %. QS's discharge is considered as the most "robust" in the face of strongly varied climate conditions. Furthermore, a common shift of the discharge pattern of all karst springs and the surface runoff pattern are identified, i.e. increased QS, QA, QE and SR in winter and early spring.

5.5. Discussion

5.5.1. Realism of the model simulations

In this study, the karst catchment model simulates the transient and highly variable discharge behavior simultaneously at the four spatially-distributed model outlets. The evaluation using different statistical metrics indicate that the results are satisfying. The previous studies proved that the model adequately represents the high permeability flow and flooding mechanisms observed in the studied karst aquifer and is also able to transform them into realistic catchment responses during rainfall periods (Chen and Goldscheider, 2014; Chen et al., 2017). The current study shows that the snow dynamic reflected on the major karst springs (QS and QA) is reproduced in the model. It indicates that the model represents the recharge process driven by the snow accumulation and melting in the studied karst catchment. During the snow accumulation period (Nov.2013 – Feb.2014), the karst system was under-saturated, and QS discharged the whole catchment, while other karst springs (QA and QE) were dry and no significant surface runoff generated from the non-karst area. The simulation is consistent with our measurements and field observations. It indicates that the model represents the dominant flow process for the investigated karst catchment during low flow conditions. We find that the surface runoff generated from the non-karst area is much less than the effective precipitation for the non-karst area. The reason is that the allogenic recharge leads to significant loss. This model behavior represents the conceptualization of our understanding about the hydraulic connection between the karst and non-karst areas.

However, the model evaluation shows that the model did not very accurately simulate the surface runoff in response to heavy rainfall events. The reason could be that we oversimplified the complex hydrological situation in the non-karst area under-representing its runoff dynamics.

The estimated low evapotranspiration for the investigated catchment seems to be realistic. In the elevated part of the study area, no significant thickness of soil cover can be considered. Even in the extended karst area, soil cover is missing, the limestone rocks are bare, and the rainfall can directly infiltrate into the karst system through surface features, leading to a high infiltration rate for the karst aquifer (Goldscheider, 2002). However, the total amount of evapotranspiration may be underestimated, as the potential evaporation from snow cover (e.g. Leydecker and Melack, 2000) was not taken into account in our model. Accordingly, the estimated infiltration rate of 95.5 % for the karst aquifer may also be overestimated. For comparison, Malard et al. (2016) estimated average infiltration rates for mountainous karst catchments across Switzerland varying between 60 % and 90 % of total precipitation using a GIS-based approach.

5.5.2. Identifying hydrological processes sensitive to potential climate change patterns

The climate scenario runs show the water fluxes and storages within the simulated catchment are sensitive to varying climate conditions. Basically, the catchment discharge amount is precipitation driven. The discharge pattern is controlled by the temporal distribution of precipitation on the one hand, and the temperature pattern on the other hand. The snow storage in the catchment is highly sensitive to the temperature variation, which can shift the seasonal snow melting for the catchment, recharge pattern for the karst aquifer and drainage pattern of the non-karst area. The impacts of potential climate change on snow accumulation and melting processes have also been reported in other catchments across the European Alps (Horton et al., 2006; Zierl and Bugmann, 2005).

For the karst aquifer, due to its characteristic duality of flow and storage and additional spatially heterogeneous distributed drainage structure, the impacts of the varied climate conditions on QS, QA and QE are distinct. The simulations demonstrate well that QE is highly sensitive to changing climate conditions. The explanation is that QE acts as the highest overflow outlet of the studied karst aquifer, and its activation is strongly controlled by the hydrodynamic conditions in the karst drainage network, which are in turn highly sensitive to recharge and fast flow processes. In contrast, QS is the lowest outlet for the karst aquifer and its discharge is "guaranteed" by the long term water storage in matrix. Accordingly, QS is the most "robust" in the face of changing climate conditions. Under the simulated climate scenarios, QA shows a mixed character. On the one hand, QA's discharge is significantly less influenced than QE and on the other hand, QA's discharge pattern can be more easily shifted than QS. It demonstrate well that the high permeability flow in the conduit network with less water storage capacity is sensitive

to changing hydrological conditions, while the low permeability flow in the matrix with greater water storage capacity is more resistant. In the non-karst area, the varied climate conditions affect the snow accumulation and melting patterns. As the non-karst and karst areas are hydraulically connected in the upper part of valley, the predicted earlier-starting snow melt can generate more runoff in the non-karst area which partly infiltrates into the underground drainage network leading to greater loss for the surface runoff and increased allogenic recharge to the karst aquifer.

For the current analysis, we used a pragmatic approach to analyze potential climate change scenarios. The uncertainties of the climate scenarios were considered using a random sampling based approach. The final results indicate the impacts of the seasonal changes in pattern of precipitation and temperature on the spatially varied hydrological processes within the catchment. Additionally, we investigated the flow exceedance probability of karst springs and surface runoff from the non-karst area (supplementary material) and find that the simulated climate conditions affect the frequency and amplitude of catchment flows. This suggests that the impacts of the temporally stochastic distributions of meteorological parameters and their variability on the catchment flow dynamics should be systematically investigated.

5.6. Conclusions

The current work presents an investigation of the water fluxes and storages in a high-elevation Alpine catchment. We extended the existing karst catchment model developed by Chen & Goldscheider (2014) to consider spatially-distributed snow dynamics and complex surface and subsurface heterogeneous drainage structures. The new model is able to simultaneously simulate the transient and highly variable discharge behavior of four spatially-distributed model outlets at an hourly time step. Furthermore, we estimated the water fluxes and storages within the model domain. The results demonstrate that the spatiotemporal distribution of water fluxes and storages is controlled by the surface and subsurface hydrological setting. We find a large portion of precipitation infiltrates in the karst aquifer as autogenic recharge and contributes to surface runoff in the adjacent non-karst area, which can partly infiltrate into the karst aquifer as allogenic point recharge. In the simulation period, the catchment is mainly drained by the karst springs, about 20 % of the total catchment discharge is provided by the permanent spring QS, 44 % by the overflow spring QA, 23 % by the estavelle QE and 13 % by the surface runoff SR generated from the non-karst area. In the simulated winter and early spring (November 2013 – March 2014), the catchment water storage is mainly characterized by the snow storage both in the karst and non-karst areas. During the rainfall season in the simulated summer and autumn (June – October 2014), the catchment storage is mainly characterized by the subsurface water storage in the karst aquifer.

Additionally, we studied the impacts of potential climate change patterns on the spatially varied surface and subsurface hydrological processes in the model using a delta approach

combined with a random sampling technique. The scenario runs demonstrate that the varied climate conditions affect the spatiotemporal distribution of water fluxes and storages within the catchment significantly: (1) the total catchment discharge decreases under all evaluated future climate conditions. (2) The catchment snow storage during normally "cold" period from December to April decreases significantly, while the autogenic and allogenic recharge to the karst aquifer increase. (3) In the karst aquifer, due to its storage capacity, the shift of recharge pattern towards increased recharge in winter and spring, and decreased recharge in summer and autumn offset each other under the varied climate conditions. (4) The impacts of the potential future climate conditions on the karst springs are distinct. The permanent spring QS presents a "robust" discharge behavior, while the estavelle QE is highly sensitive to the changing climate conditions. QA's discharge is significantly less influenced than QE and its discharge pattern can be more easily shifted than QS. This demonstrates well that the impacts of potential climate change on the subsurface flow dynamics are regulated by the karst aquifer due to its characteristic dual flow systems and spatially heterogeneous distributed drainage structure.

As our climate scenario projections use a simple delta approach, the impact of temporally stochastic distributions of meteorological parameters and their variability could not be investigated in this study. Accordingly, the results should only be applied to understand the relationship between the hydrological processes within the studied catchment and potential climate change patterns. It would be interesting to use more realistic data, i.e. the precipitation and temperature time series downscaled from regional climate models to investigate their impact on the spatially-distributed water fluxes and storages. But we warn that the measurements of meteorological variables in high-elevation mountainous environment have large quite uncertainty. These uncertainties may have an impact on the model simulations and the understanding of derived processes.

Acknowledgments

Supplementary material

Table S5.1: Summary of calibrated model parameters.

model domain	model parameter	model location	description	unit	parameter range lower	parameter range upper	final calibrated parameter set
snow storage	x_1	sub. 1-29	threshold temperature	°C	0.00	6.00	1.95
	x_2	sub. 1-29	degree day factor	mm h^{-1} °C^{-1}	0.00	0.10	0.00
	x_3	sub. 1-29	refreezing factor	-	0.00	0.50	0.37
	x_4	sub. 1-29	water holding capacity	-	0.00	0.50	0.00
	x_5	sub. 1-29	radiation coefficient	-	0.0002	0.0006	0.0002
unsaturated zone	x_6	sub. 1-5	infiltration threshold	mm	0.00	0.50	0.26
	x_7	sub. 6-10			0.00	0.50	0.38
	x_8	sub. 11-15			0.00	0.50	0.29
	x_9	sub. 16-20			0.00	0.50	0.40
	x_{10}	sub. 21-29			0.00	0.50	0.50
	x_{11}	sub. 1-5	proportion of recharge	%	0.60	1.00	0.60
	x_{12}	sub. 6-10	distributed into fast flow		0.60	1.00	1.00
	x_{13}	sub. 11-15	reservoir		0.60	1.00	0.64
	x_{14}	sub. 16-20			0.60	1.00	0.67
	x_{15}	sub. 1-5	effective flow width for	m	100	1500	959
	x_{16}	sub. 6-10	fast flow / surface runoff		100	1500	1500
	x_{17}	sub. 11-15	reservoir		100	1500	1008
	x_{18}	sub. 16-20			100	1500	421
	x_{19}	sub. 21-29			100	1500	100
drainage network	x_{20}	sub. 1-20	initial base flow	m^3/s	0.26	0.40	0.40
	x_{21}	N1	junction elevation	m asl	1430	1450	1446
	x_{22}	N2			1300	1320	1300
	x_{23}	N3			1280	1300	1280
	x_{24}	N4			1270	1290	1270
	x_{25}	N5			1240	1260	1240
	x_{26}	N6			1210	1230	1210
	x_{27}	N7			1120	1130	1127
	x_{28}	N8			1105	1115	1105
	x_{29}	N9			1095	1105	1098
	x_{30}	N10			1020	1035	1028
	x_{31}	C1-C5	conduit diameter	m	2.00	4.00	2.88
	x_{32}	C6-C10			2.00	4.00	2.00
	x_{33}	C11-C15			2.00	4.00	2.81
	x_{34}	C16-C20			2.00	4.00	4.00
	x_{35}	C21			2.00	4.00	2.71
	x_{36}	C22			2.00	4.00	3.95
	x_{37}	C23			2.00	4.00	4.00
	x_{38}	C24			2.00	4.00	4.00

model domain	model parameter	model location	description	unit	parameter range lower	parameter range upper	final calibrated parameter set
drainage network	x_{39}	C25	conduit diameter	m	2.00	4.00	3.46
	x_{40}	C26			2.00	4.00	2.53
	x_{41}	C27			0.60	1.00	0.86
	x_{42}	C28			2.00	4.00	3.77
	x_{43}	C29			0.60	1.00	0.76
	x_{44}	C30			2.00	4.00	2.92
	x_{45}	C31			2.00	4.00	2.00
	x_{46}	C32			2.00	4.00	2.51
	x_{47}	C33			2.00	4.00	2.97
	x_{48}	C34			0.20	2.00	0.51
	x_{49}	C35			0.20	2.00	0.85
	x_{50}	C36			0.20	2.00	0.20
	x_{51}	C37			0.20	2.00	2.00
	x_{52}	C38			0.20	2.00	0.21
	x_{53}	C1-C5	conduit roughness	mm	10	2000	1189
	x_{54}	C6-C10			10	2000	2000
	x_{55}	C11-C15			10	2000	1134
	x_{56}	C16-C20			10	2000	263
	x_{57}	C21			10	2000	1397
	x_{58}	C22			10	2000	1011
	x_{59}	C23			10	2000	10
	x_{60}	C24			10	2000	1661
	x_{61}	C25			10	2000	1304
	x_{62}	C26			10	2000	756
	x_{63}	C27			10	2000	1450
	x_{64}	C28			10	2000	752
	x_{65}	C29			10	2000	1782
	x_{66}	C30			10	2000	1797
	x_{67}	C31			10	2000	1577
	x_{68}	C32			10	2000	2000
	x_{69}	C33			10	2000	967
	x_{70}	C34			10	2000	274
	x_{71}	C35			10	2000	10
	x_{72}	C36			10	2000	1273
	x_{73}	C37			10	2000	1753
	x_{74}	C38			10	2000	1451
	x_{75}	Sc1-Sc5	open channel	-	0.01	0.20	0.03
	x_{76}	Sc6-Sc11	roughness coefficient		0.01	0.20	0.08
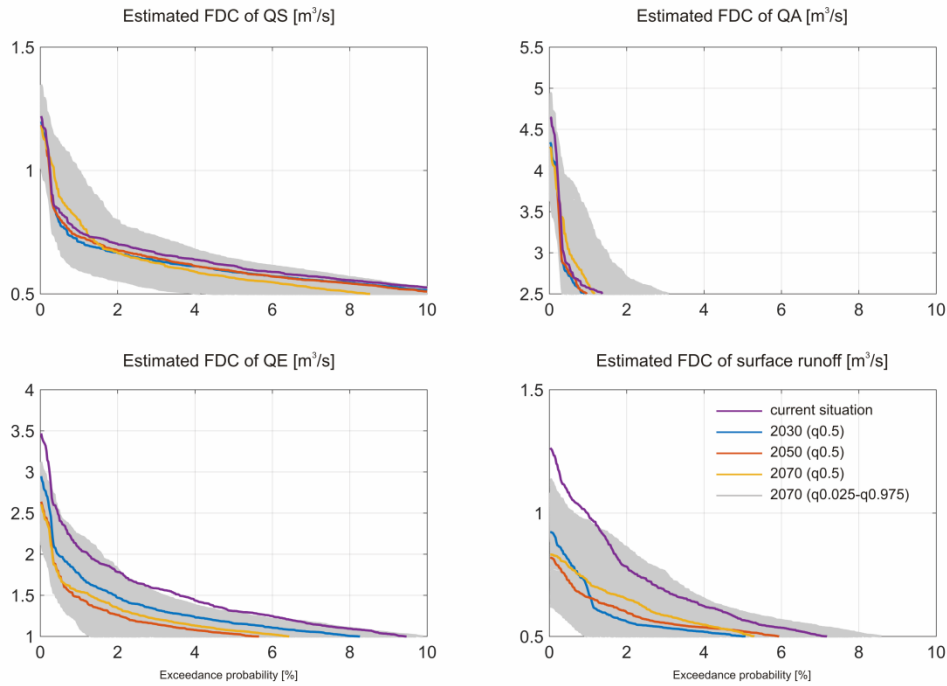
Figure S5.1: Impacts of the median climate scenarios (q0.5) for 2030, 2050 and 2070 as well as the uncertain climate scenarios (1000 random sampled combinations) for 2070 on the FDC (0 % – 10 % exceedance probability) of QS, QA, QE and surface runoff from the non-karst area for the time window from December to March.
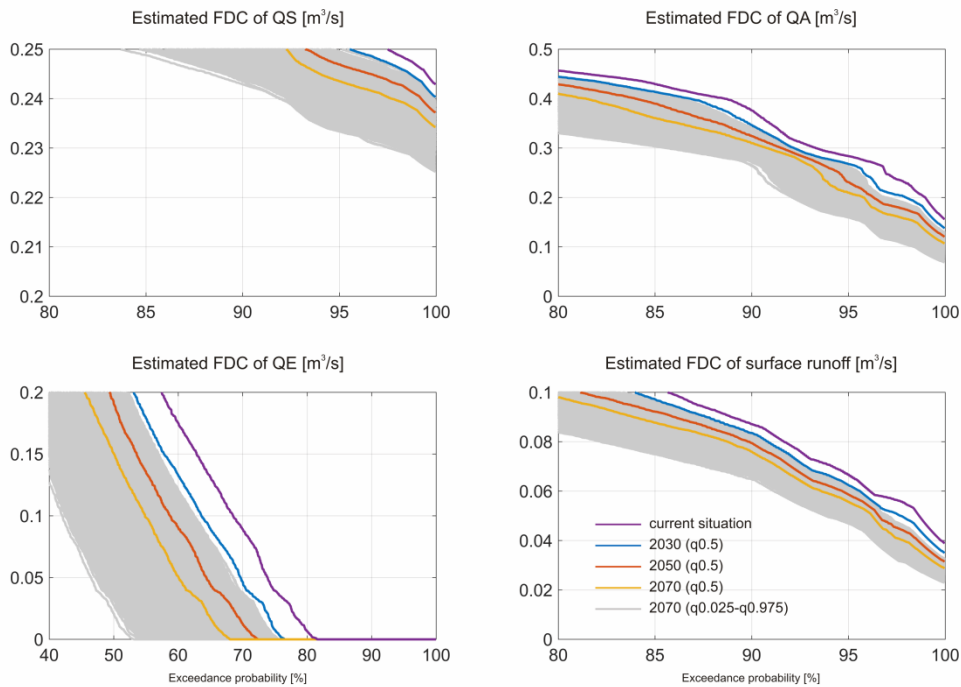
Figure S5.2: Impacts of the median climate scenarios (q0.5) for 2030, 2050 and 2070 as well as the uncertain climate scenarios (1000 random sampled combinations) for 2070 on the FDC (80 % – 100 % exceedance probability) of QS, QA, QE and surface runoff from the non-karst area for the time window from June to October.

Chapter 6

Synthesis

6.1. Conclusions

In order to obtain a better global overview of karst aquifers, a world karst aquifer map was prepared at a consistent working scale of 1:10 million and differentiates between areas of "continuous carbonate rocks" (typically > 65 % carbonate rock outcrops) and "discontinuous carbonate rocks" (typically 15 – 65 % outcrops). The updip boundaries of non-exposed karst aquifers were also delineated. The map and associated database include selected karst springs, wells and other freshwater abstraction structures, and selected caves. The proposed mapping concepts were tested, refined and proved for Europe. Prior estimates, that carbonate rock outcrops cover 35 % of Europe, were found to be overestimated. The draft karst aquifer map of Europe shows that about 21.6 % of the European land surface is characterized by the presence of carbonate rock, including 15.2 % of "continuous" and 6.4 % of "discontinuous carbonate rocks". The total area of actual carbonate rock outcrops is about 13.8 %. Much of this occurs beneath some of the continent's most densely populated regions where effective water resources management is especially critical, such as England, northern and southern France, parts of Germany, central Italy, and eastern Spain.

Subsequently, this study focused on an Alpine karst system, which is characterized by complex geology and underground conduit drainage network. A numerical model was developed step-by-step (Chapter 3 and 5) to simulate the surface and subsurface heterogeneous drainage processes within the studied catchment. The model contains a hybrid-structure (combining lumped and distributed model) and incorporates the karst and non-karst areas, which are hydraulically connected. A lumped model represents the main hydrological processes of the unsaturated zone in the karst area and the top layer of the low permeable rocks in the non-karst area. The lumped model is coupled with a distributed model representing the drainage conduit network in the karst area and surface stream channels in the non-karst area. Additionally, spatially-distributed meteorological variables and their driven snow accumulation/melting dynamic are considered in the simulated catchment. The simulation results demonstrate that the model is able to simulate simultaneously the transient and highly variable discharge behavior of four spatially-distributed model outlets at an hourly time step, which represent the karst springs at different elevations (a permanent spring, an overflow spring and an estavelle) and surface runoff generated from the non-karst area. Furthermore, the dual flow regime and transient hydrodynamic behavior of phreatic and epiphreatic conduits in the karst aquifer are demonstrated in the simulation.

Furthermore, a novel multi-step sensitivity analysis approach was developed and performed (Chapter 4) for the model part representing the karst aquifer. The results demonstrate that the identified spatiotemporally-varied drainage pattern is caused mainly by dynamics of high permeability flow in individual karst sub-catchments and flooding mechanisms in major conduit networks: (1) during and immediately after rainfall events, concentrated infiltration in the epikarst and rapid flow in the vadose zone from individual karst sub-catchments strongly influence the discharge dynamics of individual outlets. (2) After rainfall events, the influence of diffuse flow components in karst sub-catchments on system discharge is increased and the spatial contribution pattern of karst sub-catchments to the discharge behavior of individual outlets changed from "focused" to "distributed". (3) The basic system discharge behavior during dry periods is predominantly controlled by the drainage mechanism in the hydraulically-connected conduits system in the lower part of the valley. This valuable knowledge confirms that the tested model represents the conceptualization of our understanding of the relevant flow processes observed in the studied karst system and is able to transform them into realistic catchment responses. Moreover, the interactions between model parameters were quantified. The results demonstrate that the model is nonlinear and the influential parameters are highly correlated in the model space and time domain. The influence of parameter constraints on spatially-varying parameter sensitivity and interactions was assessed by performing complete sensitivity analysis for prior and posterior parameter ranges. The sensitivity calculated based on different parameter bounds was compared and the results demonstrate that the spatial patterns of identified parameter sensitivity and interactions are strongly influenced by the used parameter bounds.

Finally, this study investigated the water fluxes and storages within the investigated catchment under historical and potential future climate conditions. The model simulation under current condition demonstrates that a large portion of precipitation infiltrates in the karst aquifer as autogenic recharge and contributes to surface runoff in the adjacent non-karst area, which can partly infiltrate into the karst aquifer as allogenic point recharge. In the simulation period, the catchment is mainly drained by the karst springs, about 20 % of the total catchment discharge is provided by the permanent spring QS, 44 % by the overflow spring QA, 23 % by the estavelle QE and 13 % by the surface runoff SR generated from the non-karst area. Our simulations indicate that snow storage is dominant from November to April, while subsurface water storage in the karst aquifer dominates from May to October. Additionally, a delta approach combined with random sampling technique was used to assess the potential impacts of climate changes. The scenario runs demonstrate that the varied climate conditions affect the spatiotemporal distribution of water fluxes and storages within the catchment significantly: (1) the total catchment discharge decreases under all evaluated future climate conditions. (2) The catchment snow storage capacity during normally "cold" period from December to April decreases significantly under future climate conditions, while the autogenic and allogenic recharge to the karst aquifer increases. (3) In the karst aquifer, due to its storage capacity, the shift of recharge pattern towards increased recharge in winter and spring, and decreased

recharge in summer and autumn produce compensation under the varied climate conditions. (4) The impacts of the potential future climate conditions on the karst springs are distinct. The permanent spring QS presents a "robust" discharge behavior, while the estavelle QE is highly sensitive to the changing climate conditions. QA's discharge amount is significantly less influenced than QE and its discharge pattern can be more easily shifted than QS. It demonstrate well that the impacts of potential climate change on the subsurface flow dynamics are regulated by the karst aquifer due to its characteristic dual flow systems and spatially heterogeneous distributed drainage structure.

6.2. Perspective and outlook

- **Completion of the global karst aquifer mapping**

In this study, the mapping procedure is tested, refined and proved for Europe. Further study should extend the mapping for the whole world, as well as the collection of spring and cave data. For future research, the map should be combined with other relevant information, such as climate and global change, agriculture and irrigation, population density and water demand, or biodiversity. The GIS based database of the global karst aquifer map can be used for large scale hydrological modeling.

- **Refining the previous hydrogeological conceptual model**

Natural tracers (e.g. stable isotope) are recommended to be used to assess groundwater transit-time distribution and flow components in the studied karst system to refine the previous hydrogeological conceptual model.

- **Improved hydrological monitoring**

A hydrological monitoring system for the upper part of the Schwarzwasser valley should be established. The continuous discharge measurements can be used to better characterize the hydrological functioning of the non-karst area and the rockfall mass and their interaction with the karst drainage conduit network in underground. Moreover, the area covered radar data calibrated with ground weather station measurements are suggested to be used as model input variables to reduce precipitation data uncertainty.

- **Studying conduit-matrix interaction**

The previous work by Goldscheider (2005) indicates a clear conduit-matrix interaction in the studied karst aquifer. Further study can be proposed to use the hybrid modeling approach combing discrete conduit network and single continuum porous medium model (e.g. Reimann et al., 2011) to investigate the significance of the conduit-matrix interaction in saturated zone.

- **Coupling distributed karst catchment model and regional climate model**

Since the climate scenario projection is done by using the pragmatic delta approach, the impact of temporally stochastic distributions of meteorological parameters and their variability cannot be investigated. Therefore, precipitation and temperature time series downscaled from regional climate models are strongly advised to be used to study their impacts on the dynamics of the water fluxes and storages within the studied catchment (e.g. Kunstmann et al., 2004).

- **Coupling distributed karst catchment model and regional climate model**

Acknowledgements

This work was made possible with the help and support of many people. I would like to thank…

Declaration of Authorship

Study 1 (Chapter 2):
Citation: Zhao Chen, Augusto Auler, Michel Bakalowicz, David Drew, Franziska Griger, Jens Hartmann, Guanghui Jiang, Nils Moosdorf, Andrea Richts, Zoran Stevanovic, George Veni, Nico Goldscheider, The World Karst Aquifer Mapping project: concept, mapping procedure and map of Europe, Hydrogeology Journal, 2017, doi: 10.1007/s10040-016-1519-3.

Declaration of authorship: All authors developed the mapping approach together. Augusto Auler, Michel Bakalowicz, David Drew, Guanghui Jiang, Zoran Stevanovic and George Veni (GV) collected the spring and cave data. Jens Hartmann and Nils Moosdorf provided the GLiM database and technical support. Zhao Chen (ZC) processed the mapping with assistance of Franziska Griger and in consultation with Nico Goldscheider (NG). ZC executed the GIS analysis and obtained all results in consultation with NG. NG, ZC and GV wrote the manuscript. The final manuscript was reviewed by all authors.

Study 2 (Chapter 3):
Citation: Zhao Chen, Nico Goldscheider, Modeling spatially and temporally varied hydraulic behavior of a folded karst system with dominant conduit drainage at catchment scale, Hochifen-Gottesacker, Alps, Journal of Hydrology, 514: 41-52, 2014, doi: 10.1016/j.jhydrol.2014.04.005.

Declaration of authorship: Zhao Chen (ZC) developed the method and obtained all results in consultation with Nico Goldscheider (NG). ZC wrote the manuscript. The final manuscript was reviewed by NG.

Study 3 (Chapter 4):
Citation: Zhao Chen, Andreas Hartmann, Nico Goldscheider, A new approach to evaluate spatiotemporal dynamics of controlling parameters in distributed environmental models, Environmental Modelling and Software, 87: 1-16, 2017, doi: 10.1016/j.envsoft.2016.10.005.

Declaration of authorship: Zhao Chen (ZC) developed the method and obtained all results in consultation with Andreas Hartmann and Nico Goldscheider. ZC wrote the manuscript. The final manuscript was reviewed by all authors.

Study 4 (Chapter 5):
Citation: Zhao Chen, Andreas Hartmann, Thorsten Wagener, Nico Goldscheider, Dynamics of water fluxes and storages in an Alpine karst catchment under current and potential future climate conditions, Hydrology and Earth System Sciences Discussions, 2017, doi: 10.5194/hess-2017-216.

Declaration of authorship: Zhao Chen (ZC) developed the method and obtained all results in consultation with Andreas Hartmann, Thorsten Wagener and Nico Goldscheider. ZC wrote the manuscript. The final manuscript was reviewed by all authors.

References

Abbaspour, K.C., Yang, J., Maximov, I., Siber, R., Bogner, K., Mieleitner, J., Zobrist, J., Srinivasan, R., 2007. Modelling hydrology and water quality in the pre-alpine/alpine Thur watershed using SWAT. Journal of Hydrology 333 (2-4), 413-430.

Achleitner, S., Rinderer, M., Kirnbauer, R., 2009. Hydrological modeling in alpine catchments: sensing the critical parameters towards an efficient model calibration. Water Science & Technology 60 (6), 1507-1514.

Ahrends, H., Mast, M., Rodgers, C., Kunstmann, H., 2008. Coupled hydrological–economic modelling for optimised irrigated cultivation in a semi-arid catchment of West Africa. Environmental Modelling & Software 23 (4), 385-395.

Al-Charideh, A., 2012. Recharge rate estimation in the Mountain karst aquifer system of Figeh spring, Syria. Environmental Earth Sciences 65, 1169-1178.

Almeida, C., Silva, M. L., Crispim, J. A., 1995. National Report for Portugal. In: Final report COST action 65, Hydrogeological aspects of groundwater protection in karstic areas, 211-220.

Andrew, R.M., Dymond, J.R., 2007. A distributed model of water balance in the Motueka catchment, New Zealand. Environmental Modelling & Software 22 (10), 1519-1528.

Archer, G., Saltelli, A., Sobol, I.M., 1997. Sensitivity measures, anova-like Techniques and the use of bootstrap. Journal of Statistical Computation and Simulation 58 (2), 99-120.

Asrat, A., 2015. Geology, geomorphology, geodiversity and geoconservation of the Sof Omar Cave System, Southeastern Ethiopia. Journal of African Earth Sciences 108, 47-63.

Ayala-Carcedo, F.J., 1986. Mapa del karst de España, Instituto Geológico y Minero de España, Madrid.

Bakalowicz, M., 2005. Karst groundwater: a challenge for new resources. Hydrogeology Journal 13, 148-160.

Beccaletto, L., Hanot, F., Serrano, O., Marc, S., 2011. Overview of the subsurface structural pattern of the Paris Basin (France): Insights from the reprocessing and interpretation of regional seismic lines.

Benischke, R., Harum, T., Reszler, C., Saccon, P., Ortner, G., Ruch, C., 2010. Karstentwässerung im Kaisergebirge (Tirol, Österreich) – Abgrenzung hydrographischer Einzugsgebiete durch Kombination hydrogeologischer Untersuchungen mit Isotopenmethoden und hydrologischer Modellierung. Grundwasser 15 (1), 43-57.

Bergström, S., 1975. The development of a snow routine for the HBV-2 model. Hydrology Research (6(2)), 73-92.

Beron, P., Daaliev, T., Jalov, A., 2006. Caves and Speleology in Bulgaria, PenSoft, Bulgarian Federation of Speleology and National Museum of Natural History, Sofia, Bulgaria.

Birk, S., Geyer, T., Liedl, R., Sauter, M., 2005. Process-based interpretation of tracer tests in carbonate aquifers. Ground Water 43 (3), 381-388.

Bonacci, O., 1987. Karst Hydrology with special references to the Dinaric Karst. Springer, Berlin - Heidelberg.

Braun, L.N., Renner, C.B., 1992. Application of a conceptual runoff model in different physiographic regions of Switzerland. Hydrological Sciences Journal 37 (3), 217-231.

Butler, M.P., Reed, P.M., Fisher-Vanden, K., Keller, K., Wagener, T., 2014. Identifying parametric controls and dependencies in integrated assessment models using global sensitivity analysis. Environmental Modelling & Software 59, 10-29.

Butscher, C., Huggenberger, P., 2008. Intrinsic vulnerability assessment in karst areas: A numerical modeling approach. Water Resources Research 44 (3), W03408.

Campbell, C., Sullivan, S.M., 2002. Simulating time-varying cave flow and water levels using the Storm Water Management Model. Engineering Geology 65 (2-3), 133-139.

Chen, Z., Goldscheider, N., 2014. Modeling spatially and temporally varied hydraulic behavior of a folded karst system with dominant conduit drainage at catchment scale, Hochifen-Gottesacker, Alps. Journal of Hydrology 514, 41-52.

Chen, Z., Hartmann, A., Goldscheider, N., 2017. A new approach to evaluate spatiotemporal dynamics of controlling parameters in distributed environmental models. Environmental Modelling & Software 87, 1-16.

Confalonieri, R., Bellocchi, G., Tarantola, S., Acutis, M., Donatelli, M., Genovese, G., 2010. Sensitivity analysis of the rice model WARM in Europe: Exploring the effects of different locations, climates and methods of analysis on model sensitivity to crop parameters. Environmental Modelling & Software 25 (4), 479-488.

Christiaens, K., Feyen, J., 2002. Use of sensitivity and uncertainty measures in distributed hydrological modeling with an application to the MIKE SHE model. Water Resources Research 38 (9).

COST Action 65 (1995) Karst groundwater protection. Final report. European Commission, Report EUR 16547.

Courbon, P. (1989) Atlas of the great caves of the world. St. Louis, Cave Books.

Dandy, G.C., Simpson, A.R., Murphy, L.J., 1996. An Improved Genetic Algorithm for Pipe Network Optimization. Water Resources Research 32 (2), 449-458.

Dershowitz, W., La Pointe, P., Doe, T., 2004. Advances in discrete fracture network modelling., in: Proceedings of the U.S. EPA/NGWA Fractured Rock Conference, 882-894.

Dobler, C., Bürger, G., Stötter, J., 2012. Assessment of climate change impacts on flood hazard potential in the Alpine Lech watershed. Journal of Hydrology 460-461, 29-39.

Dobler, C., Bürger, G., Stötter, J., 2013. Simulating future precipitation extremes in a complex Alpine catchment. Natural Hazards and Earth System Sciences 13 (2), 263-277.

Doherty, J., 2004. PEST-Model Independent Parameter Estimation User Manual. Watermark Numerical Computing, Brisbane, Australia.

Doummar, J., Sauter, M., Geyer, T., 2012. Simulation of flow processes in a large scale karst system with an integrated catchment model (Mike She) – Identification of relevant parameters influencing spring discharge. Journal of Hydrology 426-427, 112-123.

Duscher, K., Gunther, A., Richts, A., Clos, P., Philipp, U., Struckmeier, W., 2015. The GIS layers of the "International Hydrogeological Map of Europe 1:1,500,000" in a vector format. Hydrogeology Journal 23, 1867-1875.

Drew, D., Hötzl, H., 1999. Karst Hydrogeology and Human Activities. Impacts, Consequences and Implications. - International Contributions to Hydrogeology (IAH). Balkema, Rotterdam, Brookfield.

DVWK, 1996. Ermittlung der Verdunstung von Land- und Wasserflächen. Wirtschafts- und Verl.-Ges. Gas und Wasser, Bonn.

Fang, T., Ball, J.E., 2007. Evaluation of spatially variable control parameters in a complex catchment modelling system: a genetic algorithm application. Journal of Hydroinformatics 9 (3), 163.

Fazal, M.A., Imaizumi, M., Ishida, S., Kawachi, T., Tsuchihara, T., 2005. Estimating groundwater recharge using the SMAR conceptual model calibrated by genetic algorithm. Journal of Hydrology 303 (1-4), 56-78.

Finger, D., Hugentobler, A., Huss, M., Voinesco, A., Wernli, H., Fischer, D., Weber, E., Jeannin, P.-Y., Kauzlaric, M., Wirz, A., Vennemann, T., Hüsler, F., Schädler, B., Weingartner, R., 2013. Identification of glacial meltwater runoff in a karstic environment and its implication for present and future water availability. Hydrology and Earth System Sciences 17 (8), 3261-3277.

Fisher, P., Abrahart, R., Herbinger, W., 1997. THE SENSITIVITY OF TWO DISTRIBUTED NON-POINT SOURCE POLLUTION MODELS TO THE SPATIAL ARRANGEMENT OF THE LANDSCAPE. Hydrological Processes 11 (3), 241-252.

Fleury, P., Plagnes, V., Bakalowicz, M., 2007. Modelling of the functioning of karst aquifers with a reservoir model: Application to Fontaine de Vaucluse (South of France). Journal of Hydrology 345 (1-2), 38-49.

Ford, D., Williams, D.W., 1989. Karst Geomorphology and Hydrology. Unwin Hyman, Boston.

Ford, D., Williams, P., 2007. Karst hydrogeology and geomorphology. Wiley.

Frei, C., 2004. Die Klimazukunft der Schweiz - Eine probabilistische Projektion. http://www.occc.ch/Products/CH2050/CH2050-Scenarien.pdf.

Gamerith, V., Neumann, M.B., Muschalla, D., 2013. Applying global sensitivity analysis to the modelling of flow and water quality in sewers. Water Research 47 (13), 4600-4611.

Ghasemizadeh, R., Hellweger, F., Butscher, C., Padilla, I., Vesper, D., Field, M., Alshawabkeh, A., 2012. Review: Groundwater flow and transport modeling of karst aquifers, with particular reference to the North Coast Limestone aquifer system of Puerto Rico. Groundwater flow and transport modeling of karst aquifers, with particular reference to the North Coast Limestone aquifer system of Puerto Rico. Hydrogeology Journal 20 (8), 1441-1461.

Ghasemizadeh, R., Yu, X., Butscher, C., Hellweger, F., Padilla, I., Alshawabkeh, A., 2015. Equivalent Porous Media (EPM) Simulation of Groundwater Hydraulics and Contaminant Transport in Karst Aquifers. PloS one 10 (9), e0138954.

Gill, L.W., Naughton, O., Johnston, P.M., 2013. Modeling a network of turloughs in lowland karst. Water Resources Research 49 (6), 3487-3503.

Gobiet, A., Kotlarski, S., Beniston, M., Heinrich, G., Rajczak, J., Stoffel, M., 2014. 21st century climate change in the European Alps – a review. The Science of the total environment 493, 1138-1151.

Goldberg, D.E., 1988. Genetic algorithms in search, optimization, and machine learning. Addison-Wesley, Reading.

Goldscheider, N., 2002. Hydrogeology and Vulnerability of Karst Systems - Examples from the Northern Alps and the Swabian Alb, Ph.D. thesis.

Goldscheider, N., 2005. Fold structure and underground drainage pattern in the alpine karst system Hochifen-Gottesacker. Eclogae Geologicae Helvetiae 98 (1), 1-17.

Goldscheider, N., 2011. Alpine Hydrogeologie. Grundwasser 16 (1), 1.

Goldscheider, N., Drew, D., 2007. Methods in karst hydrogeology. Taylor & Francis, London.

Goldscheider, N., Meiman, J., Pronk, M., Smart, C., 2008. Tracer tests in karst hydrogeology and speleology. International Journal of Speleology 37 (1), 27-40.

Goldscheider, N., Madl-Szonyi, J., Eross, A., Schill, E., 2010. Review: Thermal water resources in carbonate rock aquifers. Hydrogeology Journal 18, 1303-1318.

Göppert, N., Goldscheider, N., 2008. Solute and Colloid Transport in Karst Conduits under Low- and High-Flow Conditions. Ground Water 46 (1), 61-68.

Göppert, N., Goldscheider, N., Scholz, H., 2011. Karst geomorphology of carbonatic conglomerates in the Folded Molasse zone of the Northern Alps (Austria/Germany). Geomorphology 130, 289-298.

Gremaud, V., Goldscheider, N., Savoy, L., Favre, G., Masson, H., 2009. Geological structure, recharge processes and underground drainage of a glacierised karst aquifer system, Tsanfleuron-Sanetsch, Swiss Alps. Hydrogeology Journal 17 (8), 1833-1848.

Gremaud, V., Goldscheider, N., 2010. Climate Change Effects on Aquifer Recharge in a Glacierised Karst Aquifer System, Tsanfleuron-Sanetsch, Swiss Alps, in: Andreo, B., Carrasco, F., Durán, J.J., LaMoreaux, J.W. (Eds.), Advances in Research in Karst Media. Springer Berlin Heidelberg, Berlin, Heidelberg, 31-36.

Guo, F., Jiang, G., Yuan, D., Polk, J.S., 2013. Evolution of major environmental geological problems in karst areas of Southwestern China. Environmental Earth Sciences 69, 2427-2435.

Hall, J.W., Tarantola, S., Bates, P.D., Horritt, M.S., 2005. Distributed Sensitivity Analysis of Flood Inundation Model Calibration. Journal of Hydraulic Engineering 131 (2), 117-126.

Hartmann, A., Kralik, M., Humer, F., Lange, J., Weiler, M., 2012. Identification of a karst system's intrinsic hydrodynamic parameters: upscaling from single springs to the whole aquifer. Environmental Earth Sciences 65 (8), 2377-2389.

Hartmann, A., Wagener, T., Rimmer, A., Lange, J., Brielmann, H., Weiler, M., 2013. Testing the realism of model structures to identify karst system processes using water quality and quantity signatures. Water Resources Research 49 (6), 3345-3358.

Hartmann, A., Goldscheider, N., Wagener, T., Lange, J., Weiler, M., 2014. Karst water resources in a changing world: Review of hydrological modeling approaches. Reviews of Geophysics 52, 218-242.

Hartmann, A., Gleeson, T., Rosolem, R., Pianosi, F., Wada, Y., Wagener, T., 2015. A large-scale simulation model to assess karstic groundwater recharge over Europe and the Mediterranean. Geoscientific Model Development 8, 1729-1746.

Hartmann, J., Moosdorf, N., 2012. The new global lithological map database GLiM: A representation of rock properties at the Earth surface. Geochemistry Geophysics Geosystems 13.

Herman, J.D., Kollat, J.B., Reed, P.M., Wagener, T., 2013. From maps to movies: high-resolution time-varying sensitivity analysis for spatially distributed watershed models. Hydrology and Earth System Sciences 17 (12), 5109-5125.

Hill, M.C., Tiedeman, C.R., 2007. Effective groundwater model calibration: With analysis of data, sensitivities, predictions, and uncertainty. Wiley-Interscience, Hoboken.

Hock, R., 1999. A distributed temperature-index ice- and snowmelt model including potential direct solar radiation. Journal of Glaciology 45 (149), 101-111.

Höhlenverein Sonthofen (Eds.), 2006. Das Hölloch im Mahdtal – 100 Jahre Höhlenforschung im Kleinwalsertal, Sonthofen.

Hollingsworth, E., 2009. Karst regions of the world (KROW)—populating global karst datasets and generating maps to advance the understanding of karst occurrence and protection of karst species and habitats worldwide. University of Arkansas.

Hornberger, G., Spear, R., 1981. An approach to the preliminary analysis of environmental systems. Journal of Environmental Management (12), 7-18.

Horton, P., Schaefli, B., Mezghani, A., Hingray, B., Musy, A., 2006. Assessment of climate-change impacts on alpine discharge regimes with climate model uncertainty. Hydrological Processes 20 (10), 2091-2109.

Huber, C., Dickinson, R., 1992. Storm water management model, version 4. user's manual.

Janža, M., 2010. Hydrological modeling in the karst area, Rižana spring catchment, Slovenia. Environmental Earth Sciences 61 (5), 909-920.

Jasper, K., Calanca, P., Gyalistras, D., Fuhrer, J., 2004. Differential impacts of climate change on the hydrology of two alpine river basins. Climate Research 26, 113-129.

Jeannin, P.Y., 2001. Modeling flow in phreatic and epiphreatic Karst conduits in the Hölloch Cave (Muotatal, Switzerland). Water Resources Research 37 (2), 191-200.

Jeannin, P.-Y., 2016. Main karst and caves of Switzerland, Boletín Geológico y Minero, 127(1), 45-46.

Jukić, D., Denić-Jukić, V., 2009. Groundwater balance estimation in karst by using a conceptual rainfall–runoff model. Journal of Hydrology 373 (3-4), 302-315.

Junghans, N., Cullmann, J., Huss, M., 2011. Evaluating the effect of snow and ice melt in an Alpine headwater catchment and further downstream in the River Rhine. Hydrological Sciences Journal 56 (6), 981-993.

Kampf, S.K., Burges, S.J., 2007. A framework for classifying and comparing distributed hillslope and catchment hydrologic models. Water Resources Research 43 (5).

Kauahikaua, J., Cashman, K.V., Mattox, T.N., Heliker, C.C., Hon, K.A., Mangan, M.T., Thornber, C.R., 1998. Observations on basaltic lava streams in tubes from Kilauea Volcano, island of Hawai'i. Journal of Geophysical Research-Solid Earth 103, 27303-27323.

Kiraly, L., 1998. Modeling karst aquifers by the combined discrete channel and continuum approach. Bulletin d'Hydrogeologie (Neuchâtel) (16), 77-98.

Kiraly, L., 2002. Karstification and groundwater flow, in: Proceedings of the Conference on Evolution of Karst: From Prekarst to Cessation, 155-190.

Kollat, J.B., Reed, P.M., Wagener, T., 2012. When are multiobjective calibration trade-offs in hydrologic models meaningful? Water Resources Research 48 (3).

Kordilla, J., Sauter, M., Reimann, T., Geyer, T., 2012. Simulation of saturated and unsaturated flow in karst systems at catchment scale using a double continuum approach. Hydrology and Earth System Sciences 16 (10), 3909-3923.

Kovacs, A., Sauter, M., 2007. Modelling karst hydrodynamics, in: Goldscheider, N. & Drew, D. (Eds.), Methods in Karst Hydrogeology, 201-220.

Kozary, M.T., Dunlap, J.C., Humphrey, W.E., 1968. Incidence of saline deposits in geologic time. Geological Society of America, Special Paper 88, 43-57.

Kraller, G., Warscher, M., Kunstmann, H., Vogl, S., Marke, T., Strasser, U., 2012. Water balance estimation in high Alpine terrain by combining distributed modeling and a neural network approach (Berchtesgaden Alps, Germany). Hydrology and Earth System Sciences 16 (7), 1969-1990.

Kresic, N., Stevanovic, Z., 2010. Groundwater Hydrology of Springs. Engineering, Theory, Management, and Sustainability. Elsevier, Butterworth-Heinemann, Oxford.

Krysanova, V., Hattermann, F., Wechsung, F., 2007. Implications of complexity and uncertainty for integrated modelling and impact assessment in river basins. Environmental Modelling & Software 22 (5), 701-709.

Kubota, T., Shige, S., Hashizurne, H., Aonashi, K., Takahashi, N., Seto, S., Hirose, M., Takayabu, Y.N., Ushio, T., Nakagawa, K., Wanami, K., Kachi, M., Okamoto, K.i., 2007. Global precipitation map using satellite-borne microwave radiometers by the GSMaP project: Production and validation. Ieee Transactions on Geoscience and Remote Sensing 45, 2259-2275.

Kumar, L., Skidmore, A.K., Knowles, E., 1997. Modelling topographic variation in solar radiation in a GIS environment. International Journal of Geographical Information Science 11 (5), 475-497.

Kunstmann, H., Krause, J., Mayr, S., 2006. Inverse distributed hydrological modelling of Alpine catchments. Hydrology and Earth System Sciences 10 (3), 395-412.

Kunstmann, H., Schneider, K., Forkel, R., Knoche, R., 2004. Impact analysis of climate change for an Alpine catchment using high resolution dynamic downscaling of ECHAM4 time slices. Hydrology and Earth System Sciences 8 (6), 1031-1045.

Kunstmann, H., Stadler, C., 2005. High resolution distributed atmospheric-hydrological modelling for Alpine catchments. Journal of Hydrology 314 (1-4), 105-124.

Lakshmi Prasad, K., Rastogi, A.K., 2001. Estimating net aquifer recharge and zonal hydraulic conductivity values for Mahi Right Bank Canal project area, India by genetic algorithm. Journal of Hydrology 243, 149-161.

Lang, U., 1995. Simulation regionaler Strömungs- und Transportvorgänge in Karstaquiferen mit Hilfe des Doppelkontinuumansatzes: Methodenentwicklung und Parameteridentifikation. Ph.D. thesis.

Lauber, U., Goldscheider, N., 2014. Use of artificial and natural tracers to assess groundwater transit-time distribution and flow systems in a high-alpine karst system (Wetterstein Mountains, Germany). Hydrogeology Journal 22 (8), 1807-1824.

Laumanns, M. (2002) Atlas of the great caves and the karst of Africa. 1st ed. Berlin: Speläoclub Berlin (Berliner Höhlenkundliche Berichte, Bd. 7-9).

Lehner, B., Liermann, C.R., Revenga, C., Voeroesmarty, C., Fekete, B., Crouzet, P., Doell, P., Endejan, M., Frenken, K., Magome, J., Nilsson, C., Robertson, J.C., Roedel, R., Sindorf, N., Wisser, D., 2011. High-resolution mapping of the world's reservoirs and dams for sustainable river-flow management. Frontiers in Ecology and the Environment 9, 494-502.

Lehning, M., Völksch, I., Gustafsson, D., Nguyen, T.A., Stähli, M., Zappa, M., 2006. ALPINE3D: a detailed model of mountain surface processes and its application to snow hydrology. Hydrological Processes 20 (10), 2111-2128.

Lenderink, G., Buishand, A., van Deursen, W., 2007. Estimates of future discharges of the river Rhine using two scenario methodologies: direct versus delta approach. Hydrology and Earth System Sciences 11 (3), 1145-1159.

Leydecker, A., Melack, J., 2000. Estimating evaporation in seasonally snow-covered catchments in the Sierra Nevada, California. Journal of Hydrology 236 (1-2), 121-138.

Liedl, R., Sauter, M., Hückinghaus, D., Clemens, T., Teutsch, G., 2003. Simulation of the development of karst aquifers using a coupled continuum pipe flow model. Water Resources Research 39 (3), 1057.

Liong, S., Chan, W., ShreeRam, J., 1995. Peak-Flow Forecasting with Genetic Algorithm and SWMM. Journal of Hydraulic Engineering 121 (8), 613-617.

Long, J.C.S., Remer, J.S., Wilson, C.R., Witherspoon, P.A., 1982. Porous media equivalents for networks of discontinuous fractures. Water Resources Research 18 (3), 645-658.

Lu, Y., 2006. Karst water resources and geo-ecology in typical regions of China. Environmental Geology 51 (5), 695-699.

Malard, A., Sinreich, M., Jeannin, P.-Y., 2016. A novel approach for estimating karst groundwater recharge in mountainous regions and its application in Switzerland. Hydrological Processes 30 (13), 2153-2166.

Massmann, C., Wagener, T., Holzmann, H., 2014. A new approach to visualizing time-varying sensitivity indices for environmental model diagnostics across evaluation time-scales. Environmental Modelling & Software 51, 190-194.

Maurice, L.D., Atkinson, T.C., Barker, J.A., Bloomfield, J.P., Farrant, A.R., Williams, A.T., 2006. Karstic behaviour of groundwater in the English Chalk. Journal of Hydrology 330, 63-70.

McCormack, T., Gill, L.W., Naughton, O., Johnston, P.M., 2014. Quantification of submarine/intertidal groundwater discharge and nutrient loading from a lowland karst catchment. Journal of Hydrology 519, 2318-2330.

McIntyre, N., Jackson, B., Wade, A., Butterfield, D., Wheater, H., 2005. Sensitivity analysis of a catchment-scale nitrogen model. Journal of Hydrology 315 (1-4), 71-92.

Middelkoop, H., Daamen, K., Gellens, D., Grabs, W., Kwadijk, J. C. J., Lang, H., Parmet, B. W. A. H., Schädler, B., Schulla, J., Wilke, K., 2001. IMPACT OF CLIMATE CHANGE ON HYDROLOGICAL REGIMES AND WATER RESOURCES MANAGEMENT IN THE RHINE BASIN. Climatic Change 49 (1/2), 105-128.

Mokhtari, A., Frey, H.C., 2005. Sensitivity Analysis of a Two-Dimensional Probabilistic Risk Assessment Model Using Analysis of Variance. Risk Analysis 25 (6), 1511-1529.

Moosdorf, N., Hartmann, J., 2015. Lithological map of the World. Commission of the Geological Map of the World (CGMW), Paris.

Moreau, P., Viaud, V., Parnaudeau, V., Salmon-Monviola, J., Durand, P., 2013. An approach for global sensitivity analysis of a complex environmental model to spatial inputs and parameters: A case study of an agro-hydrological model. Environmental Modelling & Software 47, 74-87.

Neter, J., Kutner, M.H., Nachtsheim, C.J., 1996. Applied linear statistical models, 4th ed. Irwin, Chicago.

Nossent, J., Elsen, P., Bauwens, W., 2011. Sobol' sensitivity analysis of a complex environmental model. Environmental Modelling & Software 26 (12), 1515-1525.

Oehlmann, S., Geyer, T., Licha, T., Birk, S., 2013. Influence of aquifer heterogeneity on karst hydraulics and catchment delineation employing distributive modeling approaches. Hydrology and Earth System Sciences 17 (12), 4729-4742.

Orăşeanu, I., Iurkiewicz, A., 2010. Karst Hydrogeology of Romania, Oradea.

Palmer, A.N., 1991. Origin and morphology of limestone caves. Geological Society of America Bulletin 103, 1-21.

Palmer, A.N., Palmer, M.V., 2009. Caves and Karst of the USA. National Speleological Society.

Pappenberger, F., Beven, K.J., Ratto, M., Matgen, P., 2008. Multi-method global sensitivity analysis of flood inundation models. Advances in Water Resources 31 (1), 1-14.

Peña-Haro, S., Pulido-Velazquez, M., Llopis-Albert, C., 2011. Stochastic hydro-economic modeling for optimal management of agricultural groundwater nitrate pollution under hydraulic conductivity uncertainty. Environmental Modelling & Software 26 (8), 999-1008.

Peterson, E.W., Wicks, C.M., 2006. Assessing the importance of conduit geometry and physical parameters in karst systems using the storm water management model (SWMM). Journal of Hydrology 329 (1-2), 294-305.

Piccini, L., Mecchia, M., 2009. Solution weathering rate and origin of karst landforms and caves in the quartzite of Auyan-tepui (Gran Sabana, Venezuela). Geomorphology 106, 15-25.

Prelovšek, M., Turk, J., Gabrovšek, F., 2008. Hydrodynamic aspect of caves. International Journal of Speleology 37 (1), 11-26.

Ravbar, N., Šebela, S., 2015. The effectiveness of protection policies and legislative framework with special regard to karst landscapes: insights from Slovenia. Environmental Science & Policy, 51, 106-116.

Razavi, S., Gupta, H.V., 2015. What do we mean by sensitivity analysis? The need for comprehensive characterization of "global" sensitivity in Earth and Environmental systems models. Water Resources Research 51 (5), 3070-3092.

Reimann, T., 2009. MODFLOW-2005 CFP – Ein Hybridmodell für Karstgrundwasserleiter. Grundwasser 14 (2), 139-145.

Reimann, T., Geyer, T., Shoemaker, W. Barclay, Liedl, R., Sauter, M., 2011. Effects of dynamically variable saturation and matrix-conduit coupling of flow in karst aquifers. Water Resources Research 47 (11), W11503.

Reusser, D.E., Zehe, E., 2011. Inferring model structural deficits by analyzing temporal dynamics of model performance and parameter sensitivity. Water Resources Research 47 (7).

Reusser, D.E., Buytaert, W., Zehe, E., 2011. Temporal dynamics of model parameter sensitivity for computationally expensive models with the Fourier amplitude sensitivity test. Water Resources Research 47 (7).

Richts, A., Struckmeier, W., Zaepke, M., 2011. WHYMAP and the Groundwater Resources Map of the World 1:25,000,000, Sustaining Groundwater Resources, International Year of Planet Earth, 159-173.

Rimmer, A., Salingar, Y., 2006. Modelling precipitation-streamflow processes in karst basin: The case of the Jordan River sources, Israel. Journal of Hydrology 331, 524-542.

Rogger, M., Viglione, A., Derx, J., Blöschl, G., 2013. Quantifying effects of catchments storage thresholds on step changes in the flood frequency curve. Water Resources Research 49 (10), 6946-6958.

Rooij, R. de, Perrochet, P., Graham, W., 2013. From rainfall to spring discharge: Coupling conduit flow, subsurface matrix flow and surface flow in karst systems using a discrete–continuum model. Advances in Water Resources 61, 29-41.

Rössler, O., Diekkrüger, B., Löffler, J., 2012. Potential drought stress in a Swiss mountain catchment-Ensemble forecasting of high mountain soil moisture reveals a drastic decrease, despite major uncertainties. Water Resources Research 48 (4).

Rossman, L., 2006. Storm water management model; quality assurance report. dynamic wave flow routing.

Rossman, L., 2010. Strom water management model. user's manual, version 5.0.

Saltelli, A., 2002. Making best use of model evaluations to compute sensitivity indices. Computer Physics Communications 145 (2), 280-297.

Saltelli, A., Tarantola, S., Campolongo, F., Ratto, M., 2004. Sensitivity analysis in practice: A guide to assessing scientific models. Wiley, Hoboken, NJ.

Saltelli, A., Annoni, P., Azzini, I., Campolongo, F., Ratto, M., Tarantola, S., 2010. Variance based sensitivity analysis of model output. Design and estimator for the total sensitivity index. Computer Physics Communications 181 (2), 259-270.

Saltelli, A., Chan, K., Scott, E.M., 2000. Sensitivity analysis. J. Wiley & sons, New York, Chichester, Weinheim.

Sauter, M., 1992. Quantification and Forecasting of Regional Groundwater Flow and Transport in a Karst Aquifer (Gallusquelle, Malm, SW. Germany). Tübinger Geowissenschaftliche Arbeiten.

Sauter, M., Geyer, T., Kovács, A., Teutsch, G., 2006. Modellierung der Hydraulik von Karstgrundwasserleitern – Eine Übersicht. Grundwasser 11 (3), 143-156.

Scanlon, B.R., Mace, R.E., Barrett, M.E., Smith, B., 2003. Can we simulate regional groundwater flow in a karst system using equivalent porous media models? Case study, Barton Springs Edwards aquifer, USA. Journal of Hydrology 276 (1-4), 137-158.

Seibert, J., 2000. Multi-criteria calibration of a conceptual runoff model using a genetic algorithm. Hydrology and Earth System Sciences 4 (2), 215-224.

Sieber, A., Uhlenbrook, S., 2005. Sensitivity analyses of a distributed catchment model to verify the model structure. Journal of Hydrology 310 (1-4), 216-235.

Singh, R., Wagener, T., Crane, R., Mann, M.E., Ning, L., 2014. A vulnerability driven approach to identify adverse climate and land use change combinations for critical hydrologic indicator thresholds: Application to a watershed in Pennsylvania, USA. Water Resources Research 50 (4), 3409-3427.

Sinreich, M., Goldscheider, N., Hötzl, H., 2002. Hydrogeologie einer alpinen Bergsturzmasse (Schwarzwassertal, Vorarlberg). Beiträge zur Hydrogeologie 53, 5-20.

Sivelli, M., De Waele, J., (Editors), 2013. A journey across speleological Italy. Map in Scale 1:1.500,000, Società Speleologica Italiana, supplement to Speleologia 68.

Skoglund, R.O., Lauritzen, S.-E., 2011. Subglacial maze origin in low-dip marble stripe karst: examples from Norway. Journal of Cave and Karst Studies 73, 31-43.

Sobol', I., 1967. On the distribution of points in a cube and the approximate evaluation of integrals. USSR Computational Mathematics and Mathematical Physics 7 (4), 86-112.

Sobol', I.M., 1976. Uniformly distributed sequences with an additional uniform property. USSR Computational Mathematics and Mathematical Physics 16 (5), 236-242.

Sobol', I.M., 1990. On sensitivity estimation for nonlinear mathematical models. Matematicheskoe Modelirovanie, 112-118.

Song, X., Zhan, C., Xia, J., Kong, F., 2012. An efficient global sensitivity analysis approach for distributed hydrological model. Journal of Geographical Sciences 22 (2), 209-222.

Stevanovic, Z., 2015. Karst Aquifers - Characterization and Engineering, Professional Practice in Earth Sciences. Springer International Publishing.

Stevanovic, Z., Goldscheider, N., Chen, Z., the WOKAM Team (2016) WOKAM – The world karst aquifer mapping project, examples from South East Europe, Near and Middle East and Eastern Africa. In: Karst without Boundaries, edited by Stevanovic, Z., Kresic, N., Kukuric, N., CRC Press 2016, 39-51.

Stevanovic, Z., Jemcov, I.,1996. Digital Hydrogeological Map of Yugoslavia (in Serbian). Proceedings of the XI Yugoslavian Symposium on hydrogeology and engineering geology, Budva, Vol. 1, 163-170.

Tang, Y., Reed, P., van Werkhoven, K., Wagener, T., 2007a. Advancing the identification and evaluation of distributed rainfall-runoff models using global sensitivity analysis. Water Resources Research 43 (6).

Tang, Y., Reed, P., Wagener, T., van Werkhoven, K., 2007b. Comparing sensitivity analysis methods to advance lumped watershed model identification and evaluation. Hydrology and Earth System Sciences 11 (2), 793-817.

Teutsch, G., 1988. Grundwassermodelle im Karst: Praktische Ansätze am Beispiel zweier Einzugsgebiete im Tiefen und Seichten Malmkarst der Schwäbischen Alb. Ph.D. thesis.

Teutsch, G., Sauter, M., 1991. Groundwater modeling in karst terrains: Scale effects, data acquisition and field validation, in: 3rd Conference on hydrogeology, ecology, monitoring and management of ground water in karst terranes, Nashville, USA, 17-35.

UNESCO-IHP, 2013. Protection and Sustainable Use of the Dinaric Karst Transboundary Aquifer System, Transboundary Diagnostic Analysis. UNESCO-IHP, Paris.

Uusitalo, L., Lehikoinen, A., Helle, I., Myrberg, K., 2015. An overview of methods to evaluate uncertainty of deterministic models in decision support. Environmental Modelling & Software 63, 24-31.

van Griensven, A., Meixner, T., Grunwald, S., Bishop, T., Diluzio, M., Srinivasan, R., 2006. A global sensitivity analysis tool for the parameters of multi-variable catchment models. Journal of Hydrology 324 (1-4), 10-23.

van Werkhoven, K., Wagener, T., Reed, P., Tang, Y., 2008. Rainfall characteristics define the value of streamflow observations for distributed watershed model identification. Geophysical Research Letters 35 (11).

Viviroli, D., Dürr, H.H., Messerli, B., Meybeck, M., Weingartner, R., 2007. Mountains of the world, water towers for humanity: Typology, mapping, and global significance. Water Resources Research 43 (7).

Vrugt, J.A., ter Braak, C., Diks, C., Robinson, B.A., Hyman, J.M., Higdon, D., 2009. Accelerating Markov Chain Monte Carlo Simulation by Differential Evolution with Self-Adaptive Randomized Subspace Sampling. International Journal of Nonlinear Sciences and Numerical Simulation 10 (3).

Vrugt, J.A., 2016. Markov chain Monte Carlo simulation using the DREAM software package: Theory, concepts, and MATLAB implementation. Environmental Modelling & Software 75, 273-316.

Waele, J. de, Piccini, L., Columbu, A., Madonia, G., Vattano, M., Calligaris, C., D'Angeli, I., Parise, M., Chiesi, M., Sivelli, M., Vigna, B., Zini, L., Chiarini, V., Sauro, F., Drysdale, R., Forti, P., 2017. Evaporite karst in Italy: a review. International Journal of Speleology 46 (2), 137-168.

Wagner, G., 1950. Rund um Hochifen und Gottesackergebiet. eine Einführung in die Erd- und Landschaftsgeschichte des Gebietes zwischen Iller und Bregenzer Ach.

Wagener, T., Reed, P., van Werkhoven, K., Tang, Y., Zhang, Z., 2009a. Advances in the identification and evaluation of complex environmental systems models. Journal of Hydroinformatics 11 (3-4), 266.

Wagener, T., van Werkhoven, K., Reed, P., Tang, Y., 2009b. Multiobjective sensitivity analysis to understand the information content in streamflow observations for distributed watershed modeling. Water Resources Research 45 (2).

Wendling, U., Müller, J., 1984. Entwicklung eines Verfahrens zur rechnerischen Abschätzung der Verdunstung im Winter. Meteorologische Zeitschrift (34), 82-85.

White, W., 2003. Conceptual models for karstic aquifers. Speleogenesis and evolution of karst aquifers 1, 1-6.

WHYMAP, 2008. Groundwater Resources of the World, 1:25,000,000. World-wide Hydrogeological Mapping and Assessment Programme (WHYMAP) Consortium. BGR, Hannover and UNESCO, Paris.

Williams, P.W., Ford, D.C., 2006. Global distribution of carbonate rocks. Zeitschrift für Geomorphologie Suppl.-Vol. 147, 1-2.

Williams, P., 2008. The role of the epikarst in karst and cave hydrogeology: a review. International Journal of Speleology 37 (1), 1-10.

Worthington, S.R.H., 2009. Diagnostic hydrogeologic characteristics of a karst aquifer (Kentucky, USA). Hydrogeology Journal 17 (7), 1665-1678.

Worthington, S.R.H., Smart, C.C., Ruland, W., 2012. Effective porosity of a carbonate aquifer with bacterial contamination: Walkerton, Ontario, Canada. Journal of Hydrology 464-465 (0), 517-527.

Wu, Y., Jiang, Y., Yuan, D., Li, L., 2008. Modeling hydrological responses of karst spring to storm events: example of the Shuifang spring (Jinfo Mt., Chongqing, China). Environmental Geology 55 (7), 1545-1553.

Wu, P., Tang, C., Zhu, L., Liu, C., Cha, X., Tao, X., 2009. Hydrogeochemical characteristics of surface water and groundwater in the karst basin, southwest China. Hydrological Processes 23, 2012-2022.

Xanke, J., Jourde, H., Liesch, T., Goldscheider, N., 2016. Numerical long-term assessment of managed aquifer recharge from a reservoir into a karst aquifer in Jordan. Journal of Hydrology 540, 603-614.

Yang, J., 2011. Convergence and uncertainty analyses in Monte-Carlo based sensitivity analysis. Environmental Modelling & Software 26 (4), 444-457.

Yamazaki, D., Oki, T., Kanae, S., 2009. Deriving a global river network map and its sub-grid topographic characteristics from a fine-resolution flow direction map. Hydrology and Earth System Sciences 13, 2241-2251.

Young, P.C., 1978. A general theory of modelling for badly defined dynamic systems.

Zhan, Y., Zhang, M., 2013. Application of a combined sensitivity analysis approach on a pesticide environmental risk indicator. Environmental Modelling & Software 49, 129-140.

Zhang, C., Chu, J., Fu, G., 2013. Sobol′'s sensitivity analysis for a distributed hydrological model of Yichun River Basin, China. Journal of Hydrology 480, 58-68.

Zierl, B., Bugmann, H., 2005. Global change impacts on hydrological processes in Alpine catchments. Water Resources Research 41 (2).

Online resources:

www-1: World-wide Hydrogeological Mapping and Assessment Programme (WHYMAP), http://www.whymap.org/

www-2: Paul Williams and Yin Ting Fong, World Map of Carbonate Rock Outcrops v3.0, http://web.env.auckland.ac.nz/our_research/karst/

www-3: USGS, Geologic Provinces of the World, http://certmapper.cr.usgs.gov/data/wep/dds60/wep_prv.htm

www-4: Online Geo Information System for Hungary, www.vizugy.hu

www-5: Bob Gulden, Lists of longest and deepest caves in the world, http://www.caverbob.com